Molecular imaging of chemokine-like receptor 1 (CMKLR1) for non-invasive monitoring of monocyte-derived macrophages in experimental lung injury and remodeling

by

Philip Zachary Mannes

Bachelor of Arts, Dartmouth College, 2016

Submitted to the Graduate Faculty of the

School of Medicine in partial fulfillment

of the requirements for the degree of

Doctor of Philosophy

University of Pittsburgh

2023

UNIVERSITY OF PITTSBURGH

SCHOOL OF MEDICINE

This thesis was presented

by

Philip Zachary Mannes

It was defended on

June 2, 2023

and approved by

[1]Committee Chair: Flordeliza Villanueva, MD, Professor, Department of Medicine

[2]Janet Lee, MD, Professor, Department of Medicine

[1]Corrine Kliment, MD, PhD, Assistant Professor, Department of Medicine

[1]Jessie Nedrow, PhD, Assistant Professor, Department of Radiology

[1]Ashok Panigrahy, MD, Professor, Department of Radiology

[1]Dissertation Mentor: Sina Tavakoli, MD, PhD, Assistant Professor, Department of Radiology

Affiliations:

[1]University of Pittsburgh, Pittsburgh, PA

[2]Washington University, St. Louis, MO

Molecular imaging of chemokine-like receptor 1 (CMKLR1) for non-invasive monitoring of monocyte-derived macrophages in experimental lung injury and remodeling

Philip Zachary Mannes, PhD

University of Pittsburgh, 2023

There is a lack of techniques for noninvasive imaging of pulmonary inflammation associated with acute lung injury and pulmonary fibrosis. Here we determined the potential of positron emission tomography of chemokine-like receptor 1 (CMKLR1) to monitor pulmonary inflammation in murine models of lipopolysaccharide- and bleomycin-induced lung injury. Lung uptake of our recently described CMKLR1-targeting radiotracer, [^{64}Cu]NODAGA-CG34, was increased in both models during the inflammatory phase of lung injury and corresponded to lung regions with high CMKLR1 expression. Monocyte-derived macrophages, and to a lesser extent interstitial macrophages and natural killer cells, were the predominant CMKLR1 expressing leukocytes in the lungs, and the pattern of CMKLR1 expression closely resembled that of the radiotracer uptake. Additionally, we establish the clinical relevance of CMKLR1 as a biomarker of ongoing pulmonary inflammation by demonstrating expression of CMKLR1 among patients with acute respiratory distress syndrome (e.g., COVID-19) and pulmonary fibrosis resulting from multiple etiologies. Furthermore, we show that pulmonary expression of CMKLR1 may provide prognostic information in patients with pulmonary fibrosis. CMKLR1-PET is a promising approach to monitor the dynamics of lung inflammation and may represent a new approach for endotyping patients with inflammatory lung diseases.

Table of Contents

List of Tables

List of Figures

Preface

I entered graduate school as an aspiring organic chemist and left with a PhD in pathology, despite focusing primarily on molecular imaging. Put another way, graduate school had many twists and turns that I could not have anticipated nor navigated by myself. Thus, I am indebted to my mentors, friends, and family for their support and guidance throughout the past four years.

First and foremost, I owe many thanks to my PhD mentor, Sina Tavakoli, for many things. I am grateful that he was willing to take me on as a PhD student, especially given I had no background in molecular imaging, immunology, or really anything else relevant to his work. From the start, he was very invested in my development as a physician-scientist. He has spent countless hours in the lab teaching me various laboratory techniques, reinforcing rigorous scientific design, giving quick feedback on manuscripts and grants, and providing me opportunities to begin to function independently. Over the past four years, he has been an excellent mentor and I have learned far more than I ever could have imagined. I am exceedingly thankful for Sina's mentorship and guidance throughout my PhD and along my journey towards becoming a clinician-scientist.

I also must thank Janet Lee for her mentorship and training throughout graduate school. I will always be fortunate that she was willing to co-mentor me, particularly given a large portion of my project was outside of her field. I appreciate how she has always made time for me and ensured that I had whatever resources or mentorship I needed to advance through my PhD training. Dr. Lee went above and beyond as a mentor, and I cannot thank her enough for everything she has done for me.

I owe many thanks to the In Vivo Imaging Facility (IVIF) at UPMC Hillman for their assistance in our PET imaging experiments. I am especially grateful to Joe Latoche and Kate Day for ensuring

the PET experiments went smoothly and for their technical expertise. They have been instrumental in my projects, and I have learned much from each of them. Additionally, I would like to thank Jessie Nedrow for her guidance and mentorship throughout my training. I am very fortunate that she became the IVIF director, and she has always made time for me.

I will always be grateful to Clayton Barnes for many, many things during my PhD. Simply put, he is an excellent researcher and one of the few people over my career that I fully trust in the lab. If something needed to be done, he did it efficiently and correctly. Although I will miss working with Clayton, I wish him the best along his journey towards becoming a physician.

I am also very thankful to Robin Buck and Steve Custer, as well as the Department of Radiology at Pitt. First, Robin made my life easy by efficiently taking care of administrative tasks so that I was able to focus on my PhD. Despite never previously submitting a F30, she walked me through the process and helped me at every step of the way. Thus, my only real job was to hit the submit button. Furthermore, anytime I needed to schedule travel or get reimbursed, she was always available to assist me. Second, Steve was incredibly supportive and ensured I always had the resources to complete my PhD. There are many aspects of my training he likely handled that I will probably never know about, and for that I am thankful. I am very lucky to have been housed in the Department of Radiology and I have only good things to say about my experience.

Furthermore, I would like to thank the leadership and staff of both the MSTP and CMP departments for all their guidance throughout my PhD. In particular, I would like to recognize Wendy Mars and Richard Steinman. I appreciate all that Wendy Mars has done to help me progress through and succeed in the CMP program. She is an excellent director and dedicated to the development of the students. Additionally, Richard Steinman has been an invaluable mentor in many ways and in many situations. A wise MSTP student once told me the truest pieces of advice

ever given to applicants: choose the MSTP program with the best director as eight years is a long time and at some point, you will need the director's help/assistance/guidance/etc.

I am also appreciative of my thesis committee members for their contributions to and support of my PhD training. They provided me with valuable feedback during each meeting to keep my project advancing in a productive manner. I am fortunate that each member of the committee was fully committed to ensuring that I received the best training and mentorship.

Additionally, I would like to thank Flordeliza Villanueva, her lab members, and others working in the Ultrasound Center for their assistance and support during my time working in their lab space. I appreciate the willingness of Anurag, Mohammed, Soheb, and Grace to answer my questions and for providing reagents/technical expertise in a pinch.

Further, I am thankful to Grace Conway for being a true friend in the lab. I always enjoyed sharing lab space with another MSTP student and appreciated the opportunities to discuss non-lab stuff, MSTP stuff, or germane science related topics.

I would like to thank Ray Yurko and Kazi Islam in the Pitt Peptide Core for their assistance in synthesizing and characterizing our countless peptides. They have been a pleasure to work with and I appreciate all of their contributions to our projects.

Additionally, I would like to thank my parents (Dad and Mom), siblings (David, Madi, and Ben), and grandmother (Grandma) for their support throughout my PhD. Although I am not convinced my family always understood my PhD project or the process, I am thankful that they would always listen and be there for me. A PhD can be difficult, but family makes it easier.

I owe a huge debt of gratitude to my wife, Tiffany Wang, for her support during my PhD. While her role is not directly reflected in my papers or thesis, her contributions are everywhere. I am very appreciative that she has always been there for me whether it is assisting me to refine

research questions, troubleshooting failed experiments, or listening as I organized every idea in my head. Further, I am thankful that she helped me develop a degree of work-life balance and planned many non-science adventures for us throughout Pittsburgh. It would have been very difficult, and significantly less fun, to complete my PhD without my best friend.

Finally, there are many other, unlisted individuals who have helped me throughout my PhD in various ways. I am appreciative for all your contributions during my PhD (no matter how small).

And with that, I hope you enjoy reading about my past three years of work.

1.0 Introduction

The following subchapters will briefly introduce key topics relevant to the projects in chapters 2, 3, and 4. These later chapters will explore and expand upon the relevant aspects of this introduction as necessary to provide the appropriate context and rationale for individual studies. Afterward, there will be a discussion section primarily highlighting the translational relevance of the projects described herein and potential future experiments (chapter 5).

1.1 Lung function

The lungs are the fundamental organ of the respiratory system and function to facilitate gas exchange between the environment and bloodstream. Specifically, the major gases exchanged are oxygen and carbon dioxide. In the lungs, oxygen is absorbed into the arterial circulation until being released into peripheral tissues via the capillaries. Oxygen is required for multiple biologic functions, most importantly being aerobic respiration from which much of life, including humans, derives most of its cellular energy. Carbon dioxide, by contrast, is a major byproduct of cellular metabolism and is removed from cells via the bloodstream and ultimately via exhalation in the lungs (e.g., the reverse of oxygen delivery).

Gas exchange occurs in the terminal lung regions, e.g., alveoli, which are highly specialized pulmonary units optimized for efficient diffusion of gases into or out of the bloodstream (Figure 1). Alveoli are air sacs lined with a very thin layer of epithelial pneumocytes in direct contact with

air on one side and capillary endothelial cells carrying blood on the other side. As oxygen and carbon are both relatively non-polar molecules, they diffuse freely across the thin alveolar-capillary barrier.

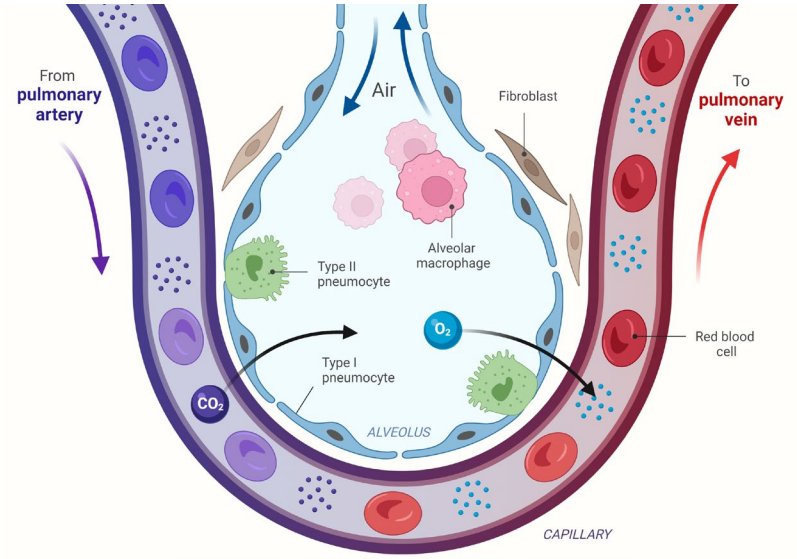

Figure 1. Gas exchange in the healthy lungs.

Deoxygenated blood enters the lungs via the pulmonary artery and travels through the pulmonary arterial system until reaching the capillary bed. Gas exchange readily occurs across the thin alveolar-capillary barrier by diffusion of carbon dioxide from the blood into the alveolar space and oxygen from the alveoli into the blood. Under normal physiologic conditions, the alveoli is filled with air without an air-fluid level. The oxygenated blood then leaves the capillaries and enter the pulmonary veins to eventually return to systemic ciruclation. The figure was provided by BioRender (publication license # DH25CI9RE1).

1.2 Acute lung injury

While the alveoli are ordinarily highly efficient at gas exchange, various pulmonary insults, whether direct (e.g., pneumonia, inhalation injury, lung trauma) or indirect (e.g., sepsis, pancreatitis, non-pulmonary trauma), may lead to disruption of the alveolar-capillary barrier and

the development of acute lung injury (ALI) or acute respiratory distress syndrome (ARDS). Clinically, the diagnosis of ARDS is based on several major criteria including acute onset, bilateral lung infiltrates from non-cardiac origin, and PaO_2/FiO_2 ratio of less than 300 mmHg (1). Unfortunately, there is often a poor prognosis for patients who develop ARDS, and the primary management of ARDS remains supportive as there are currently no definitive treatments.

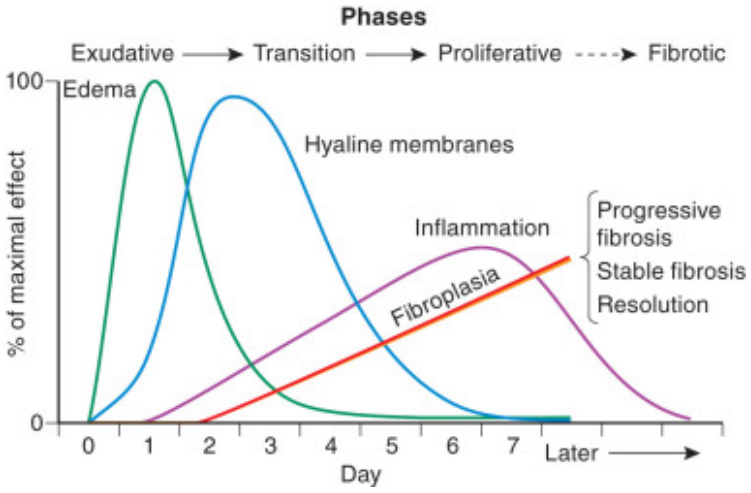

Figure 2. Acute respiratory distress syndrome (ARDS) timeline.

The phases of ARDS are reproducible and reflect the global mechanisms of wound repair (exudation, proliferation, variable fibrogenesis). The indefinite relationship between proliferation and fibrogenesis is depicted as a *hashed line* in the sequence at the top of the figure. In experimental ARDS, the exact time of injury is known, and the entire lung proceeds through the phases at the same time. In a patient who develops diffuse alveolar damage from any cause, the acute lung injury may begin in different areas at different times, so a biopsy specimen may demonstrate injury at various phases in this sequence. The figure and associated legend were reproduced with a license from the publisher (Elsevier) #5534411239332 (2).

ARDS has two key phases: the exudative and proliferative stages (Figure 2) (3). During the early portion of the exudative stage, the lungs undergo diffuse alveolar damage with the key histopathological changes in the lungs being alveolar edema and hyaline membrane formation. The damage to the alveolar pneumocytes and vascular endothelium results in leakage of

proteinaceous fluid and inflammatory cells into the alveolar space. The combination of disruption of the alveolar-capillary barrier along with the alveolar edema results in an air-fluid interface that cannot effectively exchange gases. During the later stages of the exudative phase, patients enter the fibroproliferative/transition phase characterized by resolution of pulmonary edema and early collagen deposition.

In patients surviving the exudative stages, some patients progress into the proliferative phase which is characterized by continued interstitial inflammation and interstitial fibrosis. Chronic activation of inflammatory and fibrogenic processes result in obliteration of the normal lung architecture, including the alveoli, and the development of potentially irreversible pulmonary fibrosis. However, there are no effective methods to predict patients who will progress into the proliferative phase or monitor response to therapy (4).

1.3 Pulmonary fibrosis

In addition to ALI/ARDS, there are a variety of other, non-related causes of pulmonary fibrosis (5) including drug-induced (e.g. amiodarone, bleomycin), environmental (e.g., mold), autoimmune (e.g., scleroderma, sarcoidosis), radiation-induced, and occupational (e.g., silicosis, asbestosis). In some cases, the inciting exposure remains unknown and is classified as idiopathic. Ordinarily following pulmonary injury, the body removes the inciting stimuli and repairs the resulting tissue damage with minimal scar production. In pulmonary fibrosis, various triggers produce an exaggerated wound healing response ultimately leading to fibrotic remodeling and extracellular matrix deposition (6). The underlying pathophysiology of pulmonary fibrosis is believed to involve

aberrant interactions between epithelial and mesenchymal cells leading to activation of fibroblasts and collagen deposition. However, substantial evidence now demonstrates that pulmonary fibrosis often has an inflammatory component that plays a role in the pathogenesis of the inflammation-fibrosis axis (7-9).

Interstitial thickening and destruction of lung architecture leads to poor gas exchange causing many of the hallmark symptoms. Patients with pulmonary fibrosis frequently demonstrate an unpredictable clinical course characterized by periods of relatively stable disease interspersed with life threatening acute exacerbations (10, 11). While there are no treatments, there are two FDA approved medications that slow the decline of pulmonary function (12, 13). Similar to ARDS, there is no widespread consensus on techniques or biomarkers to prognosticate patient outcomes or appropriately select and monitor therapeutic response (10, 14, 15).

1.4 Chemokine-like receptor 1

Chemokine-like receptor 1 (CMKLR1) (16), also identified as ChemR23 (17), is a G protein-coupled receptor (GPCR) that shares structural similarities to other GPCRs for chemokines and chemoattractant molecules (18). Chemerin was the first confirmed endogenous ligand for CMKLR1, although resolvin E1 has subsequently been identified as a second ligand (19, 20). A number of leukocyte populations are known to express CMKLR1 and respond to chemerin signaling, such as macrophages, natural killer cells, and plasmacytoid dendritic cells (21-23). Interestingly, adipocytes have also been shown to express CMKLR1 (24), although the role of CMKLR1 on these cells is less. Chemerin has been further found to bind to two related GPCR, G

protein-coupled receptor 1 (GPR1) and C-C motif chemokine receptor like 2 (CCRL2) (18). However, the function of these two receptors is less well characterized and appears to demonstrate a different expression pattern than that of CMKLR1 (18, 25).

Regulation of the chemerin-CMKLR1 axis is primarily driven by posttranslational processing of chemerin. The best-described function for CMKLR1 is as a chemokine receptor, and the bioactivity of chemerin and related peptides are measured by their potency in chemoattractant and calcium flux assays. Under homeostatic conditions, chemerin is secreted by a diverse range of cells, including the pulmonary epithelium (21), as an inert 143 amino acids pro-peptide (e.g., chemerin$_{20\text{-}163}$) and circulates throughout the body in its inactive form (18, 21). In the inflammatory environment, a number of serine proteases derived from neutrophils, mast cells, and the coagulation cascade proteolytically bioactivate pro-chemerin by selective cleavage of 6 or 7 C-terminus amino acid residues to give chemerin-derived products with high chemotactic potency (i.e., chemerin$_{20\text{-}157}$ and chemerin$_{20\text{-}156}$, respectively) (Figure 3) (26). Despite the necessity of proteases for chemerin bioactivity, a distinct set of enzymes inactivate or degrade chemerin peptides to limit the extent of chemerin activity (27, 28).

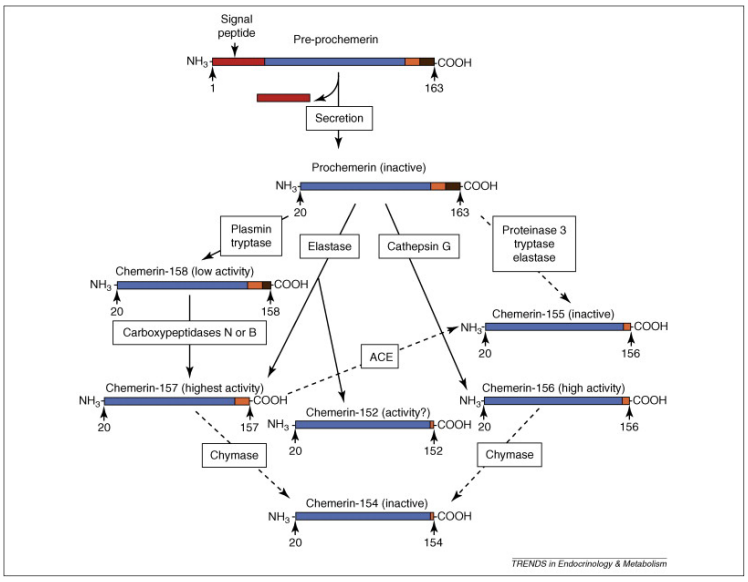

Figure 3. Proteolytic processing of chemerin.

Chemerin is produced as a pre-proprotein, pre-prochemerin (1–163), which requires N-terminal cleavage of a secretion signal peptide before it is secreted as an inactive precursor protein, prochemerin (20–163). Extracellular proteolytic processing of the carboxyterminus of prochemerin exposes the bioactive region. Cathepsin G cleaves seven C-terminal amino acids from prochemerin (chemerin-156), elastase is able to cleave six (chemerin-157), eight (chemerin-155) or eleven (chemerin-152), plasmin cleaves five (chemerin-158), and tryptase cleaves five (chemerin-158) or eight (chemerin-155). Multiple cleavages might be required to fully activate chemerin, with an initial tryptase cleavage resulting in chemerin with low activity (chemerin-158), and a second cleavage by carboxypeptidase N or B producing highly active chemerin (chemerin-157). Chemerin-156 and -157 activities are terminated by chymase cleavage to produce inactive chemerin-154. Chemerin-157 activity might also be terminated by ACE cleavage to produce inactive chemerin-155. The number (e.g. -157) refers to the terminal amino acid position of the processed protein. Solid arrows represent activation pathways; broken arrows represent inactivation pathways. The figure and associated figure legend are reproduced with permission from the publisher (Elsvier) #5534420653203 (29).

Short peptides derived from the C-terminus (e.g., chemerin$_{149\text{-}157}$) of bioactivated chemerin are known to be high-affinity CMKLR1 agonists (30), suggesting that the C-terminus of chemerin may be responsible for CMKLR1 signaling. Additionally, modification of these truncated

chemerin analogs at their N-terminus appears to minimally affect CMKLR1 binding and efficacy (31, 32), which is supported by a recently published cryo-electron microscopy structure of CMKLR1 showing the N-terminus of a short nine amino acid peptide sitting on the outer edge of the ligand-binding pocket (Figure 4) (33). CMKLR1 also appears to tolerate amino acid substitutions (e.g., incorporation of D- or unnatural amino acids) at selected locations without altering the pharmacologic properties of the peptide (31, 32, 34). However, the bioactivated, full length chemerin proteins are more potent and show slightly different signaling properties than that of their truncated or modified counterparts and hints at an unrealized function for the N-terminus of chemerin (27, 35, 36). Interestingly, chemerin and truncated analogs show comparable potency and efficacy in pharmacologic assays when compared across species, which may result from the high degree of sequence homology of CMKLR1 among different species (18). This facilitates evaluation of chemerin-derived analogs in non-human models of disease (21, 32, 34).

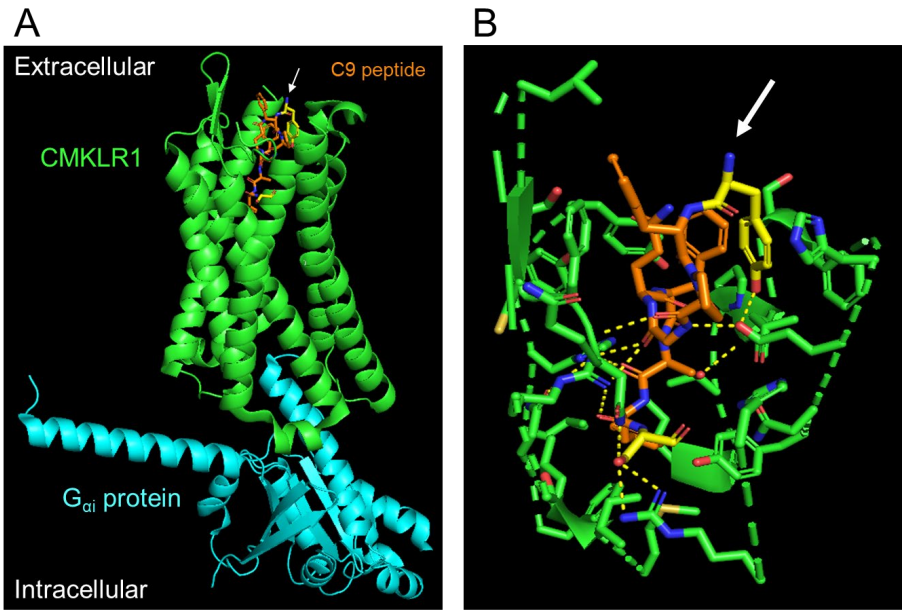

Figure 4. Cryo-EM structure of chemerin$_{149\text{-}157}$ bound to a CMKLR1/$G_{\alpha i}$ protein complex.

(**A**) Chemerin$_{149\text{-}157}$ binds to CMKLR1 such that the C-terminus is buried deep in the binding pocket created by the transmembrane domains with the N-terminus remaining near the surface. The N-terminus amine group of tyrosine

(denoted by the white arrow) does not participate in binding to CMKLR1 points outside of the receptor-ligand binding pocket. (**B**) Magnification of the binding pocket showing the chemerin$_{149\text{-}157}$ peptide and CMKLR1 amino acid residues within 5 Å of the peptide. The yellow dotted lines denote polar contacts between the ligand and receptor. For simplicity of the figure, the G_{β} and G_{γ} subunits, as well as an antibody used for stability of the protein complex, were removed. The figure was created using PyMOL and data available on the Protein Data Bank website (7YKD) (33). Colors: CMKLR1 = green; $G_{\alpha i}$ protein = light blue; Chemerin$_{149\text{-}157}$: orange with exception of C-terminus serine and N-terminus tyrosine which are yellow to assist in their identification.

The chemerin-CMKLR1 axis is biologically relevant in the pathogenesis of pulmonary conditions (21, 37-39), in addition to a wide range of other disorders including the skin (40, 41), heart (42, 43), vasculature (36), and gastrointestinal system (44, 45). For example, in a murine model of lipopolysaccharide-induced acute lung injury, co-administration of chemerin resulted in significantly reduced levels of infiltrating neutrophils (21). By contrast, CMKLR1-knockout mice demonstrated increased numbers of pulmonary neutrophils and macrophages (21). In a separate model of acute viral pneumonia, appropriate chemerin-CMKLR1 signaling was associated with significantly increased survival and improved pulmonary functional measures (37). The role of CMKLR1 in pulmonary fibrosis, however, remains relatively unexplored. While it may be tempting to conclude the chemerin-CMKLR1 axis exerts an anti-inflammatory effect, the exact function of CMKLR1 is likely more complex and, based on available evidence, better understood as a pathway for the recruitment and activation of subsets of leukocytes.

1.5 Positron emission tomography

Despite the relevance of CMKLR1 to the pathophysiology of pulmonary diseases, there remains a lack of available methods for investigating the role and function of CMKLR1 *in vivo*. To enable *in vivo* monitoring of $CMKLR1^+$ cell recruitment and kinetics during distinct phases of preclinical models of lung injury and remodeling, we proposed CMKLR1-targeted positron emission tomography with our recently developed radiotracer, [^{64}Cu]NODAGA-CG34 (22).

Positron emission tomography (PET) is a highly sensitive and non-invasive imaging method for detection of molecular and biological processes in the lung that are difficult to obtain with other imaging modalities, such as computed tomography (CT), magnetic resonance (MR), and ultrasound. Additionally, PET has advantages over non-imaging-based techniques commonly used for assessment of pulmonary pathology, including bronchoalveolar lavage, biopsy, and pulmonary function tests. Firstly, PET is well tolerated by patients with decreased lung function and appropriate for serial measurements, which may be a significant limitation for invasive sampling methods. Secondly, PET is not subject to sampling bias and can provide information regarding disease processes throughout the entirety of the lungs. Thirdly, PET tracer uptake is not dependent on patient effort and less invasive than procedures like bronchoscopy.

There are many reports of PET being used to study pulmonary disease mechanisms in both preclinical and clinical studies. The most commonly used PET tracer remains [^{18}F]FDG largely due to its widespread availability and clinical approval by the U.S. Food & Drug Administration. Although [^{18}F]FDG-PET has shown promise for monitoring inflammatory and fibrogenic processes in the lungs (46-49), the interpretation of [^{18}F]FDG-PET is complicated given its uptake

by all metabolically active cells. To address the lack of specificity of [^{18}F]FDG uptake, PET imaging agents have been developed for selective targeting of individual molecular pathways and processes.

Considerable efforts have been dedicated to investigating individual molecular targets for PET imaging of lung specific applications. For molecular imaging of acute lung injury, many of the reported radiotracers target leukocyte subsets or secreted inflammation associated proteins (22, 46, 50-55). In particular, monocyte (53) and macrophage (22, 54, 55) populations have proven promising as PET imaging targets for non-invasive detection of ongoing inflammation, and the tracer uptake tends to correlate well with established inflammatory markers. While the underlying pathophysiology of acute lung injury and pulmonary fibrosis are different, various PET tracers developed for imaging inflammation have found success for *in vivo* quantification of diseases processes associated with pulmonary fibrosis, notably several myeloid targeted radiotracers (22, 56, 57). Additionally, a separate class of radiotracers specific for fibrogenic mechanisms have found success for imaging pulmonary fibrosis (58-61). Given the complexity of the inflammation-fibrosis axis, a multipronged approach for investigating molecular patterns of lung injury and remodeling is useful to understand distinct aspects of disease pathology and their correlation with clinically meaningful endpoints.

1.6 Organization of thesis chapters.

The first chapter reports preclinical PET imaging of ALI using the most widely available and utilized radiotracer, [^{18}F]FDG. We also show that [^{18}F]FDG uptake by PET may non-invasively

monitor response to anti-inflammatory therapy. Further, we demonstrate that while [^{18}F]FDG appears promising for molecular imaging of ALI, the non-specificity of [^{18}F]FDG uptake by all metabolically active cells is a significant barrier to providing biologically or pathogenically relevant information. We conclude the chapter by highlighting the need to develop pathway specific molecular imaging agents.

In the second chapter, we describe CMKLR1-targeted PET as a new approach for non-invasive and selective monitoring of a specific immune cell population, monocyte-derived macrophages, in the same preclinical model of ALI employed for chapter 1. We report the design and characterization of our CMKLR1-PET tracer, [^{64}Cu]NODAGA-CG34. Additionally, we show that its PET-derived uptake effectively monitors both ongoing pulmonary inflammation and its response to treatment. Furthermore, *in vivo* uptake of [^{64}Cu]NODAGA-CG34 correlates with various biological measures of inflammation. Finally, we demonstrate the potential clinical relevance of CMKLR1 to pulmonary inflammation as CMKLR1 expression in the lungs of patients with COVID-19 closely resembles the expression pattern observed in our preclinical model. Given the known role of monocyte-derived macrophages in driving lung modeling following ALI and the abundance of CMKLR1-cells during the inflammatory phase of ALI, we hypothesized that CMKLR1-PET during the acute inflammatory period of lung injury may predict the development and extent of future lung fibrosis.

In the third chapter, we demonstrate CMKLR1-PET is a promising biomarker for ongoing monocyte-derived macrophage inflammation associated with the early stages of pulmonary fibrosis. Similar to chapter 2, we show that CMKLR1 expression in the lung is primarily expressed by monocyte-derived macrophages during the inflammatory phase in our lung fibrosis model. We further confirm the ability of CMKLR1-PET for non-invasive monitoring of monocyte-derived

macrophages as the of pattern PET-derived [^{64}Cu]NODAGA-CG34 uptake closely resembles that of CMKRL1 expression as measured with flow cytometry. The chapter concludes with clinical histologic and transcriptomics data showing that CMKLR1 expression is increased in the lungs of patients with pulmonary fibrosis and may provide prognostic information regarding patient survival.

The final chapter of the thesis discusses future directions for this CMKLR1 project, with the ultimate goal of eventually translating CMKLR1 radiotracers into the clinic.

2.0 2-deoxy-2-[18F]fluoro-D-glucose positron emission tomography to monitor lung inflammation and therapeutic response to dexamethasone in a murine model of acute lung injury

The work presented in this chapter has been previously published the *Molecular Imaging and Biology* (62), and I am the first author of the manuscript. I have obtained the proper permission from the journal to reproduce the contents of the article in my dissertation (Publisher license #5517271323926).

This study was supported by the following grants: National Institute of Biomedical Imaging and Bioengineering (NIBIB, R21EB027871) and National Heart, Lung, and Blood Institute (NHLBI, K08HL144911) to Sina Tavakoli; NHLBI (F30HL158038) to Philip Mannes; NHLBI (R01HL136143, P01HL114453, R01HL142084, and K24HL143285) to Janet Lee. This work utilized the Hillman Cancer Center In Vivo Imaging Facility, a shared resource at the University of Pittsburgh (supported by P30CA047904).

2.1 Abstract

The purpose of this current study was to image inflammation and monitor therapeutic response to anti-inflammatory intervention using 2-deoxy-2-[^{18}F]fluoro-D-glucose ([^{18}F]FDG) positron emission tomography (PET) in a preclinical model of acute lung injury (ALI). Mice were intratracheally administered lipopolysaccharide (LPS, 2.5 mg/kg) to induce ALI or phosphate-buffered saline as the vehicle control. A subset of mice in the ALI group received two

intraperitoneal doses of dexamethasone 1 and 24 hours after LPS. [^{18}F]FDG PET/CT was performed 2 days after the induction of ALI. [^{18}F]FDG uptake in the lungs was quantified by PET (%ID/mL$_{mean}$ and standardized uptake value (SUV$_{mean}$)) and *ex vivo* γ-counting (%ID/g). The severity of lung inflammation was determined by quantifying the protein level of inflammatory cytokines/chemokines and the activity of neutrophil elastase and glycolytic enzymes. In separate groups of mice, flow cytometry was performed to estimate the contribution of individual immune cell types to the total pulmonary inflammatory cell burden under different treatment conditions. Lung uptake of [^{18}F]FDG was significantly increased during LPS-induced ALI, and a decreased [^{18}F]FDG uptake was observed following dexamethasone treatment to an intermediate level between that of LPS-treated and control mice. Protein expression of inflammatory biomarkers and the activity of neutrophil elastase and glycolytic enzymes were increased in the lungs of LPS-treated mice versus those of control mice, and correlated with [^{18}F]FDG uptake. Furthermore, dexamethasone-induced decreases in cytokine/chemokine protein levels and enzyme activities correlated with [^{18}F]FDG uptake. Neutrophils were the most abundant cells in LPS-induced ALI, and the pattern of total cell burden during ALI with or without dexamethasone therapy mirrored that of [^{18}F]FDG uptake. [^{18}F]FDG PET noninvasively detects lung inflammation in ALI and its response to anti-inflammatory therapy in a preclinical model. However, high [^{18}F]FDG uptake by bone, brown fat, and myocardium remains a technical limitation for quantification of [^{18}F]FDG in the lungs.

2.2 Introduction

Acute lung injury (ALI), clinically known as respiratory distress syndrome (ARDS), represents a life-threatening condition in seriously ill patients characterized by an acute onset of pulmonary infiltrates and impaired oxygenation. ARDS is an inflammatory driven disease resulting from direct (e.g., pneumonia) or indirect pulmonary (e.g., sepsis or trauma) insults leading to disruption of the alveolar-capillary barrier and, ultimately, impaired lung function (3). Clinically, ARDS continues to significantly burden healthcare settings (63), particularly intensive care units, with the incidence of ARDS increasing many folds during the COVID-19 pandemic (64). Despite our improved understanding on the risk factors that are associated with the development of ARDS, the diagnosis of ARDS remains clinical that is based on a constellation of clinical, physiological, and radiographic findings, and we currently lack effective methods to predict patient's outcomes and monitor treatment response.

A promising method for *in vivo* monitoring of molecular patterns of lung inflammation and response to therapy is positron emission tomography (PET). In particular, PET visualizes and quantifies ongoing molecular processes and therefore supplements the anatomical and structural information provided by other imaging modalities, such as computed tomography (CT). Additionally, PET has many advantages to study pulmonary inflammation in comparison to those of currently employed methods. For instance, PET, in contrast to lung biopsy or bronchoalveolar lavage (BAL), can noninvasively visualize lung inflammation without being subject to sampling bias (65). Moreover, PET may detect molecular patterns of inflammation or resolution at an earlier stage than that of other imaging techniques, including CT (46). Also, PET is a quantitative technique that is less affected by patient's effort, which represents a major disadvantage of

physiological tests, such as pulmonary function tests (66). Further, PET can be tailored to monitor individual molecular targets or pathways of interest by the use of specific radiotracers. While much effort is currently being devoted to the development of PET tracers targeting specific aspects of the inflammatory response, the most widely available and studied radiotracer remains 2-deoxy-2-[^{18}F]fluoro-D-glucose ([^{18}F]FDG).

Cellular uptake of [^{18}F]FDG closely reflects glucose uptake as both [^{18}F]FDG and glucose are internalized and processed by related cellular processes (67, 68). [^{18}F]FDG is transported into metabolically active cells via the glucose transporter (GLUT) family of proteins and is subsequently phosphorylated by hexokinases into [^{18}F]FDG-6-phosphate, which is essentially irreversibly trapped intracellularly and cannot be further metabolized via glycolysis (69).

Although [^{18}F]FDG is most extensively utilized for oncological purposes to detect the tumor-associated Warburg effect, the applications of [^{18}F]FDG PET in inflammatory diseases have increased (48, 49, 70). In the inflammatory environment, molecular signals and cascades alter immune cell metabolism in highly orchestrated ways, referred to as immunometabolism. One of the key cellular responses to inflammation is increased glucose metabolism (71). Given that several cell types abundant in the acutely injured lung, such as neutrophils and macrophages, demonstrate increased influx and glucose metabolism in the acutely inflamed tissues, [^{18}F]FDG PET is a clinically available method to sensitively and noninvasively visualize *in vivo* changes in glucose metabolism, ultimately a proxy for total inflammatory cell burden (46, 47, 72).

Clinically, [^{18}F]FDG PET has been demonstrated to noninvasively monitor the underlying inflammatory processes in various pulmonary diseases. Lung uptake of [^{18}F]FDG is increased in chronic obstructive pulmonary disease (COPD), cystic fibrosis, asthma, interstitial lung diseases, and ARDS (47, 48, 73-78). Importantly, [^{18}F]FDG PET provides clinically useful information about disease phenotypes and treatment response. In both COPD (74-76) and idiopathic pulmonary fibrosis (77), for instance, increased [^{18}F]FDG uptake correlates with clinical markers of disease severity and indicates aggressive disease status. A separate study has demonstrated that both total and rate of [^{18}F]FDG uptake are increased in patients with cystic fibrosis compared to healthy controls, and [^{18}F]FDG uptake correlates with neutrophil content of BAL samples (78). Increased lung uptake of [^{18}F]FDG has also been reported in healthy volunteers instilled with intrabronchial endotoxin (48). Interestingly, [^{18}F]FDG PET has been shown to sensitively detect the lung-specific responses to therapies, including statins and recombinant activated protein C, in healthy volunteers receiving intrabronchial endotoxin (47). While almost all immune and non-immune cells contribute to the total uptake of [^{18}F]FDG in the tissues, neutrophils have been shown have the highest ex vivo uptake of [^{3}H]deoxyglucose among the cells recovered by BAL (48, 78).

Despite significant interest in exploring [^{18}F]FDG as a method to noninvasively monitor lung inflammation, with a particular interest in improving our ability to molecularly endotype and stratify patients for improving clinical outcomes, there remain critical gaps in our knowledge that limit the interpretation of [^{18}F]FDG PET and its utility for understanding lung diseases. Two key gaps include whether [^{18}F]FDG uptake correlates with lung tissue expression of inflammatory biomarkers and if [^{18}F]FDG can monitor the response to corticosteroids, as a clinically relevant anti-inflammatory therapy in ARDS. In this study, we demonstrated in a preclinical

lipopolysaccharide (LPS)-induced ALI model that [^{18}F]FDG PET noninvasively detected lung inflammation and response to dexamethasone therapy. Additionally, we showed that [^{18}F]FDG uptake correlated with the expression of selected inflammatory proteins and activity of neutrophil elastase and glycolytic enzymes. We further showed that the total number of cells in the lungs, predominantly driven by changes in neutrophils, closely mirrored that of [^{18}F]FDG uptake under different conditions.

2.3 Methods

2.3.1 Chemicals and reagents

The major chemicals and reagents are listed in Supplemental Table 1, Supplemental Table 2, Supplemental Table 3, Supplemental Table 4, and Supplemental Table 5.

2.3.2 Mouse model of experimental lung injury

Animal experiments were performed using C57BL/6J mice (9- to 12-week-old, Jackson Laboratory, strain #000664). Mice were administered intratracheally with 2.5 μg/g LPS from *Escherichia coli* O111:B4 in 60 μl of phosphate-buffered saline (PBS) to induce lung injury. Control mice were intratracheally injected with 60 μl of PBS. In experiments involving anti-inflammatory treatment, mice received two doses of dexamethasone (10 mg/kg in 500 μL of PBS) via intraperitoneal injections at 1 and 24 hours following LPS instillation, whereas non-dexamethasone treated mice were given intraperitoneal PBS (500 μL) injections. Studies were

performed in accordance with a protocol approved by the University of Pittsburgh Institutional Animal Care and Use Committee.

2.3.3 PET/CT and quantification of [^{18}F]FDG uptake

Mice (n= 4 PBS, 8 LPS, and 8 LPS + Dexamethasone) were fasted the night prior to PET/CT. Two days after intratracheal LPS or PBS instillation, mice were injected intravenously with [^{18}F]FDG (7.52 ± 0.03 MBq) while awake, and the mice remained awake until PET/CT acquisition. Mice were anesthetized with inhalational isoflurane and static PET (~5-min) and CT (180 projections, 140-msec exposure, 180° rotation, 80-kVp, 500-μA, field-of-view: 78.5x100-mm) were performed (Inveon, Siemens) ~60 minutes after radiotracer injection.

Regions of interest were drawn over the left and right lungs, and [^{18}F]FDG uptake in the left and right lungs was averaged and quantified as the mean percentage of injected dose per milliliter of tissue (%ID/mL$_{mean}$) and standard uptake value (SUV$_{mean}$) (IRW software). The peripheral regions of the lungs were excluded from the regions of interest to minimize the effect of scattered radiation from [^{18}F]FDG uptake by myocardium and bones. Following PET/CT, mice were euthanized, and radiotracer uptake was also quantified *ex vivo* by γ-counting (Wizard^2, PerkinElmer) of harvested lungs. Decay-corrected [^{18}F]FDG uptake values are reported.

2.3.4 Lung homogenization

Following γ-counting, the lungs were frozen at -20 °C and stored for >10 half-lives to allow [^{18}F]FDG to fully decay. Then, the left lung was mechanically homogenized in 1 mL of distilled

water. A 10x cytokine lysis buffer (Supplemental Table 2) was added to the lung homogenate (9 parts of lung homogenate: 1 part of 10x cytokine lysis buffer, by volume). After incubating for 30 min at 4 °C, the lung homogenate was centrifuged (10,000 g for 20 min). The resulting supernatant was collected and stored at -80 °C until use.

2.3.5 Protein expression assays

The protein expression of select inflammatory markers in the lung homogenate was quantified using an enzyme-linked immunosorbent assay (ELISA) according to the manufacturer's directions (Supplemental Table 3).

2.3.6 Neutrophil elastase activity assay

The neutrophil elastase activity in lung homogenates was determined as previously described, with minor modifications (79, 80). Briefly, lung homogenate (10 µL) was incubated with 100 µM of a fluorogenic neutrophil elastase substrate (MeOSuc-AAPV-AMC, Millipore Sigma) in 50 µL assay buffer (100 mM Tris-HCl, 500 mM NaCl, pH = 8.0) at 37 °C. Over the course of 3 hours, the fluorescence of each sample was measured every 10 min (Excitation = 380 nm, Emission = 460 nm) with a Synergy H4 Hybrid Microplate Reader (BioTek). The neutrophil elastase activity was calculated as the slope of the linear portion of the fluorescence versus time graph normalized to the average of that of the control mice.

2.3.7 Glycolytic enzyme activity assays

The activity of hexokinase (HK) (81) and lactate dehydrogenase (LDH) (82) was measured using previously reported methods with optimization for use with lung homogenate. Briefly, lung homogenate samples (4.0 µL) were incubated at room temperature with 56.0 µL of the appropriate assay buffers (Supplemental Table 4 and Supplemental Table 5). The absorbance of each sample, resulting from NADH or NADPH reduction of nitro blue tetrazolium chloride, was measured over 10 min at 1 min intervals at 490 nm (83) using a Synergy H4 Hybrid Microplate Reader (BioTek). The rate of enzymatic activities was determined as the slope of the linear portion of the absorbance versus time graph normalized to the average of that of the control mice.

2.3.8 Flow cytometric immunophenotyping of murine lungs

Separate groups of mice treated with LPS (N = 4), LPS + Dexamethasone (N=4), or PBS (N=4) were euthanized, and the pulmonary circulation was perfused with PBS via a right ventricular puncture. Both lungs were then minced with scissors and diluted with dissociation buffer (collagenase A, 1.0 mg/mL in PBS supplemented with 1 mM of Ca^{+2} and Mg^{+2}). The lungs were enzymatically dissociated at 37 °C for 1 hour with shaking. Then, the resulting cell suspensions were passed through 40-µm cell strainers. After red blood cell lysis, Precision Count Beads (50 µL) were added to each sample. After washing with PBS, cells were incubated with 1% bovine serum albumin (BSA) in PBS and treated first with mouse Fc block (2.0 µL per sample), followed by a mixture of antibodies (0.5 µL per antibody per sample) and DAPI (5.0 µL of 1 µg/mL per sample) for 0.5 hour at 4 °C. Finally, cells were washed and fixed with 4% formalin for 0.5 hour at room temperature. Flow cytometry was performed the following day using a LSR II Flow

Cytometry (BD Biosciences) and analyzed using FlowJo software version 10.7.2 (BD Biosciences). A list of the antibodies used in this study is available in Supplemental Table 1.

2.3.9 Statistics

Statistical analysis was performed with Prism 9 (GraphPad). The data are shown as the mean ± SEM. A one-way analysis of variance, followed by Fisher's Exact post hoc test, was used to compare mean values in > 2 groups. Pearson correlations were used to determine the linear relationship between two groups. Statistical significance was considered $P < 0.05$.

2.4 Results

2.4.1 Noninvasive detection of ALI and anti-inflammatory response to dexamethasone by [^{18}F]FDG PET

At 1-h post-injection of [^{18}F]FDG, we observed increased radiotracer uptake in the lungs of LPS-treated mice as compared to those of control mice (Figure 5).The mice receiving LPS followed by dexamethasone demonstrated less lung [^{18}F]FDG uptake than that of LPS-treated mice alone, but greater than that of the control mice. Quantification of PET-derived [^{18}F]FDG uptake confirmed that LPS-treated mice demonstrated significantly increased tracer uptake over PBS-treated mice (by both PET-derived %ID/mL$_{mean}$ and SUV$_{mean}$), which was significantly reduced

by administration of dexamethasone (PET-derived %ID/mL$_{mean}$) with a trend towards a significant decline as measured by SUV$_{mean}$ (Fig. 2A, B).

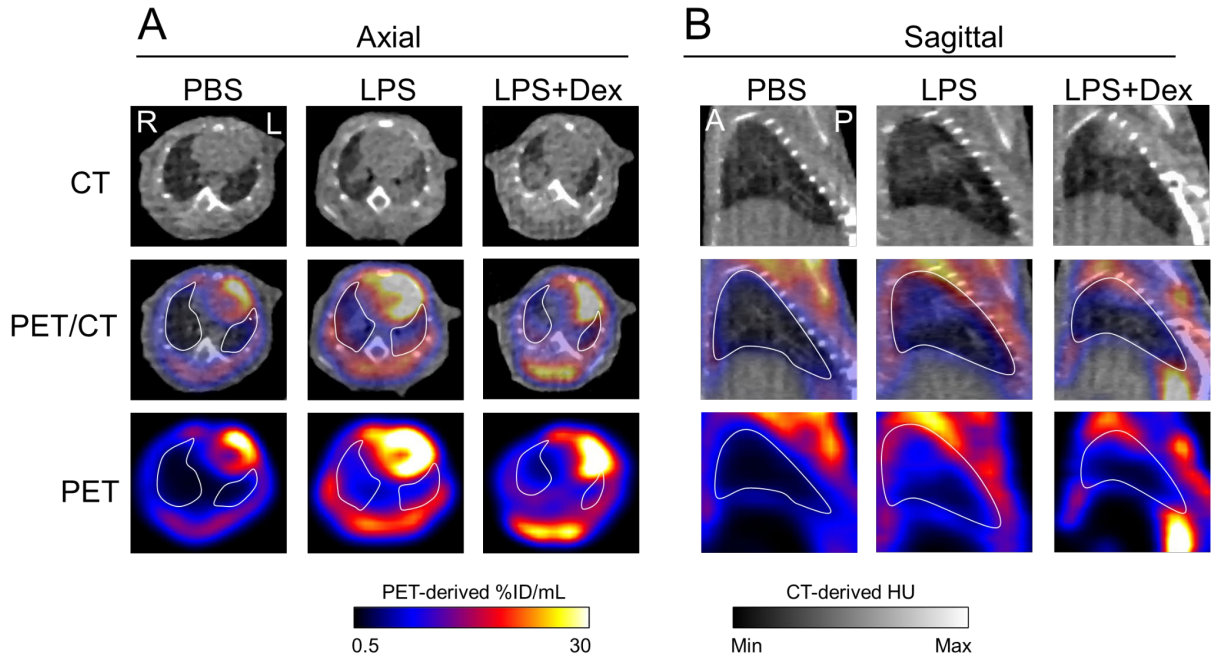

Figure 5. Representative [^{18}F]FDG PET/CT images in LPS-induced ALI and its response to dexamethasone treatment.

(**A**) Axial and (**B**) sagittal PET, CT, and coregistered PET/CT images for mice treated with PBS, LPS, or LPS followed by dexamethasone. Mice treated with LPS show focal regions of pulmonary consolidation and groundglass opacities on the CT, which demonstrate increased [^{18}F]FDG uptake. Dexamethasone treatment decreases lung [^{18}F]FDG uptake, although not to the level of control treated mice. High [^{18}F]FDG uptake is seen in lung-adjacent tissues, including the heart, ribs, and brown fat. The lungs are outlined in white in the PET/CT overlaid images. The white letters indicate image direction: A = anterior, L = left, P = posterior, R = right. Abbreviations: PBS = phosphate buffered saline, LPS = lipopolysaccharide, Dex = dexamethasone.

2.4.2 *Ex vivo* quantification of [^{18}F]FDG uptake by γ-counting correlates moderately with PET-derived %ID/mL$_{mean}$, but less strongly with SUV$_{mean}$

PET-derived quantification of the uptake of radiotracers is subject to inaccuracies resulting from lung-specific (e.g. respiratory motion and lung tissue density) (84, 85) and PET-specific (e.g. scatter, partial volume effect, and positron range) (86, 87) factors. Therefore, we determined the correlations between PET-derived [^{18}F]FDG uptake (%ID/mL$_{mean}$ or SUV$_{mean}$) in the lung and the uptake quantified by *ex vivo* γ-counting (%ID/g), the gold standard for quantification of radiotracer uptake by organs in preclinical studies, to address the accuracy of *in vivo* quantification of [^{18}F]FDG. Similar to the [^{18}F]FDG uptake determined by PET imaging, mice treated with LPS demonstrated significantly increased [^{18}F]FDG uptake in the lungs, compared to that of control mice by *ex vivo* γ-counting (6.95%±0.48 vs. 2.43%±0.37, respectively; $P < 0.0001$) (Figure 6). Consistent with PET-derived quantification, mice receiving LPS followed by dexamethasone had an intermediate level of [^{18}F]FDG uptake that was less than that of the LPS only treated mice (4.79%±0.19 vs. 6.95%±0.48, respectively; $P = 0.0004$) yet greater than that of the control mice (4.79%±0.19 vs. 2.43%±0.37, respectively; $P = 0.0011$). Importantly, there was a moderate correlation between *in vivo* PET-derived %ID/mL$_{mean}$ and *ex vivo* γ-counting-derived (%ID/g) [^{18}F]FDG lung uptake ($R^2 = 0.53$; $P = 0.0003$) (Figure 6). However, the correlation between *in vivo* PET-derived SUV$_{mean}$ and *ex vivo* γ-counting (%ID/g) [^{18}F]FDG was less strong ($R^2 = 0.24$; $P = 0.027$).

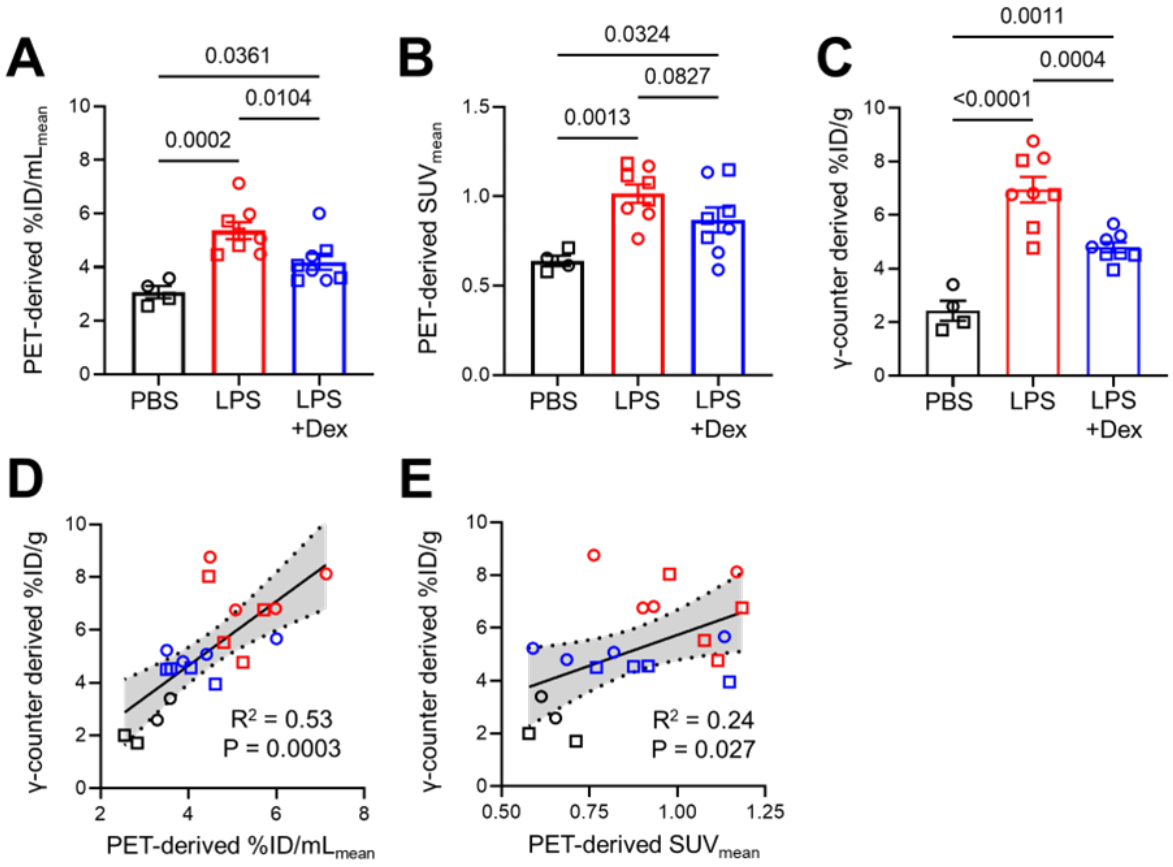

Figure 6. Quantification of [^{18}F]FDG uptake in a preclinical LPS-induced ALI model confirms dexamethasone treatment response may be detected noninvasively by [^{18}F]FDG PET.

The *in vivo* uptake of [^{18}F]FDG in the lungs was quantified by PET-derived (**A**) %ID/mL$_{mean}$ and (**B**) SUV$_{mean}$. (**C**) *Ex vivo* γ-counting was performed on the lungs following completion of PET/CT. (D, E) Correlations between *in vivo* and *ex vivo* [^{18}F]FDG uptake were calculated. N = 4 PBS, 8 LPS, and 8 LPS+Dex treated mice. Equal numbers of male (squares) and female (circles) mice were used per group. Colors: PBS = black, LPS = red, LPS+Dex = blue. Abbreviations: PBS = phosphate buffered saline, LPS = lipopolysaccharide, Dex = dexamethasone.

2.4.3 [^{18}F]FDG uptake correlates with inflammatory biomarkers and the activity of glycolytic enzymes

One of the hallmarks of experimental ALI is the inflammatory response that is characterized by an increase in cytokines and chemokines (88). We tested whether increased [^{18}F]FDG lung uptake in ALI correlates with the abundance of select inflammatory proteins. We found that LPS treatment significantly increased the pulmonary expression of pro-inflammatory cytokines and chemokines (3, 89-92), including interleukin 1-beta (IL-1β), interferon gamma (IFN-γ), interleukin 6 (IL-6), and CXC motif chemokine ligand 1 (CXCL1), versus that of control treated mice (Figure 7). Additionally, dexamethasone reduced the expression of these cytokines and chemokines to an intermediate level between that of the LPS-treated and control mice. We further established that lung uptake of [^{18}F]FDG, as measured with *in vivo* %ID/mL$_{mean}$ or SUV$_{mean}$ or *ex vivo* %ID/g, generally correlated with the expression of established inflammatory markers (Figure 7). In particular, the *ex vivo* [^{18}F]FDG uptake most strongly correlated with inflammatory markers IL-1β and CXCL1.

Recruitment and activation of neutrophils are key features of the initial inflammatory phase of ALI (88), which are mediated by several chemokines, including CXCL1. We therefore tested if [^{18}F]FDG uptake correlated with neutrophil elastase activity in lung homogenate, as a measure for the total burden of neutrophil activation in the lungs (80, 93). As expected, LPS induced a significant increase in lung neutrophil elastase activity, versus that of control mice, that was decreased upon dexamethasone treatment (Figure 8). Although *ex vivo* γ-counting-derived [^{18}F]FDG uptake correlated with neutrophil elastase activity (R^2 = 0.43, P = 0.0017), the

correlations were weaker with PET-derived quantification of [^{18}F]FDG uptake (%ID/mL$_{mean}$: R^2 = 0.18, P = 0.064 and SUV$_{mean}$: R^2 = 0.28, P = 0.017) (Fig. 4B).

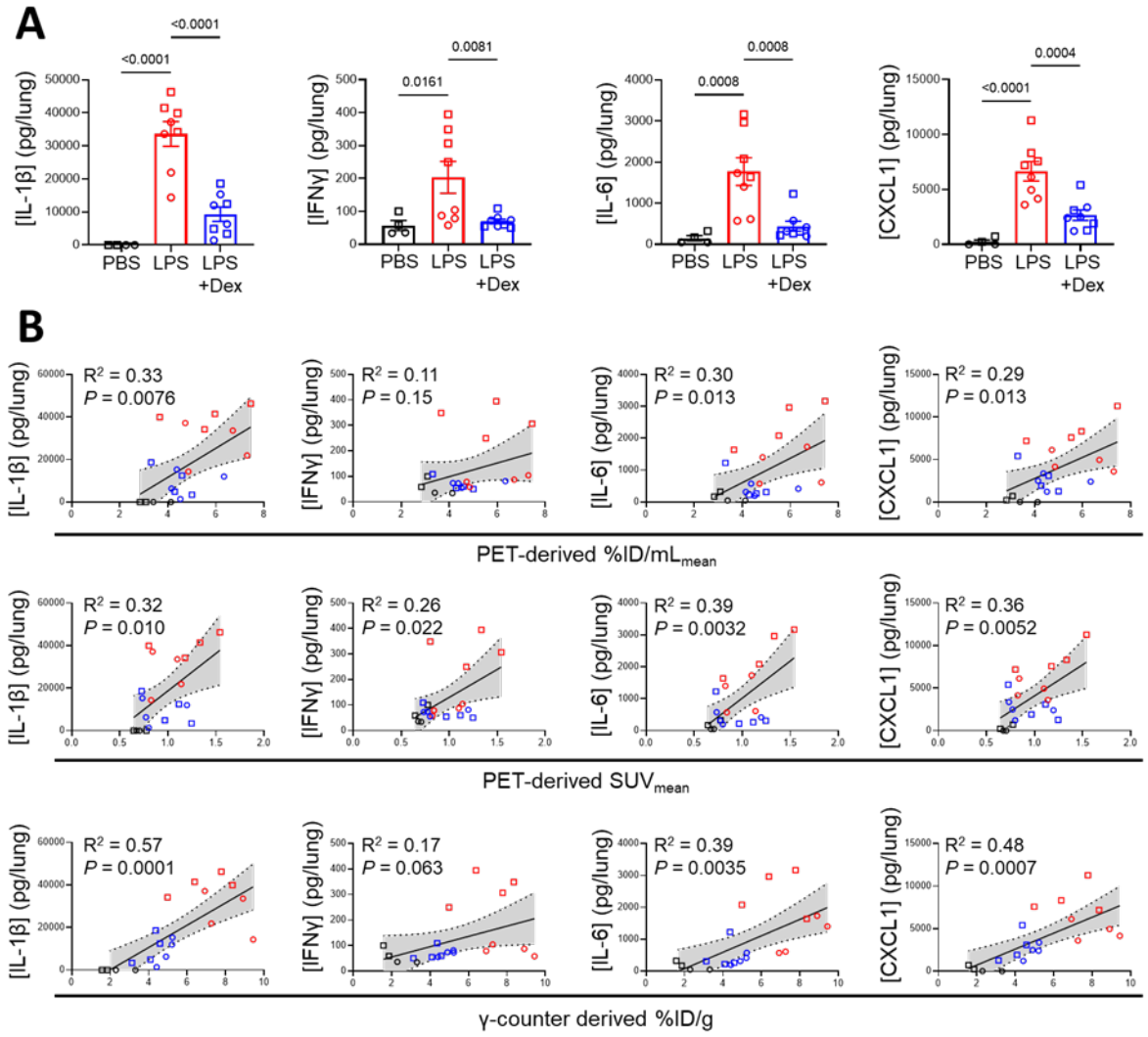

Figure 7. PET-derived [^{18}F]FDG uptake correlates with protein expression of inflammatory markers.

(**A**) The protein expression of select markers was determined with an enzyme-linked immunosorbent assay following PET/CT. (**B**) Expression of inflammatory cytokines/chemokines was correlated with PET-derived (Top: %ID/mL$_{mean}$ or Middle: SUV$_{mean}$) and γ-counter-derived (Bottom) [^{18}F]FDG uptake. N = 4 PBS, 8 LPS, and 8 LPS+Dex treated mice. Equal numbers of male (squares) and female (circles) mice were used per group. Abbreviations: PBS = phosphate buffered saline, LPS = lipopolysaccharide, Dex = dexamethasone.

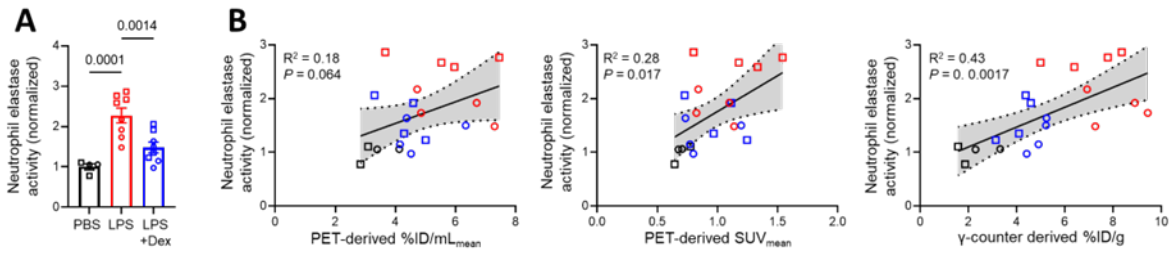

Figure 8. Pulmonary [^{18}F]FDG uptake correlates with neutrophil elastase activity.

(**A**) Neutrophil elastase activity was determined in lung homogenates following PET/CT. The total neutrophil elastase activity is increased following intratracheal instillation of LPS and decreases nearly to baseline with dexamethasone treatment. The neutrophil elastase activity of LPS and LPS+Dex groups was normalized to the average of the controls. (**B**) Neutrophil elastase activity was correlated with PET-derived (Left: %ID/mL$_{mean}$ or Middle: SUV$_{mean}$) or γ-counter-derived (Right) [^{18}F]FDG uptake. N = 4 PBS, 8 LPS, and 8 LPS+Dex treated mice. Equal numbers of male (squares) and female (circles) mice were used per group. Abbreviations: PBS = phosphate buffered saline, LPS = lipopolysaccharide, Dex = dexamethasone.

As several inflammatory stimuli inhibit the tricarboxylic acid cycle, many leukocytes in inflammatory environments rely on glycolysis for energy production and proper inflammatory functions (94-98). Further, a switch to glycolysis with an associated increase in lactate production represents a validated metabolic alteration and poor clinical prognostic factor in ARDS (99-106). We therefore examined whether [^{18}F]FDG uptake correlates with pulmonary glycolytic activity of HK and LDH. We focused on HK and LDH as they represent important steps in glycolysis; HK traps glucose and [^{18}F]FDG intracellularly via phosphorylation whereas LDH catalyzes the critical final step of glycolysis to regenerate NAD+ to sustain high levels of glycolysis. Following LPS treatment, we found that the relative activity of HK and LDH were both significantly increased over that of controls (Figure 9). Interestingly, dexamethasone decreased HK and LDH activities to the levels of control mice. Further, the HK and LDH activity both generally correlated with

[^{18}F]FDG uptake, although most strongly with *ex vivo* γ-counting-derived measurements (Figure 9).

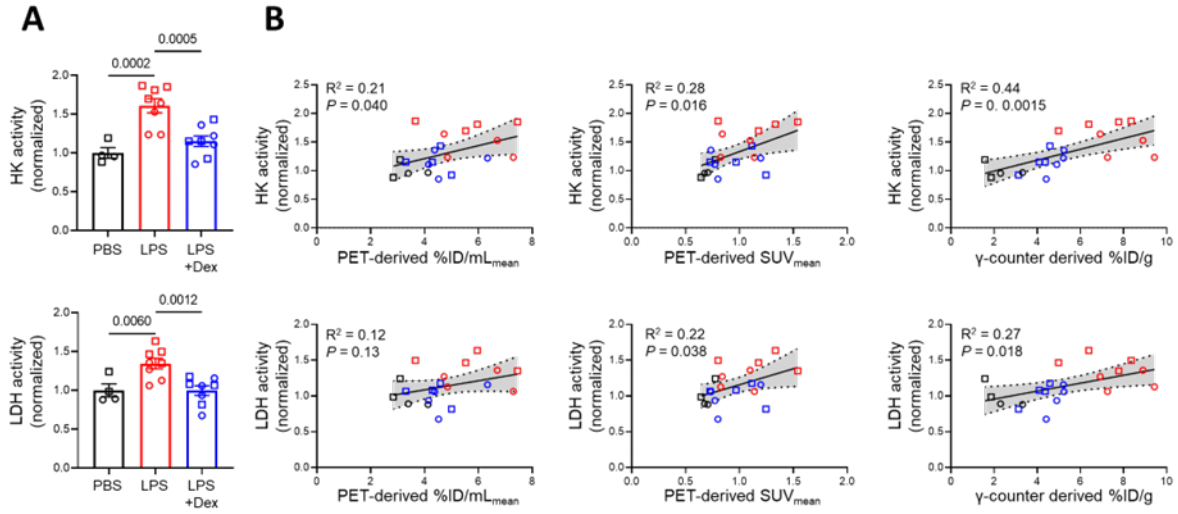

Figure 9. [^{18}F]FDG uptake correlates with the activity of glycolytic enzymes.

(**A**) The activity of hexokinase (HK) and lactate dehydrogenase (LDH) in lung homogenates was measured following PET/CT. The total lung activity of both enzymes was significantly increased following administration of LPS. Anti-inflammatory treatment by dexamethasone reduced the activity of HK and LDH nearly to that of controls. Enzymatic activity was normalized to that of the average of the controls. (**B**) HK and LDH activities were correlated with PET-derived (Left: %ID/mL$_{mean}$ or Middle: SUV$_{mean}$) or γ-counter-derived (Right) [^{18}F]FDG uptake. N = 4 PBS, 8 LPS, and 8 LPS+Dex treated mice. Equal numbers of male (squares) and female (circles) mice were used per group. Abbreviations: PBS = phosphate buffered saline, LPS = lipopolysaccharide, Dex = dexamethasone.

2.4.4 Neutrophil burden in the lungs mirrors the observed pattern of [^{18}F]FDG uptake in LPS-induced ALI and response to anti-inflammatory treatment

To determine changes in pulmonary immune cell populations in response to LPS administration with or without dexamethasone treatment, we first determined the absolute cell

count for individual cell types harvested from the lungs (Figure 10) using a flow cytometry gating strategy provided in Fig. S1. Following LPS-treatment, we detected significantly increased numbers of lung neutrophils (e.g., ~60-fold increase) versus that of control mice (P = 0.0008) (Figure 10). However, LPS induced only modest increases in the number of several other lung immune cell populations, including interstitial and monocyte-derived macrophages. We found that dexamethasone treatment reduced the number of infiltrating neutrophils without affecting the abundance of other cell populations. Additionally, we observed minimal changes to the number of lymphoid cells (B-cells, natural killer cells, and T-cells), monocytes ($Ly6C^{hi}$ and $Ly6C^{lo}$), dendritic cells ($CD11b^{hi}$ and $CD11b^{lo}$), eosinophils, and $CD45^{neg}$ non-immune cells after treatment with LPS or dexamethasone versus that of controls.

We next calculated the relative contributions of individual cell types to the total pulmonary cell counts under different treatment conditions (Figure 10). Unsurprisingly, LPS-treated mice exhibited the highest number of total lung cells, with neutrophils accounting for over half of all cells in the lungs of mice with LPS-induced ALI. Dexamethasone therapy decreased the number of lung leukocytes largely due to a decrease in the number of neutrophils. By contrast, neutrophils represented only 2% of all cells in the control lungs. As the changes in $CD45^{neg}$ cells and other leukocyte populations were relatively minor compared to that of the neutrophils, the change in total cell count was driven primarily by neutrophils. Furthermore, we observed the total cell count measured by flow cytometry in different experimental groups (Figure 10) closely mirrored that of [^{18}F]FDG uptake under the same treatment conditions (Figure 6). Unsurprisingly, $CD45^{neg}$ cells represent a significant fraction of total lung cells under all conditions and are presumably a major contributor to [^{18}F]FDG uptake in healthy lungs.

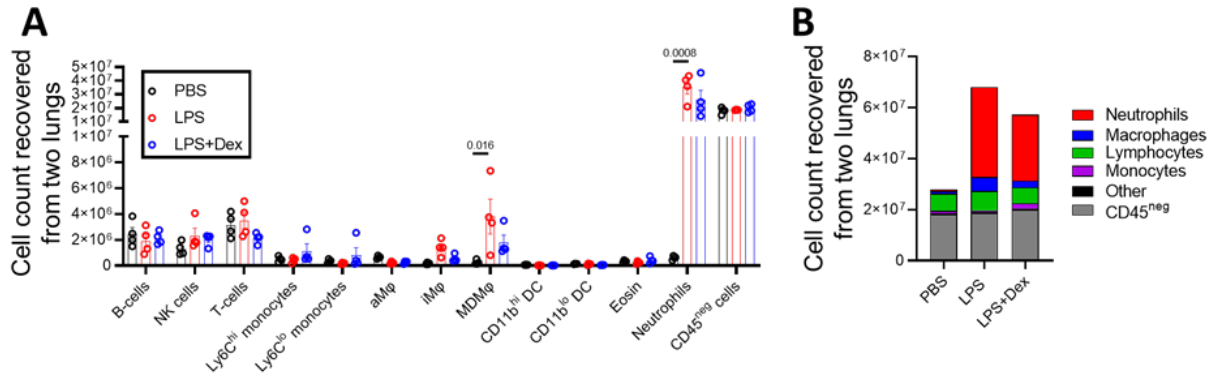

Figure 10. Neutrophils are the most abundant cell type during LPS-induced ALI as measured by flow cytometry.

(**A**) The cell count was quantified for mice treated with intratracheal LPS or LPS+Dex vs. control. (**B**) The relative contribution of individual cell types to the total recovered cells from the lungs of mice following treatment with LPS and/or dexamethasone versus control, as visualized with a stacked-bar graph. Abbreviations: NK cells = natural killer cells; aMφ = alveolar macrophage; iMφ = interstitial macrophage; MDMφ = monocyte-derived macrophage; $CD11b^{hi}$ DC = $CD11b^{hi}$ dendritic cells; $CD11b^{lo}$ DC = $CD11b^{lo}$ dendritic cells; Eosin = eosinophils; $CD45^{neg}$ cells = non-immune cells . N = 4 PBS, 4 LPS, and 4 LPS+Dex treated mice. Equal numbers of male and female mice were used per group. Abbreviations: PBS = phosphate buffered saline, LPS = lipopolysaccharide, Dex = dexamethasone.

2.5 Discussion

In this study, we demonstrate that [^{18}F]FDG uptake is increased in LPS-induced ALI and noninvasively detects the response to a clinically relevant anti-inflammatory therapy, dexamethasone. We found that [^{18}F]FDG uptake during ALI with or without dexamethasone treatment correlates with the degree of inflammatory cytokine/chemokine expression and the activity of neutrophil elastase and glycolytic enzymes. We further found that [^{18}F]FDG uptake closely mirrors the pattern of pulmonary neutrophil accumulation during ALI, and the dominant

immune cell population in this model. Thus, [^{18}F]FDG PET is effective in monitoring ongoing and resolving lung inflammation through its correlations with lung specific expression of inflammatory biomarkers and active neutrophils.

While the pathophysiology of ARDS/ALI is complex, we demonstrate that [^{18}F]FDG PET noninvasively and directly monitors specific aspects of the inflammatory response in the lung that are difficult to obtain via other available techniques. We show that [^{18}F]FDG uptake correlates with pathogenically relevant and therapeutically targetable biomarkers expressed in lung tissue, which may prove advantageous over measurement of serum biomarkers that may reflect systemic rather than lung specific inflammatory processes. Importantly, we found that [^{18}F]FDG uptake monitors the anti-inflammatory response to dexamethasone therapy, as confirmed by correlations between reduced radiotracer uptake with decreased expression of inflammatory mediators, including cytokines, chemokines, and proteases. Furthermore, [^{18}F]FDG PET more accurately visualizes the response to anti-inflammatory treatment compared to that of CT, as demonstrated by reduced [^{18}F]FDG uptake in regions of CT-defined pulmonary airspace opacification following steroid therapy.

Despite the widespread use of and research on [^{18}F]FDG for imaging inflammation, there remain biologic and technological limitations that may hinder interpretability of [^{18}F]FDG for monitoring ongoing lung inflammation. For example, both clinical and preclinical studies have shown that all metabolically active cells metabolize [^{18}F]FDG, including the liver, ribs, heart, and brown fat (107-110). Due to the positron range and scattered radiation, the high radiotracer uptake in extra-pulmonary tissues, enhanced by the systemic inflammation induced by LPS, appears to

"spillover" into the lungs, and leads to overestimation of the true extent of pulmonary [^{18}F]FDG uptake by PET in regions adjacent to organs with high [^{18}F]FDG uptake. In preclinical experiments, the combination of respiratory motion from non-respiratory gated scans and small subject size further enhances the undesirable impact of the relatively high positron range and scatter, ultimately leading to inaccurate assessments of pulmonary radiotracer uptake. These limitations may account for the moderate correlation between *ex vivo* γ-counting (%ID/g) derived [^{18}F]FDG uptake and *in vivo* PET %ID/mL$_{mean}$ and fair correlation between *ex vivo* γ-counting (%ID/g) derived [^{18}F]FDG uptake and *in vivo* PET SUV$_{mean}$. The lower correlation strength of SUV$_{mean}$ with γ-counting-derived uptake values may result from the weight loss in LPS-treated mice that lowers the SUV$_{mean}$ (111-114). As the %ID/mL does not account for weight changes, we observed a stronger correlation between PET-derived %ID/mL$_{mean}$ and γ-counting derived %ID/g. Notably, the correlations between [^{18}F]FDG uptake and biological markers in our study were generally strongest when tracer uptake was assessed by *ex vivo* γ-counting, consistent with the inaccuracies of *in vivo* PET-derived measurements. While the larger size of humans and implementation of respiratory gating in clinical scans reduce the above mentioned effects, the non-specific [^{18}F]FDG uptake by the heart, liver, and ribs may obscure inflammatory processes in the lung periphery and subpleural space.

Although [^{18}F]FDG PET is the most popular molecular imaging approach for assessment of inflammation, there remains a clear need to develop new radiotracers targeting specific aspects of the inflammatory process. In particular, our study demonstrates that [^{18}F]FDG uptake is likely driven by abundant, metabolically active cell types, e.g., neutrophils in the case of ALI (48, 49, 65, 115, 116), with probable contributions from lung parenchymal cells. Additionally, prior studies

have shown that neutrophils contribute to most [^{3}H]deoxyglucose uptake among the cells recovered from BAL of humans intrabronchially administered with LPS (48, 78)**.** To address the non-specificity of [^{18}F]FDG, selective PET agents have been developed to study specific inflammatory pathways, particularly monocyte/macrophage-driven inflammation. For instance, the PET tracer [^{64}Cu]DOTA-ECL1i is reported to target CCR2-expressing monocytes (53, 56), which have been demonstrated to be relevant in pulmonary inflammation and noninvasively monitors response to immunotherapies. Additionally, we have recently reported that [^{64}Cu]NODAGA-CG34, a PET tracer that selectively binds to chemokine-like receptor-1 (CMKLR1), detects the accumulation of monocyte-derived macrophages in the lungs of mice with ALI (22). Other emerging molecular imaging targets include, $\alpha_4\beta_1$ integrin (117), leukocyte receptor CD11b (118), folate receptor-β (55), and translocator protein receptor (119), which have been successfully used for noninvasive detection of lung inflammation in ALI.

There remain several limitations of our current study. First, as previously mentioned, the high degree of [^{18}F]FDG uptake in lung-adjacent tissues results in the spillover of radiotracer signal into the lungs, as measured by PET. To minimize the unwanted contribution from these non-lung organs to the lung [^{18}F]FDG uptake, we drew our regions of interest to include a few millimeter margins between the lung and adjacent organs, leading to underestimation of lung radiotracer uptake. Another limitation of our study is that we measured a relatively limited number of inflammatory and glycolytic markers with which to correlate [^{18}F]FDG uptake. We chose to measure these chemokines, cytokines, and enzymes as they are common biomarkers characterizing the inflammatory response observed in experimental ALI (88). Additionally, decreased blood flow to areas of lung inflammation due to hypoxia-induced vasoconstriction (120) is expected to affect

the observed [^{18}F]FDG uptake. Kinetic analysis of [^{18}F]FDG uptake along with perfusion PET imaging allows for a more accurate measurement of the rate of [^{18}F]FDG uptake. However, the static PET design of our approach is aligned with our primary goal to determine the utility of the [^{18}F]FDG PET according to the currently performed clinical protocols to monitor lung inflammation and response to therapy.

In conclusion, [^{18}F]FDG PET may be useful in monitoring ongoing pulmonary inflammation and therapeutic response. Additionally, our data along with the previous publications (48, 78) suggest that [^{18}F]FDG uptake is mostly driven by the metabolic activity of neutrophils in this preclinical model of ALI, and is less reflective of other specific subsets of immune cells. While our results should encourage additional work into better understanding the biological correlations of [^{18}F]FDG uptake, there remains a clear need to develop new radiotracers targeting specific aspects of the inflammatory process and better understand the biologic correlates of molecular imaging.

3.0 Molecular Imaging of Chemokine-Like Receptor 1 (CMKLR1) in Experimental Acute Lung Injury

The work presented in this chapter has been previously published the *Proceedings of the National Academy of Sciences* (PNAS) (22), and I am the first author of the manuscript. PNAS does not require authors to obtain permission for use of articles in their dissertations.

This study was supported by the following grants: National Institute of Biomedical Imaging and Bioengineering (NIBIB, R21EB027871) and National Heart, Lung, and Blood Institute (NHLBI, K08HL144911) to Sina Tavakoli; NHLBI (F30HL158038) to Philip Mannes; NHLBI (R01HL136143, P01HL114453, R01HL142084, and K24HL143285) to Janet Lee; and National Cancer Institute (NCI, K08CA222663, R21CA263381, and R37CA258829), Burroughs Wellcome Fund (Career Award for Medical Scientists), and Fast Grant for COVID-19 research to Benjamin Izar. This work utilized the Hillman Cancer Center In Vivo Imaging Facility, a shared resource at the University of Pittsburgh (supported by P30CA047904).

3.1 Abstract

The lack of techniques for noninvasive imaging of inflammation has challenged precision medicine management of acute respiratory distress syndrome (ARDS). Here, we determined the potential of positron emission tomography (PET) of chemokine-like receptor-1 (CMKLR1) to monitor lung inflammation in a murine model of lipopolysaccharide-induced injury. Lung uptake of a CMKLR1-targeting radiotracer, [^{64}Cu]NODAGA-CG34, was significantly increased in

lipopolysaccharide-induced injury, correlated with the expression of multiple inflammatory markers, and reduced by dexamethasone treatment. Monocyte-derived macrophages, followed by interstitial macrophages and monocytes were the major CMKLR1-expressing leukocytes contributing to the increased tracer uptake throughout the first week of lipopolysaccharide-induced injury. The clinical relevance of CMKLR1 as a biomarker of lung inflammation in ARDS was confirmed using single-nuclei RNA-sequencing datasets which showed significant increases in *CMKLR1* expression among transcriptionally distinct subsets of lung monocytes and macrophages in COVID-19 patients vs. controls. CMKLR1-targeted PET is a promising strategy to monitor the dynamics of lung inflammation and response to anti-inflammatory treatment in ARDS.

3.2 Introduction

Acute lung injury (ALI) is a heterogeneous life-threatening condition which is caused by diffuse alveolar damage and manifests as acute hypoxemic respiratory failure and non-cardiogenic pulmonary edema, clinically referred to as the acute respiratory distress syndrome (ARDS). With an annual incidence of ~75 per 100,000 individuals and a mortality rate of 27-45%, ARDS has long been a major healthcare issue (121). This has been drastically aggravated during the current pandemic, as ARDS occurs in ~5% of patients with COVID-19 and accounts for most of its fatalities (122).

The disruption of the alveolar-capillary barrier in ALI may occur following direct exposure to various biological, chemical, and physical hazards, or indirect injuries, e.g., sepsis (3, 123, 124).

Despite the etiological heterogeneity of the triggering events, dysregulated inflammation is a critical driver of ALI/ARDS and its progression to the fibroproliferative phase (3). Therefore, detection of the inter-individual heterogeneity of the immune response plays a crucial role in understanding the pathophysiology of ALI/ARDS and promoting a precision medicine approach through predicting the clinical trajectory of disease in individual patients and monitoring their responses to various anti-inflammatory therapies (90, 125, 126).

The current clinical methods to characterize lung inflammation have significant limitations. Invasive techniques, like lung biopsy, pose significant risks to critically ill patients and are subject to sampling bias (127). Additionally, the available plasma biomarkers of inflammation are non-specific, and their alterations may be related to extra-pulmonary processes (128). Molecular imaging, by contrast, can non-invasively provide spatially-resolved information about pathological processes contributing to lung inflammation (129). Early molecular imaging studies of lung inflammation were mostly focused on [^{18}F]fluorodeoxyglucose ([^{18}F]FDG) positron emission tomography (PET), which relies on the detection of enhanced glucose utilization by activated leukocytes (129). However, the non-specificity of [^{18}F]FDG uptake has prompted the development of novel tracers targeting more specific aspects of the immune response (85, 130). Notably, pre-clinical studies have shown the feasibility of targeted imaging of C-C motif chemokine receptor-2 (CCR2) (53), very late antigen-4 (VLA4) (117), CD11b (118), and folate receptor-β (55) in ALI, each depicting a different aspect of lung inflammation. However, no single molecular imaging strategy can capture the complexity of the immune response and the substantial heterogeneity of ARDS as major barriers to clinical implementation of therapies targeting different aspects of disease pathogenesis, e.g., immunomodulatory/immunosuppressive or anti-fibrotic

drugs, in individual patients (131). For example, while targeted imaging of CCR2 allows for the detection of ongoing influx of monocytes, CCR2 downregulation upon monocyte-to-macrophage differentiation (132, 133) may limit the utility of this approach in inflammatory conditions driven by local proliferation or sustained activation of the accumulated macrophages. Therefore, continued development and validation of novel tracers that target diverse aspects of the immune response are critical to establish a multi-pronged approach for characterizing disease endotypes, ultimately leading to the precision management of ALI/ARDS.

Chemokine-like receptor 1 (CMKLR1) is a G-protein coupled receptor for chemerin and resolvin E1, which plays key roles in recruitment and activation of macrophages, natural killer cells, and plasmacytoid dendritic cells in inflammatory diseases across multiple organs, including atherosclerosis (134, 135), rheumatoid arthritis (136), and inflammatory bowel disease (45). With respect to the lungs, CMKLR1 has been shown to contribute to the inflammation induced by cigarette smoke (38), traffic-related particles (39), viral pneumonia (37) and ALI (21) in pre-clinical models. Moreover, a comprehensive single-cell transcriptomic study has recently shown the expression of *CMKLR1* by a subset of monocyte-derived macrophages in patients with COVID-19 ARDS (137), which supports the clinical relevance of CMKLR1 as a biomarker of lung inflammation in ARDS.

In this study, we hypothesized that molecular imaging of CMKLR1, as a biomarker of lung inflammation, is feasible and allows for non-invasive quantitative detection of ongoing lung inflammation in an experimental model of ARDS. We describe the development and validation of a new CMKLR1-targeting radiotracer, based on a recently discovered high-affinity and

proteolytically stable peptidomimetic analog of the carboxyl terminus of chemerin (referred to as CG34) (31), for PET imaging of lung inflammation in a murine model of lipopolysaccharide (LPS)-induced ALI and monitoring the therapeutic response to dexamethasone, as a clinically relevant intervention in ARDS. Additionally, we establish the biological correlates of this imaging approach by determining the relationship between tracer uptake and the expression of multiple markers of lung inflammation, and by immunophenotyping of CMKLR1-expressing leukocytes contributing to tracer uptake in experimental ALI. We further characterize the kinetics of CMKLR1 expression over the course of LPS-induced ALI and compare the pattern to that of CCR2. Finally, we address the clinical relevance of CMKLR1 as a biomarker in ARDS by determining the expression of CMKLR1 in lungs of patients with COVID-19 *vs.* controls by secondary analysis of a single-nuclei RNA-sequencing (snRNA-seq) dataset (138).

3.3 Methods

3.3.1 Chemicals and reagents

The major chemicals and reagents (Supplemental Table 6), plasmids (Supplemental Table 7), HPLC methods (Supplemental Table 8), flow cytometry reagents (Supplemental Table 9), histology antibodies (Supplemental Table 10), Taqman primers (Supplemental Table 11), and details of publicly available single-cell RNA sequencing datasets (Supplemental Table 12) are listed in the Supplementary Information. Chemical characterization of NODAGA-CG34 is shown in Appendix Figure 26.

3.3.2 Cell culture

HeLa cells transiently transfected with mouse CMKLR1 and/or $G_{\alpha 15}$ cDNA plasmids were used for calcium flux or radioligand binding assays. Resident peritoneal cells harvested from C57BL/6J mice via peritoneal lavage (139), were used to determine the binding/uptake of 6CF-$Chem_{145\text{-}157}$ by flow cytometry.

3.3.3 Radiolabeling

Radiolabeling of NODAGA-CG34 was performed in 0.5 M NaOAc buffer (pH = 6.9 and 0.8 mM gentisic acid dissolved in water) by adding [^{64}Cu]$CuCl_2$ in 0.1 M HCl (37 MBq per 1.0 nmol of NODAGA-CG34) and incubation at 40 °C for 30 minutes. The radiochemical purity of [^{64}Cu]NODAGA-CG34 was determined by radio-HPLC to confirm a minimum purity of >95% prior to use in all *in vitro* (measurement of octanol/water partition coefficient (logD), radiolysis and plasma stability assays, and plasma protein binding assay) and *in vivo* (PET/CT) experiments. Relevant radio-HPLC methods are described in Supplemental Table 8.

3.3.4 Mouse model of experimental lung injury

Animal experiments were performed on C57BL/6J mice under a protocol approved by the University of Pittsburgh Institutional Animal Care and Use Committee. Adult 9- to 12-week-old C57BL/6J mice were used throughout the study. Mice were administered intratracheally with 2.5

µg/g LPS from *Escherichia coli* O111:B4 in 60 µl of phosphate-buffered saline (PBS) to induce lung injury (117). Control mice were intratracheally injected with 60 µl of PBS. In experiments involving anti-inflammatory treatment, mice receiving dexamethasone were given two doses of 10 mg/kg (in 500 µL in PBS) via intraperitoneal injections at 1 and 24 hours following LPS instillation, whereas control mice were treated with intraperitoneal PBS (500 µL) injections.

3.3.5 PET/CT and quantification of [^{64}Cu]NODAGA-CG34 uptake

Mice were injected intravenously with [^{64}Cu]NODAGA-CG34 (6.41±0.05 MBq). Tracer specificity was addressed by co-injection of [^{64}Cu]NODAGA-CG34 and 100-fold molar excess of non-radiolabeled NODAGA-CG34. Static PET (~10-min) and CT (180 projections, 140-msec exposure, 180° rotation, 80-kVp, 500-µA, field-of-view: 78.5 x 100-mm) were performed, according to our previous experiments (117) (Inveon, Siemens), 90 minutes after [^{64}Cu]NODAGA-CG34 injection.

Regions of interest were drawn over the left and right lungs, and the uptake in the left and right lungs of [^{64}Cu]NODAGA-CG34 was averaged and quantified as the mean and maximal standardized uptake value (SUV_{mean} and SUV_{max}) (IRW software). Biodistribution was performed by γ-counting (Wizard2, PerkinElmer) of harvested organs. Data are reported as percentage of injected dose per gram tissue (%ID/g) after decay correction. Multiplanar reformats of PET/CT images were performed (Vivoquant software) to reconstruct planes matching the autoradiography and histology images.

3.3.6 Gene expression assays

Following PET/CT, the lungs of mice were harvested and stored frozen for >10 half-lives of [^{64}Cu]NODAGA-CG34 prior to use for gene expression assays using TaqMan primers according to standard methods (117). All transcript levels were normalized to the expression level of 18S ribosomal RNA (*Rn18s*).

3.3.7 Flow cytometric immunophenotyping of murine lungs

Mechanically dissociated cells from murine lungs were incubated in the absence or presence of 6CF-Chem$_{145\text{-}157}$ (100 nM) with or without co-incubation with Chem$_{145\text{-}157}$ (10 μM) at 37 °C for 1 hour. After washing with PBS and blocking of nonspecific binding using 1% BSA and Fc block, a mixture of antibodies and DAPI was added for 0.5 hour at 4 °C. Cells were then washed and fixed for flow cytometry.

3.3.8 Lung immunostaining

Murine lung cryosections were incubated with primary antibodies (1:200, 4 °C, overnight) prior to incubation with fluorescently-conjugated secondary antibodies (1:200, 4 °C, 2 hours) and mounting.

3.3.9 snRNA-seq of COVID-19 and control lungs

A secondary analysis of a previously published snRNA-seq dataset from the autopsied lungs

of nineteen patients with lethal COVID-19 and lung tissue (biopsy or lung resection) from seven pre-pandemic control patients without COVID-19 was performed to determine the expression of *CMKLR1* among different cell types in the lungs. The RNA sequencing data are available in the Gene Expression Omnibus (GEO) database under accession number GSE171524. Data collection, analysis and UMAP identification of major cell populations were conducted as previously reported (138). Differential gene expression was performed using the Seurat (v4.1.0) (140).

3.3.10 Analysis of additional publicly available human scRNA-seq datasets

CMKLR1 expression by different immune cells were determined across different organs through secondary analysis of separate independently published scRNA-seq datasets (GEO accession numbers GSE145926, GSE193782, and GSE201333, or European Genome-Phenome Archive accession number EGAS00001004481) using the UCSC Cell Browser software (available at: https://cells.ucsc.edu/) (141-145).

3.3.11 Statistical analysis

Statistical analysis was performed using Prism 9 (GraphPad). Data are presented as mean ± SEM. A student's *t*-test was performed to compare the means values between two groups. One-way analysis of variance, followed by Fisher's Exact post hoc test, was used to compare mean values in > 2 groups. Pearson's test was used to determine the correlations between continuous variables. For snRNA-seq data, the percentage of cells positive for *CMKLR1* and the average *CMKLR1* expression in different cell subsets were compared between COVID-19 and control groups using Fisher's Exact and Wilcoxon rank-sum tests, respectively. Statistical significance

was considered as $P < 0.05$.

3.3.12 Supplemental methods

Additional details on materials and methods are provided in Appendix B.

3.4 Results

3.4.1 NODAGA-CG34 is a potent CMKLR1 agonist

To achieve site-specific [^{64}Cu]Cu^{+2} radiolabeling of CG34, a high-affinity (i.e. low nanomolar) human CMKLR1 agonist (31), we conjugated the N-terminus of CG34 with NODAGA, a chelator with favorable *in vivo* pharmacokinetics, through a 6-aminohexanoic acid linker (Appendix Figure 25 and Appendix Figure 26). To confirm that NODAGA-6-aminohexanoic acid conjugation did not impair CG34 functionality, calcium flux assays were performed in HeLa cells expressing mouse CMKLR1 (mCMKLR1) and G-protein alpha-15 ($G_{\alpha 15}$) *vs.* $G_{\alpha 15}$ alone (Appendix Figure 25 and Appendix Figure 27). The potency of NODAGA-CG34 in eliciting CMKLR1-specific response was comparable to that of a high-affinity peptide derived from amino acids 145-157 of chemerin ($Chem_{145\text{-}157}$, Appendix Figure 28) with EC_{50} of 45.7 *vs.* 42.2 nM, respectively (Appendix Figure 25).

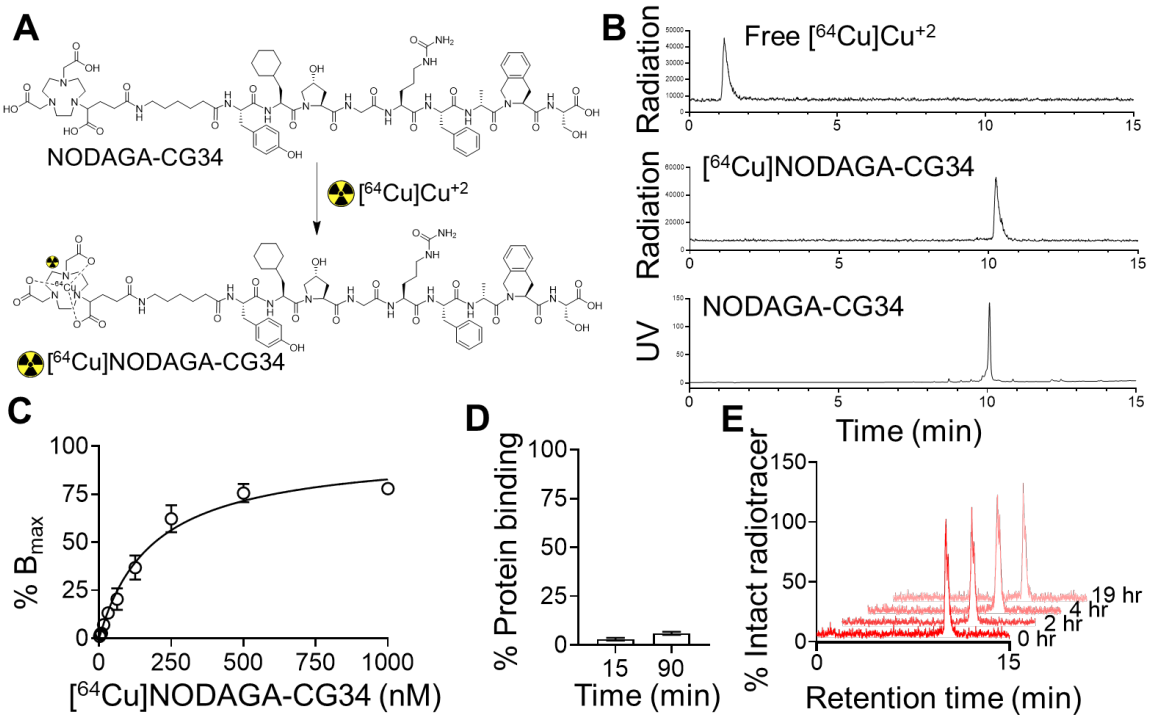

Figure 11. Radiolabeling of NODAGA-CG34 and select *in vitro* pharmacologic properties of [^{64}Cu]NODAGA-CG34.

(**A**) Radiolabeling of NODAGA-CG34 was performed by its incubation with [^{64}Cu]$CuCl_2$ in sodium acetate buffer containing gentisic acid at 40 °C for 30 min. (**B**) Radiolabeling efficiency >95% is consistently achieved as confirmed by radio-HPLC as a quality control threshold for proceeding to downstream experiments. Radio-HPLC of free [^{64}Cu]Cu^{+2} (top panel) has a retention time of ~1.2 minutes *vs.* [^{64}Cu]NODAGA-CG34 (middle panel) with a retention time of 10.2 minutes. Unlabeled NODAGA-CG34 (lower panel) demonstrates a similar retention time by HPLC, as measured by UV detection, to that of [^{64}Cu]NODAGA-CG34. (**C**) A saturation binding curve demonstrates specific (total minus non-specific) binding of [^{64}Cu]NODAGA-CG34 to mCMKLR1 in HeLa cells transiently transfected with mCMKLR1 with a K_d of 192.1 ± 28.6 nM. Total and non-specific binding were conducted in the absence or presence of 2.5 μM $Chem_{145-157}$, respectively. (**D**) The plasma protein binding of [^{64}Cu]NODAGA-CG34 was determined by separation of bound and free [^{64}Cu]NODAGA-CG34 using a size-exclusion column following by γ-counting at specified time points. (**E**) Representative radio-HPLC chromatograms demonstrate high (~100%) *in vitro* stability of [^{64}Cu]NODAGA-CG34 in mouse plasma at different time-points over a 19-hour period. N = 3 independent

experiments for all experiments, except for radiolabeling which has been performed >10 times. Data are expressed as the mean ± SEM.

3.4.2 [^{64}Cu]NODAGA-CG34 exhibits a favorable *in vitro* profile for CMKLR1-targeted PET

Radiolabeling of NODAGA-CG34 with [^{64}Cu]Cu^{+2} consistently provided [^{64}Cu]NODAGA-CG34 with radiochemical yields >95% at a molar activity of ~37 MBq/nmol (Figure 11). Radioligand binding assays demonstrated a high affinity of [^{64}Cu]NODAGA-CG34 to mCMKLR1 with a dissociation constant (K_d) of 192.1 nM (Figure 11), which is further enhanced by the cellular internalization of CMKLR1 agonists (146).

[^{64}Cu]NODAGA-CG34 is highly hydrophilic with an 1-octanol/PBS partition coefficient (logD) of -2.86 ± 0.08. Additionally, [^{64}Cu]NODAGA-CG34 demonstrated low plasma protein binding both at 15 minutes (3.0% ± 0.7) and 90 minutes (6.0% ± 0.8) (Figure 11).

Radio-HPLC of [^{64}Cu]NODAGA-CG34 after overnight incubation in radiolabeling buffer under ambient conditions did not reveal any additional radioactive peaks (Appendix Figure 29), confirming its stability to both radiolysis and radiometal chelation. Additionally, radio-HPLC of [^{64}Cu]NODAGA-CG34 after extended incubation in mouse plasma revealed no detectable radiometabolites, indicating its excellent plasma stability (Appendix Figure 29).

3.4.3 [^{64}Cu]NODAGA-CG34 PET quantitatively detects lung inflammation

Visual assessment of PET/CT demonstrated both diffuse and distinct focal lung uptake of [^{64}Cu]NODAGA-CG34 in regions of airspace opacification two days after the induction of ALI, which were blocked by co-administration of unlabeled NODAGA-CG34 (Figure 12 and Appendix Figure 30). Consistent with this qualitative assessment, the maximum and mean standardized uptake values (SUV_{max} and SUV_{mean}) of [^{64}Cu]NODAGA-CG34 were ~1.7-fold higher in ALI compared to control lungs (Figure 12). A marked reduction in SUV_{max} and SUV_{mean} in mice co-injected with excess unlabeled NODAGA-CG34 confirmed the *in vivo* specificity of [^{64}Cu]NODAGA-CG34 uptake (Figure 12).

Similarly, *ex vivo* γ-counting determined that lung uptake of [^{64}Cu]NODAGA-CG34 was ~2-fold higher in ALI mice as compared to controls and was blocked by co-injection of unlabeled NODAGA-CG34 (Figure 12). We verified the accuracy of PET-derived quantification of [^{64}Cu]NODAGA-CG34 uptake by demonstrating a strong correlation between SUV_{mean} and γ-counting measurements of [^{64}Cu]NODAGA-CG34 uptake (R^2=0.53, P=0.0006) (Figure 12).

Consistent with prior reports of systemic inflammation associated with intratracheal LPS-induced ALI (53, 117, 118), significant increases in [^{64}Cu]NODAGA-CG34 uptake were present in several organs (particularly liver, spleen, thymus, and intestine) in ALI mice compared to controls (Fig. 2F).

To validate the accuracy of [^{64}Cu]NODAGA-CG34 PET as an imaging biomarker of lung inflammation, we determined the correlations between lung SUV_{mean} and mRNA expression of

inflammatory markers. ALI substantially increased the expression of multiple inflammation-associated genes, including chemokines, interleukins, and cytokines, in the lungs (Appendix Figure 31), many of which significantly correlated with SUV_{mean} (Appendix Figure 31).

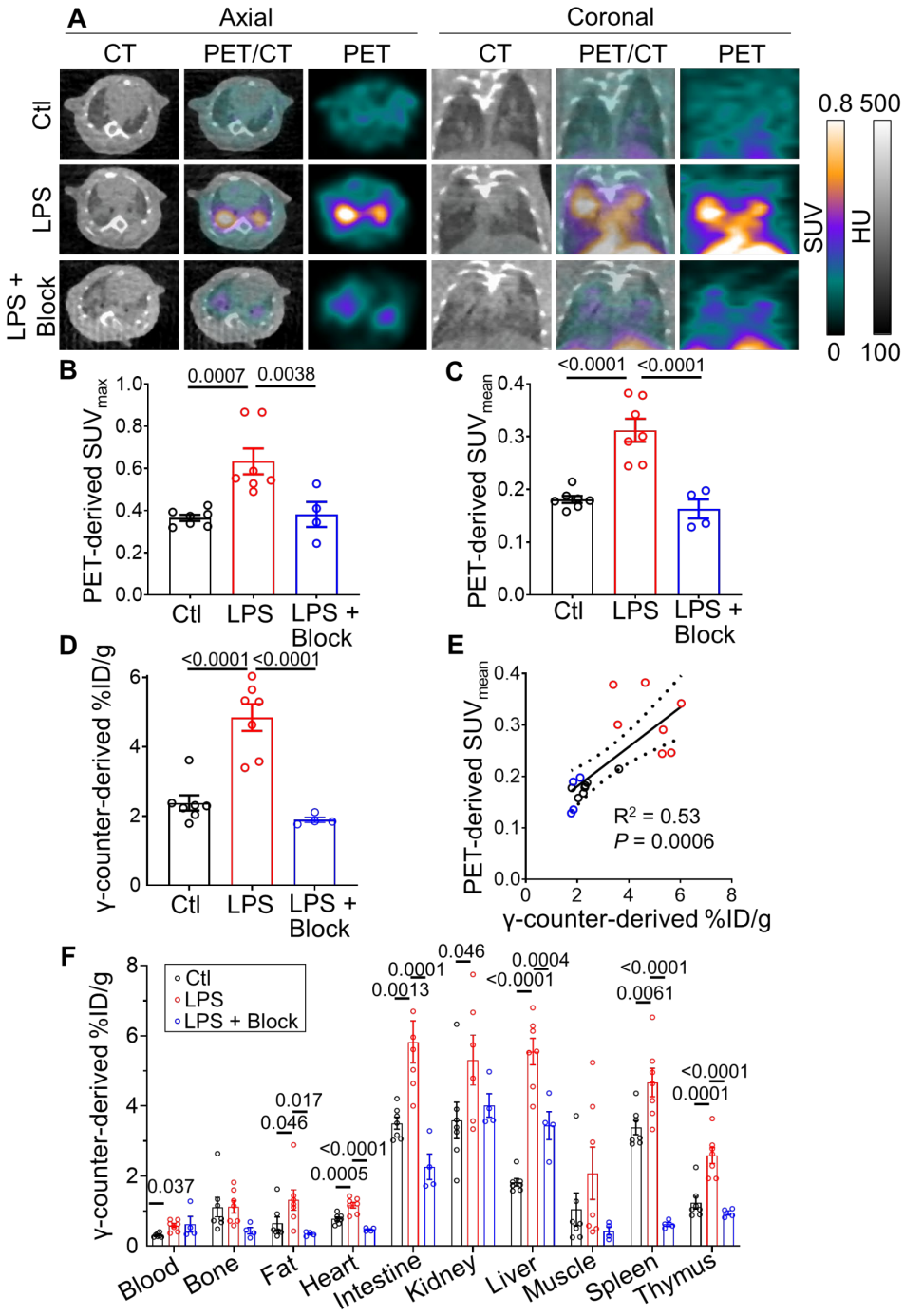

Figure 12. [^{64}Cu]NODAGA-CG34 PET/CT in LPS-induced lung injury.

(**A**) Representative axial (left) or coronal (right) CT, PET and co-registered PET/CT images acquired ~90 minutes after intravenous tracer injection from a control mouse (top row) *vs.* a mouse 2 days after intratracheal LPS administration (middle row) demonstrate markedly increased lung uptake of [^{64}Cu]NODAGA-CG34 mostly localized to regions of airspace opacities detected by CT. Co-injection of 100-fold molar excess of non-radiolabeled NODAGA-CG34 blocks the tracer uptake in inflamed lungs (bottom row), confirming the specificity of tracer uptake. *In vivo* PET-derived quantification of tracer uptake demonstrates ~73% increase in lung SUV_{max} (**B**) and ~72% increase SUV_{mean} (**C**) in LPS-injured mice compared to control mice (N = 3 males and 4 females per group), which is completely blocked by co-injection of excess non-labeled NODAGA-CG34 despite CT evidence of lung injury (N = 2 males and 2 females in the blocked group). (**D**) Quantification of tracer uptake by γ-counting confirms a similar pattern with 103% increased [^{64}Cu]NODAGA-CG34 uptake in experimental lung injury, compared to control lungs, which is completely blocked by co-injection of unlabeled NODAGA-CG34. (**E**) *In vivo* PET-derived (SUV_{mean}) and *ex vivo* γ-counting-derived (%ID/g) measurements of [^{64}Cu]NODAGA-CG34 uptake correlate significantly (R^2 = 0.53, P = 0.0006), confirming the accuracy of non-invasive quantification of tracer uptake in lungs. (**F**) Biodistribution of [^{64}Cu]NODAGA-CG34, determined by *ex vivo* γ-counting (%ID/g) in select organs, demonstrated systemic inflammation upon LPS-induced lung injury as evidenced by multi-organ increases in [^{64}Cu]NODAGA-CG34 uptake. SUV_{max}, SUV_{mean}, and %ID/g data in panels **B**-**E** represent the average values of the left and right lungs for each mouse. PBS = phosphate-buffered saline; LPS = lipopolysaccharide. Data are expressed as the mean ± SEM. Linear regressions are shown along with 95% confidence intervals. Statistical significance between groups was calculated using a one-sided ANOVA with a post-hoc two-tailed Fisher's exact test. Linear correlations were determined by calculating the Pearson correlation coefficient.

3.4.4 [^{64}Cu]NODAGA-CG34 PET monitors the therapeutic response to dexamethasone

Considering the promise and accuracy of [^{64}Cu]NODAGA-CG34 PET to quantify lung inflammation, we next determined its potential in monitoring the response to anti-inflammatory treatment by dexamethasone. Similar to our prior experiment, lung uptake of [^{64}Cu]NODAGA-CG34 was significantly increased on day 2 post-LPS-induced ALI compared to controls, as

determined by *in vivo* PET and *ex vivo* γ-counting (Figure 13). Dexamethasone treatment (1 and 24 hours post-LPS) significantly reduced lung uptake of [^{64}Cu]NODAGA-CG34 in LPS-injured mice, as measured both globally throughout the lungs (SUV_{mean} and %ID/g) and in the most inflamed regions (SUV_{max}) (Figure 13). Notably, dexamethasone-treated ALI mice, when compared to untreated ALI mice, frequently demonstrated consolidated regions with minimal tracer uptake, highlighting the potential of [^{64}Cu]NODAGA-CG34 PET to quantify the inflammatory burden of consolidated lungs, hence supplementing the structural information obtained by CT (Figure 13). Consistent with PET findings, dexamethasone significantly reduced the expression of inflammatory biomarkers in LPS-injured lungs (Figure 13).

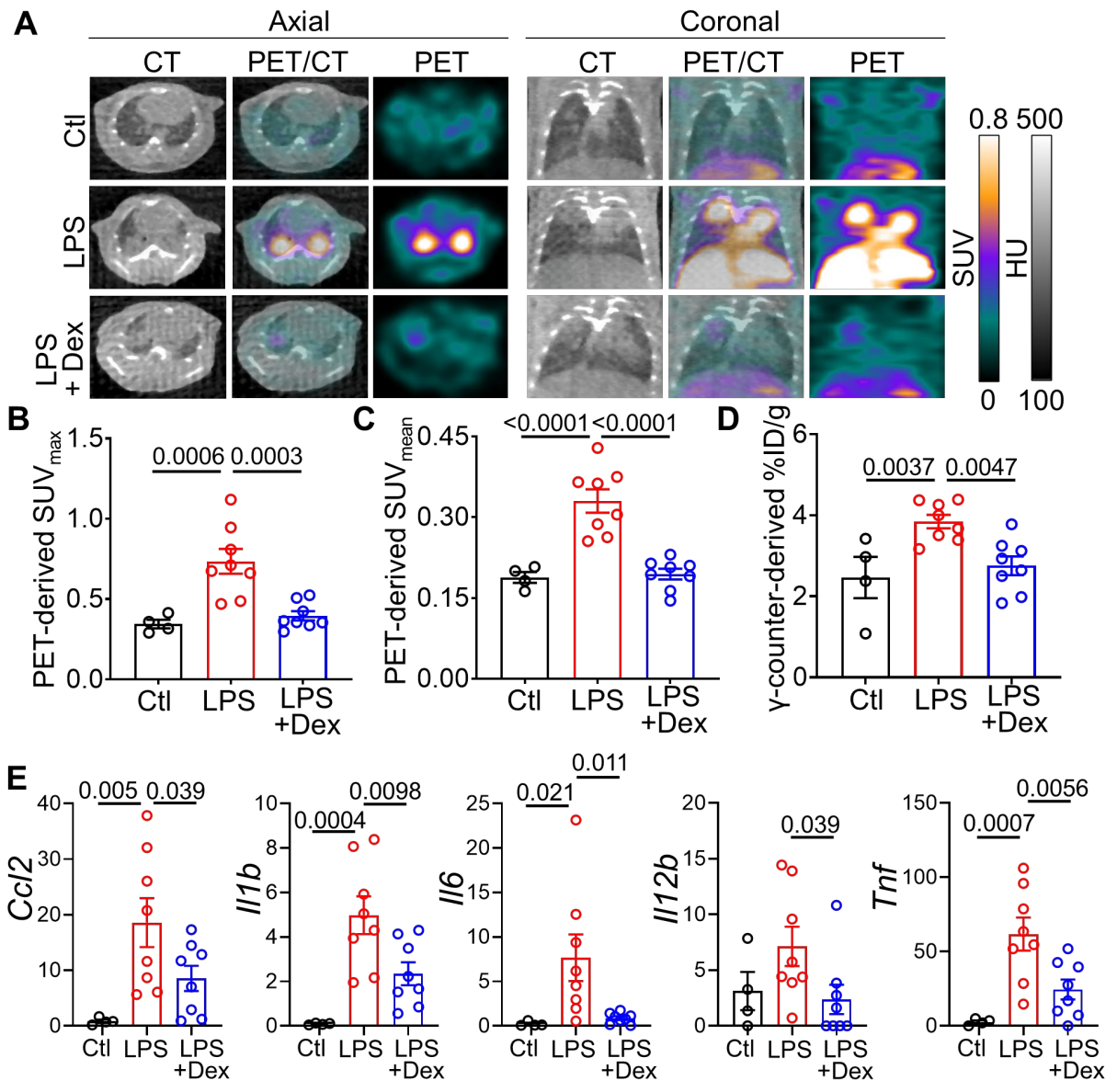

Figure 13. Effect of dexamethasone treatment on the lung uptake of [^{64}Cu]NODAGA-CG34 in LPS-induced experimental lung injury.

(**A**) Representative axial (left) and coronal (right) CT, PET and co-registered PET/CT on day 2 post PBS or LPS treatment. Images were acquired ~90 minutes after intravenous [^{64}Cu]NODAGA-CG34 injection in control (top row) and LPS-treated mice after receiving (bottom row) or not receiving (middle row) dexamethasone. Corticosteroid treatment reduced radiotracer uptake by PET, although areas of airspace opacities were still frequently observed on CT. (**B**-**C**) *In vivo* PET-derived quantification of tracer uptake demonstrates ~46% decrease in lung SUV_{max} and ~41% decrease in SUV_{mean} in LPS-injured mice receiving dexamethasone compared to mice treated with LPS only (N = 4

males and 4 females per group). The lung radiotracer uptake in dexamethasone-treated mice approached that of control mice (N = 2 males and 2 females for control mice). (**D**) Quantification of lung radiotracer uptake by γ-counting confirms a similar pattern with 28% decreased [^{64}Cu]NODAGA-CG34 uptake in LPS-injured mice treated with dexamethasone, when compared to mice receiving only LPS. (**E**) The mRNA expression of select inflammatory markers is significantly reduced in dexamethasone-treated, compared to untreated, LPS-injured lungs. mRNA transcript levels are normalized to the geometric mean of *Rn18s*, the housekeeping gene. SUV_{max} and SUV_{mean}, and %ID/g values represent the average values of the left and right lungs for each mouse. PBS= phosphate-buffered saline; LPS = lipopolysaccharide; Dex= dexamethasone. Data are expressed as the mean ± SEM. Statistical significance between groups was calculated using a one-sided ANOVA with a post-hoc two-tailed Fisher's exact test.

3.4.5 Uptake of CMKLR1-targeting peptide in ALI represents the expansion of CMKLR1-expressing monocytes and macrophages and to a lesser extent natural killer cells

We identified the major immune cells in control and LPS-injured lungs using the gating strategy provided in Appendix Figure 32. For flow cytometric identification of immune cells contributing to [^{64}Cu]NODAGA-CG34 uptake, we utilized a fluorescently-conjugated peptide derived from an established high-affinity CMKLR1 ligand (36) and analog of CG34 derived from the natural amino acids 145-157 of chemerin, 6CF-$Chem_{145-157}$ (Appendix Figure 33). We first determined the high potency and specificity of 6CF-$Chem_{145-157}$ to mCMKLR1 in murine peritoneal macrophages (Appendix Figure 33). Then, we confirmed 6CF-$Chem_{145-157}$ binding may serve as a proxy for [^{64}Cu]NODAGA-CG34 uptake by demonstrating that NODAGA-CG34 displaced 6CF-$Chem_{145-157}$ binding on murine peritoneal macrophages (Appendix Figure 33). Finally, we confirmed that 6CF-$Chem_{145-157}$ binding is restricted to CMKLR1-expressing cells by co-staining of peritoneal cells with 6CF-$Chem_{145-157}$ and an anti-CMKLR1 antibody, which demonstrated 6CF-$Chem_{145-157}$ binding is only detectable in CMKLR1-expressing macrophages

(Appendix Figure 33).

Flow cytometry of mechanically-dissociated lungs demonstrated that two days after LPS-induced injury most leukocyte populations, most pronouncedly neutrophils and monocyte-derived macrophages, followed by natural killer (NK) cells, interstitial macrophages, Ly6C^{hi} monocytes and lymphocytes, were increased (Figure 14). However, the LPS-induced increase in 6CF-Chem$_{145-157}$ uptake at this timepoint was predominantly restricted to monocyte-derived macrophages, followed by modest increases among interstitial macrophages, Ly6C^{hi} monocytes, Ly6C^{lo} monocytes, and alveolar macrophages (Figure 14). NK cells were the only population that demonstrated significant 6CF-Chem$_{145-157}$ uptake both at steady-state and following LPS-induced injury. There was no significant uptake of 6CF-Chem$_{145-157}$ by neutrophils, B-cells, T-cells, and CD45^{neg} cells. Treatment with dexamethasone significantly reduced the number of CMKLR1-expressing cells (e.g., macrophages, monocytes, and NK cells) within the LPS-injured lungs, while only decreasing 6CF-Chem$_{145-157}$ uptake per cell in alveolar macrophages and Ly6C^{hi} monocytes (Figure 14).

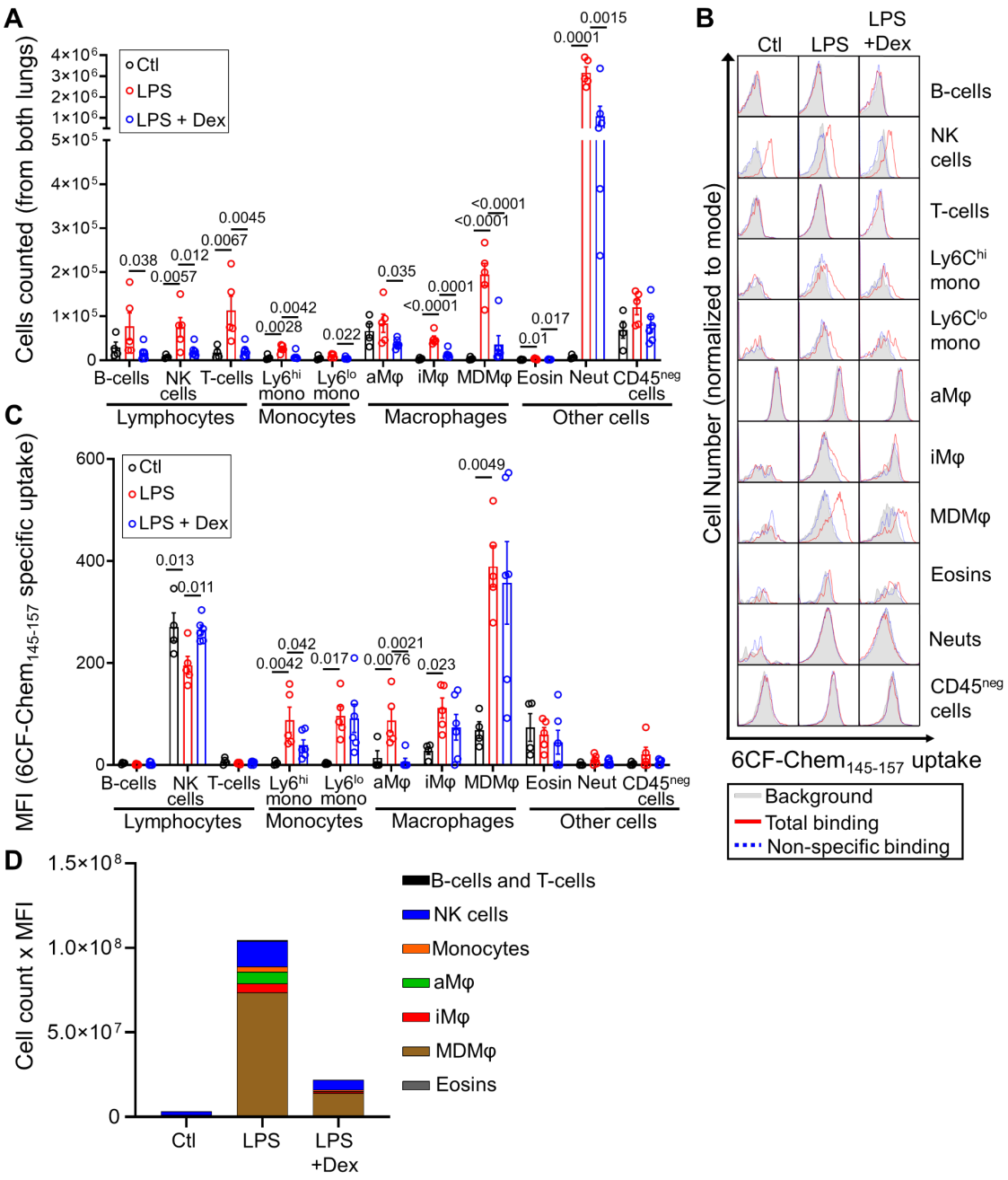

Figure 14. Flow cytometry identification of CMKLR1 expressing cells in healthy and LPS-injured lungs.

(**A**) The absolute number of most immune cells within the lungs is significantly increased at day 2 post-intratracheal instillation of LPS. (**B**) Representative histograms showing specific uptake of a CMKLR1-targeted fluorescent ligand, 6CF-Chem$_{145-157}$ (100 nM), by various immune cells in the lungs of mice treated with PBS, LPS, or LPS plus dexamethasone (gray: background/autofluorescence; red: total-binding of 6CF-Chem$_{145-157}$ in the absence of Chem$_{145-157}$; blue: non-specific binding of 6CF-Chem$_{145-157}$ in the presence of 10 μM Chem$_{145-157}$). (**C**) Specific 6CF-Chem$_{145-}$

$_{157}$ uptake (total minus non-specific/blocked) in different cell subsets was quantified by mean fluorescent intensity (MFI), as a proxy for the uptake of CMKLR1-targeted tracer ([^{64}Cu]NODAGA-CG34), in LPS-injured *vs.* control mice. Monocyte-derived macrophages, interstitial macrophages, and monocytes (Ly6C^{hi} and Ly6C^{lo}) demonstrated the largest increases in 6CF-Chem$_{145-157}$ uptake in LPS-induced experimental lung injury. Natural killer cells had significant 6CF-Chem$_{145-157}$ uptake during steady-state, but the uptake was not further induced by lung injury. (**D**) A stacked-bar graph summary of the cell count multiplied by the cellular uptake (MFI) of 6CF-Chem$_{145-157}$ highlights that monocyte-derived macrophages are the major contributors to the tracer uptake (~70%) due to a marked increase in their abundance and significant induction of 6CF-Chem$_{145-157}$ uptake per cell in mice with LPS-induced ALI compared to control or dexamethasone-treated mice. CD45-negative cells and neutrophils are omitted from this graph due to their negligible specific 6CF-Chem$_{145-157}$ uptake. N for PBS group = 2 male and 2 female mice; N for LPS group: 3 male and 2 female mice; N for LPS + dexamethasone group: 3 male and 3 female mice. aMφ: alveolar macrophages; Eosins: eosinophils; iMφ: interstitial macrophages; MDMφ: monocyte-derived macrophages; NK cells: natural killer cells; Neuts: neutrophils. Data are expressed as the mean ± SEM. Statistical significance between groups was calculated using a one-sided ANOVA with a post-hoc two-tailed Fisher's exact test.

To estimate the contribution of individual CMKLR1 expressing cell types to the total lung uptake of 6CF-Chem$_{145-157}$, as a proxy for the uptake of [^{64}Cu]NODAGA-CG34 in PET imaging studies, we multiplied the number of counted cells per type by their 6CF-Chem$_{145-157}$ uptake measured by specific mean fluorescence intensity. Using this measure, we confirmed that LPS-treated mice had the highest total lung uptake of 6CF-Chem$_{145-157}$, while dexamethasone treatment markedly reduced 6CF-Chem$_{145-157}$ uptake (Figure 14). By contrast, there was minimal 6CF-Chem$_{145-157}$ uptake in PBS-treated mice. Importantly, we determined that monocytes and macrophages represented the majority (~85%) of total 6CF-Chem$_{145-157}$ uptake on day-2 post-LPS-induced ALI which was largely driven by monocyte-derived macrophages (contributing to ~70% of the uptake) with smaller contributions from alveolar macrophages (~7%), interstitial macrophages (~5%), and monocytes (~3%). NK cells represented only ~14% of 6CF-Chem$_{145-157}$

uptake in LPS-injured lungs. A similar pattern of 6CF-Chem$_{145-157}$ uptake by cell type was found in dexamethasone-treated ALI mice though at a significantly reduced total uptake of 6CF-Chem$_{145-157}$. By contrast, 6CF-Chem$_{145-157}$ uptake was markedly lower in PBS-treated mice and was largely driven by NK cells (~60%) and alveolar macrophages (~21%), while monocytes-derived macrophages (~6%), interstitial macrophages (~2%), and monocytes (~1%) contributed minimally to the total uptake.

We used combined high-resolution autoradiography and histology to confirm the spatial colocalization of [^{64}Cu]NODAGA-CG34 uptake to regions of lung inflammation and increased CMKLR1 expression. As demonstrated in Figure 15, autoradiography revealed minimal diffuse [^{64}Cu]NODAGA-CG34 uptake throughout the lungs in control mice. However, a marked increase in [^{64}Cu]NODAGA-CG34 uptake was present in LPS-injured lungs manifesting as discrete foci of tracer accumulation, mostly in a peri-bronchial distribution as expected by the intratracheal delivery route of LPS, superimposed on a diffusely increased tracer uptake in the remaining parts of the lungs. Notably, the foci of high [^{64}Cu]NODAGA-CG34 uptake colocalized with inflamed regions of lungs as determined by hematoxylin and eosin staining (Figure 15) and increased CMKLR1 expression (Figure 15). Further, we confirmed that the abundant expression of CMKLR1 in inflamed regions of LPS-injured lungs mostly co-localized with CD45 (Figure 15) and F4/80 (Figure 15), consistent with flow cytometric finding of 6CF-Chem$_{145-157}$ uptake in macrophages.

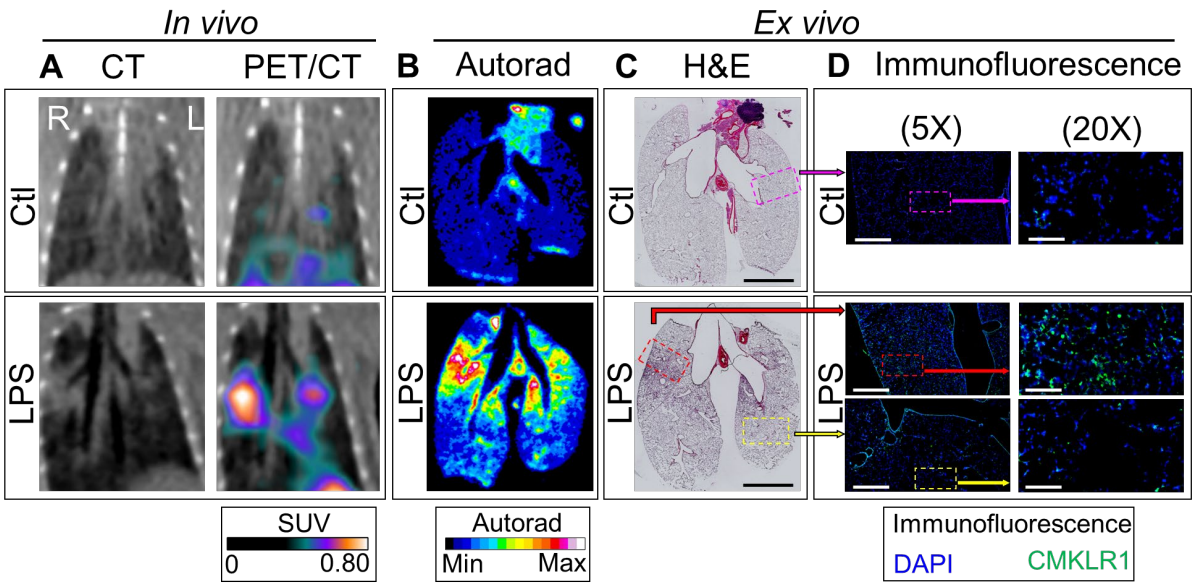

Figure 15. Co-localization of [^{64}Cu]NODAGA-CG34 uptake and CMKLR1 expression via PET/CT, autoradiography and immunohistology in murine lungs.

Representative PET/CT images (**A**) from a control mouse (top) and day-2 post-LPS (bottom) reformatted according to the plane of *ex vivo* autoradiography (**B**) and hematoxylin and eosin-stained tissues (**C**) confirm excellent colocalization of [^{64}Cu]NODAGA-CG34 uptake with inflamed regions of the lungs. Representative low- and high-magnification immunofluorescent staining images (**D**) from adjacent tissue sections demonstrate the abundant expression of CMKLR1 in a highly inflamed region of the lungs in an LPS-treated mouse (red box in **C**) while there is minimal CMKLR1 expression in a less inflamed (yellow box in **C**) or non-inflamed (purple box in **C**) regions of lungs in the LPS- and PBS-treated mice [Scale bar in hematoxylin and eosin imaging = 5 mm, in 5X immunofluorescence images = 800 µm, and in 20X immunofluorescence images = 200 µm. N for PBS and LPS groups = 2 and 3 male mice, respectively]. Increased CMKLR1 expression in LPS-induced lung injury mostly colocalizes with (**E**) CD45^{+} leukocytes, and in particular (**F**) F4/80^{+} macrophages. Scale bar 20X immunofluorescence images = 200 µm, and in 100X immunofluorescence images = 40 µm. N for PBS and LPS groups = 2 female and 1 male mouse per group.

3.4.6 Distinct kinetics of CMKLR1 and CCR2 expression by monocytes and macrophages in ALI allow for monitoring of different aspects of lung inflammation by PET

CCR2-targeted PET using [^{64}Cu]DOTA-ECL1i has been reported to detect the early phase of lung inflammation at 24 hours post-LPS administration in the murine model of ALI (53). Notably, the lung uptake of [^{64}Cu]DOTA-ECL1i returned to the level of control lungs on days 2 and 6 post-LPS (53). To determine the potential of [^{64}Cu]NODAGA-CG34 PET in detecting a distinct aspect of inflammation captured by [^{64}Cu]DOTA-ECL1i PET (i.e., increased burden of recruited monocytes/macrophages *versus* ongoing monocyte flux), we compared the kinetics of CCR2 and CMKLR1 expression at different timepoints after LPS administration by flow cytometry (Figure 16). CCR2 expression was highest among Ly6C^{hi} monocytes while it was markedly lower in interstitial and monocyte-derived macrophages particularly on days 4 and 7 post-LPS, consistent with the rapid downregulation of CCR2 upon monocyte-to-macrophage differentiation (147, 148). In contrast, 6CF-Chem$_{145\text{-}157}$ uptake, as a surrogate for CMKLR1 expression, remained high in monocyte-derived macrophages throughout the first week after LPS administration with only a modest decrease on day 7. A progressive increase in 6CF-Chem$_{145\text{-}157}$ uptake by interstitial macrophage was also noted throughout the 7-day period, while its uptake by Ly6C^{hi} monocytes markedly dropped from day-1 to day-2 post-LPS. Notably, CCR2 and CMKLR1 expression by SiglecF^{hi} alveolar macrophages remained negligible in control mice and throughout the first week after LPS administration. These data support distinct kinetics of CCR2 and CMKLR1 expression with CCR2 primarily expressed by undifferentiated Ly6C^{hi} monocytes while CMKLR1 predominantly expressed upon differentiation of monocytes to macrophages.

To confirm that the persistent expression of CMKLR1 by the accumulated burden of lung macrophages allows for the imaging of lung inflammation over an extended period after the

induction of ALI, we performed a time course analysis of [^{64}Cu]NODAGA-CG34 PET over one week following LPS administration (Figure 16). Interestingly, the lung uptake of [^{64}Cu]NODAGA-CG34 closely paralleled the kinetic changes in CMKLR1 expression by monocytes and macrophages detected by flow cytometry, i.e., a persistent increase in [^{64}Cu]NODAGA-CG34 uptake throughout the first week after LPS administration with a modest decrease on day 7 coinciding with the resolving phase of inflammation as detected by the reduced number of inflammatory cells (Appendix Figure 34). Together, our data suggest that CMKLR1- and CCR2-targeted PET detect distinct aspects of monocyte/macrophage biology in ALI in which the uptake of [^{64}Cu]NODAGA-CG34 is primarily reflective of the accumulated burden of recruited monocyte-derived and interstitial macrophages, while [^{64}Cu]DOTA-ECL1i uptake is largely driven by ongoing flux of monocytes during the early stage of ALI irrespective of the total burden of macrophage accumulation.

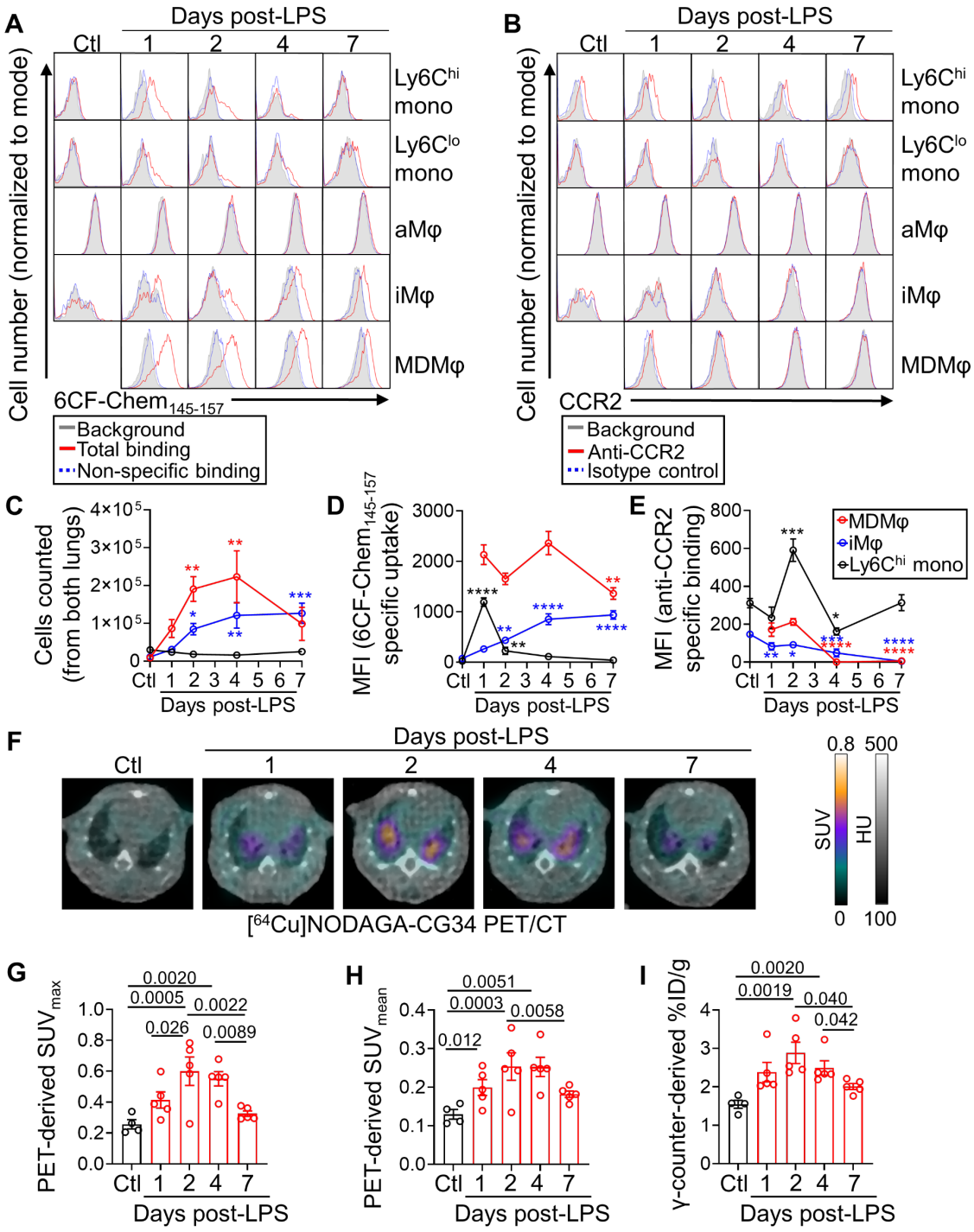

Figure 16. Kinetics of CMKLR1 and CCR2 expression by monocytes and macrophages during LPS-induced ALI and time course of [^{64}Cu]NODAGA-CG34 PET/CT.

(**A-B**) Representative histograms showing the specific uptake of a CMKLR1-targeted fluorescent ligand, 6CF-Chem$_{145\text{-}157}$ (100 nm), or expression of CCR2 in lung monocytes and macrophages throughout the course of LPS-

induced ALI (gray: background/autofluorescence; red: total-binding of 6CF-Chem$_{145-157}$ in the absence of Chem$_{145-157}$ or binding of a CCR2 antibody; blue: non-specific binding of 6CF-Chem$_{145-157}$ in the presence of 10 μM Chem$_{145-157}$ or binding of isotype control antibody). Data for monocyte-derived macrophages is omitted for the control group as the cell number was very low for accurate quantification. (**C**) The absolute number of Ly6C^{hi} monocytes, interstitial macrophages, and monocyte-derived macrophages at different time points following LPS instillation. The number of monocyte-derived macrophages peaks on days 2 and 4, whereas the number of interstitial macrophages increases through day 7. By contrast, the number of Ly6C^{hi} monocytes remains consistently low. (**D**-**E**) Specific 6CF-Chem$_{145-157}$ uptake (total minus non-specific/blocked) or anti-CCR2 binding (anti-CCR2 minus isotype control) in Ly6C^{hi} monocytes, interstitial macrophages, and monocyte-derived macrophages following LPS-induced lung injury. Monocyte-derived macrophages maintain high 6CF-Chem$_{145-157}$ uptake throughout the course of ALI, whereas interstitial macrophages demonstrate increasing 6CF-Chem$_{145-157}$ uptake through day 7. Ly6C^{hi} monocytes show high 6CF-Chem$_{145-157}$ uptake only on day 1. By contrast, CCR2 expression is primarily restricted to Ly6C^{hi} monocytes in ALI with only a transient low level CCR2 expression by monocyte-derived macrophages during days 1 and 2 after LPS administration. (**F**) Representative axial co-registered [^{64}Cu]NODAGA-CG34 PET/CT images of mice at 1, 2, 4, and 7 days following LPS-treatment or non-treated controls. (**G**-**H**) *In vivo* PET-derived quantification of [^{64}Cu]NODAGA-CG34 uptake demonstrates lung SUV$_{max}$ and SUV$_{mean}$ peaking around 2 to 4 days post-LPS followed by a decrease on day 7. (**I**) Quantification of lung radiotracer uptake by γ-counting confirms a similar pattern of tracer uptake to that obtained by *in vivo* PET. SUV$_{max}$ and SUV$_{mean}$, and %ID/g values represent the average values of the left and right lungs for each mouse. Ctl = untreated mice; LPS = lipopolysaccharide; mono = monocytes; aMφ = alveolar macrophages; iMφ = interstitial macrophages; MDMφ = monocyte-derived macrophages. N for panels A-E: 3 male and 2 female mice except for day-2 with N=2 male and 3 female mice; N for panels F-I: 3 male and 2 female mice except for control group with N=2 male and 2 female mice. Data are expressed as the mean ± SEM. For panels C-E, comparisons were made between the various treatment timepoints to the control group for Ly6C^{hi} monocytes and interstitial macrophages or to the 1-day treatment group for monocyte-derived macrophages (as the control group is omitted). *P*-values: * < 0.05; ** < 0.01; *** < 0.001; **** < 0.0001. Statistical significance was calculated using a one-sided ANOVA with a post-hoc two-tailed Fisher's exact test.

3.4.7 *CMKLR1* expression is increased in lung monocytes and macrophages in COVID-19

Our preclinical results support the premise of CMKLR1 as a novel imaging biomarker of monocyte/macrophage-driven inflammation in an experimental model of ALI. To establish the clinical relevance of CMKLR1 as a biomarker of inflammation in ARDS, we performed a secondary analysis of a snRNA-seq dataset (138) to determine the total and cell-specific expression of *CMKLR1* in autopsied lungs of patients with fatal COVID-19-induced ARDS *vs.* pre-pandemic controls who underwent lung resection or biopsy. *CMKLR1* expression was increased nearly threefold on average in COVID-19 compared to control lungs, though there was a significant heterogeneity in *CMKLR1* expression among the individual patients (Figure 17), supporting the presence of different inflammatory endotypes of COVID-19. Consistent with our data in the murine model, *CMKLR1*-expressing cells were markedly more abundant in COVID-19 compared to control lungs and were mostly clustered with monocytes and macrophages (Fig. 7B-C). Detailed analysis across various cell types (Fig. 7D) demonstrated significant increases both in the abundance of *CMKLR1*-expressing monocytes and macrophages, and their expression level of *CMKLR1* in COVID-19 compared to controls.

A focused analysis of alveolar macrophages and monocyte-derived macrophages (the two populations with most abundant *CMKLR1* expression) in COVID-19 lungs demonstrated distinct transcriptional profiles of *CMKLR1*-positive and *CMKLR1*-negative cells, as summarized by heat maps and volcano plots of the most differentially expressed genes (Figure 17). Interestingly, the transcriptional profiles of *CMKLR1*-expressing alveolar macrophages and monocyte-derived ma1crophages closely resembled those of a recently discovered subset of profibrotic *CD163*/*LGMN*-expressing lung macrophages in COVID-19 and idiopathic pulmonary fibrosis

(137), as confirmed by the overexpression of a significant number of genes upregulated in these cells (Figure 17).

To confirm these results, we analyzed an independent publicly available scRNA seq dataset which demonstrated the increased expression of *CMKLR1* in macrophages obtained from three different sites within the respiratory tract (bronchoalveolar lavage fluid, nasopharynx, and airways) of patients with COVID-19 *vs.* control subjects (Appendix Figure 35) (141, 142, 144). Similarly, using another publicly available scRNA-seq dataset (143, 144), we demonstrated increased expression of *CMKLR1* in macrophages obtained from bronchoalveolar fluid of patients with cystic fibrosis. The expression of *CMKLR1* was mostly restricted to two clusters of $FOLR2^{+}$ and $SPP1^{+}$ interstitial macrophages which were expanded in cystic fibrosis patients compared to control subjects (Appendix Figure 36). Finally, we sought to explore CMKLR1 as a macrophage marker in non-pulmonary tissues. Using a fourth independent scRNA-seq dataset (144, 145), we confirmed that *CMKLR1* expression in other tissues, including spleen, thymus, liver, and fat, was largely restricted to macrophages (Appendix Figure 37). These results collectively suggest a broader clinical relevance of CMKLR1 as an imaging biomarker of inflammatory diseases of the lung and other organs.

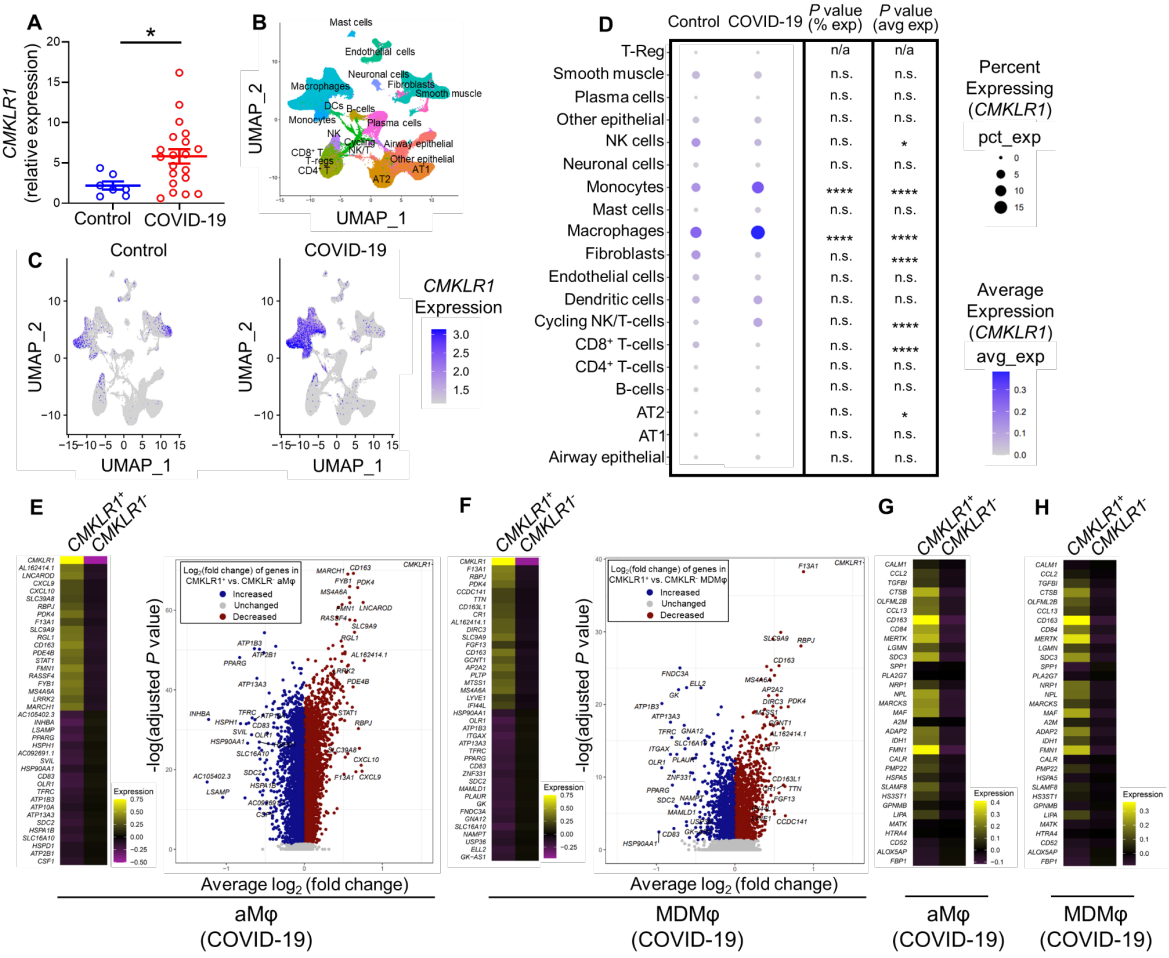

Figure 17. *CMKLR1* expression in the lungs of patients with COVID-19-induced ARDS.

(**A**) Pooled-cell analysis of a previous snRNA-seq dataset demonstrates a significant increase in *CMKLR1* expression in the lungs of patients with COVID-19-induced ARDS as compared to non-COVID-19 controls. (**B**) A UMAP projection of the snRNA-seq data allowing for the identification of major lung cell subsets. (**C**) *CMKLR1* expression clusters predominantly among the monocytes and macrophages subsets, and *CMKLR1* is significantly increased in abundance and expression (log-normalized, per cell) in COVID-19 (right) patients *vs.* controls (left). (**D**) Dot plot representation of the average *CMKLR1* expression and the percentage of *CMKLR1*-expressing cells in selected cell subsets. Monocytes and macrophages demonstrate the highest expression level (avg exp) of *CMKLR1* and frequency (% exp) of cells expressing (avg exp) *CMKLR1* both in control and COVID-19 lungs. Notably, both the frequency of *CMKLR1*-expressing cells and the expression level of *CMKLR1* by monocytes and macrophages are increased in COVID-19 ARDS compared to control lungs. By contrast, *CMKLR1* expression is negligible by other cell types, compared to that of monocytes and macrophages, and is only minimally affected by COVID-19 (**E**-**F**). Heat maps and

volcano plots of the most differentially expressed genes demonstrate distinct transcriptional profiles of *CMKLR1*-positive and *CMKLR1*-negative cells among both alveolar macrophages (E) and monocyte-derived macrophages (**F**) in COVID-19 patients (*CMKLR1* data points are excluded from the volcano plots). (**G**-**H**) Heat map representations support the transcriptional resemblance of *CMKLR1*-expressing alveolar macrophages (**G**) and monocyte-derived macrophages (**H**) with the previously reported profibrotic *CD163*/*LGMN*-expressing profibrotic macrophages in COVID-19 patients. The majority of transcripts reported to be upregulated in *CD163*/*LGMN* profibrotic macrophages are also overexpressed in *CMKLR1*-expressing cells. aMφ: alveolar macrophages; AT1: type 1 alveolar cells; AT2: type 2 alveolar cells; MDMφ: monocyte-derived macrophages; NK: natural killer cells. n.a: not applicable; n.s: not significant. Data are expressed as the mean±SEM. *P*-values: * < 0.05; ** < 0.01; *** < 0.001; **** < 0.0001. Statistical significance between two groups was calculated using a two-sided Student's t-test. The percentage of cells positive for *CMKLR1* and the average *CMKLR1* expression in different cell subsets were compared between COVID-19 and control groups using Fisher's Exact and Wilcoxon rank-sum tests, respectively.

3.5 Discussion

In this study, we demonstrated the accuracy of CMKLR1-targeted PET with [^{64}Cu]NODAGA-CG34 to quantify lung inflammation in a preclinical model of ALI, as validated by strong correlations between radiotracer uptake and expression of biologically relevant inflammatory biomarkers (3), and to monitor the therapeutic response to a clinically relevant anti-inflammatory intervention, i.e., dexamethasone. Additionally, we established the biological basis of [^{64}Cu]NODAGA-CG34 uptake by identifying a marked increase in the abundance of CMKLR1-expressing immune cells in inflamed lungs, which were mostly comprised of monocyte-derived macrophages and to a lesser extent monocytes and interstitial macrophages. Further, we showed that the sustained expression of CMKLR1 on monocyte-derived and interstitial macrophages over the course of LPS-induced ALI represented a distinct pattern than that of CCR2, which was

transiently expressed by undifferentiated monocytes in the early stages of ALI. Finally, we confirmed the clinical relevance of CMKLR1, as a biomarker of lung inflammation and a potential target for molecular imaging, by demonstrating significant increases in the abundance and expression of *CMKLR1* in transcriptionally distinct subsets of lung monocytes and macrophages in patients with COVID-19 as an example of ARDS associated with a major healthcare burden, and in patients with cystic fibrosis.

Disease endotyping is critical for precision medicine-driven management of ARDS (91, 131). In other inflammatory lung diseases, e.g., asthma and chronic obstructive pulmonary disease, identification of clinically measurable endotypes has enabled successful clinical trials and subsequent approval of treatments specifically for patients with certain molecular patterns of inflammation (149, 150). Although ARDS endotypes exist (91, 151), our limited mechanistic understanding of relevant ARDS biomarkers and molecular pathways along with limited non-invasive approaches for assessment of lung inflammation remain major barriers to endotype ARDS and evaluate targeted immunomodulatory therapies in the clinical setting and clinical trials (91, 131).

Molecular imaging is a promising approach for ARDS endotyping through non-invasive characterization of specific patterns of inflammation. The most extensively studied radiotracer, [^{18}F]FDG, detects pulmonary inflammation in both preclinical and clinical settings (47, 85), but poorly predicts disease course or treatment response (47, 76, 152). Considering the non-specificity of [^{18}F]FDG (85), its use is limited as a precision medicine tool in inflammatory lung diseases, and there is a growing interest in developing novel radiotracers for specific inflammatory biomarkers.

Previously tested tracers targeting CCR2 (53), VLA4 (117), CD11b (118), and folate receptor-β (55) have successfully imaged lung inflammation in preclinical models of ALI, though each delineates a selected aspect of the immune response. For example, CCR2 is a promising imaging biomarker for the detection of ongoing influx of classical monocytes to inflamed tissues (53, 56, 153). However, CCR2-targeted PET may not accurately reflect the total burden of tissue macrophages in inflammatory conditions driven by prolonged survival and/or proliferation of tissue macrophages rather than monocyte influx, as CCR2 expression rapidly downregulates upon differentiation of monocytes to macrophages (132, 133). Supporting this scenario, the uptake of a ^{64}Cu-DOTA-ECL1i, a CCR2-targeting tracer, in a murine model of LPS-induced ALI is only detectable in the first 24 hours after induction of ALI and returns to the uptake of uninjured lung by days 2 and 6 post-injury (53), the timeframe which corresponds to the maximal accumulation of monocytes and macrophages in this model. On the other hand, folate receptor-β expression is mostly restricted to lung interstitial macrophages compared to monocytes and alveolar macrophages (154, 155). Unlike CCR2 and folate receptor-β, VLA-4 (156) and CD11b (157) have a broader expression across various leukocyte subsets, hence their targeted imaging likely reflects broader, though less specific, aspects of the inflammatory response. Therefore, the complexity and heterogeneity of the inflammatory processes underlying ALI cannot be captured through a single molecular imaging approach, which necessitates the development of a multi-pronged diagnostic approach to delineate various complementary aspects of lung inflammation, paralleling similar efforts for development of therapeutics affecting different inflammatory pathways.

The chemerin-CMKLR1 axis is emerging as a major contributor to monocyte and macrophage recruitment in multiple preclinical models of lung inflammation. For example, the activation of

the chemerin-CMKLR1 axis in LPS-induced lung injury increased macrophage migration, while decreasing neutrophil influx and pro-inflammatory cytokine production in the lungs (21). Also, functional CMKLR1 signaling provided a survival benefit along with decreased complications in a murine viral pneumonia model (37). Furthermore, CMKLR1 activation improved viral clearance and production of anti-viral antibodies and decreased the expression of pro-inflammatory mediators (21, 37). CMKLR1 may also influence the innate and adaptive immune responses upon environmental exposures and its deficiency markedly reduces leukocyte recruitment to inflamed lungs (38, 39). While clinical data are still lacking, these preclinical findings highlight the potential of CMKLR1 as a novel mechanistically relevant biomarker of lung inflammation in a variety of pulmonary diseases.

We are unaware of prior reports using CMKLR1-targeted imaging in inflammatory diseases. To address this gap, we developed [^{64}Cu]NODAGA-CG34 and demonstrated its favorable pharmacodynamics and pharmacokinetic properties for PET, including high affinity at CMKLR1 and receptor-mediated internalization (146), facile site-specific radiolabeling at high molar activity, low plasma protein binding, excellent plasma stability, and fast blood clearance. Consistent with the prior report of a DOTA-conjugated CG34, the incorporation of unnatural amino acids in the CG34 peptide (31) provided excellent stability against proteolytic degradation compared to natural chemerin-derived peptides. To take advantage of its superior radiometal chelation properties for radiolabeling with [^{64}Cu]Cu^{+2}, lower susceptibility to trans-chelation, and higher *in vivo* stability compared to DOTA (158-160), we used NODAGA as the radiotracer chelating moiety instead of a recently reported DOTA-conjugate (31). NODAGA-based PET tracers, in particular, are readily radiolabeled under mild conditions without the need for post-

synthesis radiochemical purification (3, 158, 161). Further, we selected copper-64 as the radiolabeling isotope due to its advantages over other radiometals, such as gallium-68, including its higher spatial resolution and its longer physical half-life which obviates the need for on-site production (63), allowing for its cost-effective nationwide availability (64).

PET/CT showed spatially heterogeneous [^{64}Cu]NODAGA-CG34 uptake in experimental lung injury with focal regions of intense uptake, corresponding to areas of airspace opacites determined by CT, superimposed on relatively diffusely increased uptake, when compared to control lungs. Therefore, we quantified SUV_{max} and SUV_{mean} to better capture the extent of tracer uptake in the most inflamed regions and the global burden of inflammation, respectively, which both revealed highly reproducible increased tracer uptake in LPS-injured *vs.* control lungs. The lung uptake of [^{64}Cu]NODAGA-CG34, as measured with γ-counting-derived %ID/g, was quantitatively comparable to that of other pulmonary molecular imaging agents (53, 56, 118). Despite the known difficulties of quantification of tracer uptake in the lungs (85), strong correlations between *in vivo* (PET-derived SUV_{mean}) and *ex vivo* (γ-counting-derived %ID/g) measures of [^{64}Cu]NODAGA-CG34 uptake support the accuracy of our approach to non-invasively measure tracer uptake. Encouragingly, *in vivo* radiotracer uptake also correlated with lung expression of multiple pathogenically relevant and therapeutically targetable biomarkers of lung injury (3, 126), such as *Il1b*, *Il6,* and *Tnf*, highlighting the accuracy of CMKLR1-targeted PET to serve as a surrogate non-invasive marker of lung inflammation.

To highlight the translational potential of CMKLR1-targeted PET to non-invasively monitor lung inflammation during treatment, we performed [^{64}Cu]NODAGA-CG34 PET/CT after

dexamethasone treatment in LPS-injured mice, a clinically relevant therapy for ARDS and other inflammatory conditions (126). Dexamethasone treatment significantly reduced lung radiotracer uptake (SUV_{max} and SUV_{mean}) almost to the control levels, paralleling a significant downregulation of several key pro-inflammatory mediators. Interestingly, PET/CT of LPS-injured mice treated with dexamethasone frequently showed focal airspace opacities (i.e. consolidation) by CT with little [^{64}Cu]NODAGA-CG34 uptake compared to mice not treated with dexamethasone. This finding highlights the potential of [^{64}Cu]NODAGA-CG34 PET to provide biological information beyond what can be achieved by traditional radiographic methods such as CT, which are limited to the detection of anatomical/structural changes.

A key biological validation for [^{64}Cu]NODAGA-CG34 PET was establishing the cells contributing to its uptake in LPS-induced lung injury. Little is known about leukocyte subtypes that express CMKLR1 in steady-state and inflamed lungs, although data from other organs, including spleen (21) and blood (45), have shown the expression of CMKLR1 by monocytes/macrophages, NK cells, and dendritic cells. We performed immunophenotyping of lungs cells which bind to 6CF-Chem$_{145-157}$, as a proxy for [^{64}Cu]NODAGA-CG34 uptake and CMKLR1 expression, after establishing its competitive receptor binding profile with NODAGA-CG34 uptake and CMKLR1-specificity. 6CF-Chem$_{145-157}$ uptake was predominantly restricted to macrophages, monocytes, and NK cells, with minimal binding to other immune and non-immune cells. Notably, recruited monocyte-derived macrophages accounted for nearly 70% of the observed 6CF-Chem$_{145-157}$ uptake in the lungs during LPS-induced injury driven by a combination of increased cell count and per cell 6CF-Chem$_{145-157}$ uptake. By contrast, NK cells contributed only 14% to the total lung uptake of 6CF-Chem$_{145-157}$ in LPS-injury. Interestingly, 6CF-Chem$_{145-157}$

flow cytometry data support that dexamethasone-induced decline in [^{64}Cu]NODAGA-CG34 uptake in lung injury is primarily driven by reducing the influx of CMKLR1-expressing leukocytes with smaller contributions of reduced CMKLR1 expression per cell in alveolar macrophages and Ly6C^{hi} monocytes.

To establish the potential of [^{64}Cu]NODAGA-CG34 PET to capture a distinct aspect of monocyte/macrophage-driven inflammation, we compared the kinetic changes in CMKLR1 and CCR2 expression by monocytes and macrophages along with a time course analysis of [^{64}Cu]NODAGA-CG34 uptake over one week after the induction of ALI. We demonstrated that CCR2 is highly expressed by Ly6C^{hi} monocytes, but is downregulated upon monocyte-to-macrophage differentiation, which could explain the previously reported rapid decrease in the lung uptake of [^{64}Cu]DOTA-ECL1i as early as 2 days after LPS-induced ALI (53). In contrast, CMKLR1 expression and [^{64}Cu]NODAGA-CG34 uptake remained high in monocyte-derived and interstitial macrophages during the first 4 days after the induction of ALI and only modestly declined on day 7, which coincides with the resolution phases of inflammation as detected by the decreased number of lung monocytes and macrophages. Collectively, our data support that distinct kinetics of CMKLR1 and CCR2 expression by monocytes and macrophages allows for monitoring different aspects of lung inflammation by [^{64}Cu]NODAGA-CG34 PET (total burden of recruited macrophages) *vs.* [^{64}Cu]DOTA-ECL1i PET (ongoing flux of monocytes).

Despite strong preclinical evidence demonstrating the importance of CMKLR1 to the pathophysiology of inflammation, little is known clinically about its role or utility as a biomarker in ARDS (45). Here, we showed a significant increase in *CMKLR1* expression in COVID-19

ARDS, which consistent with our findings in the mouse model was mostly due to the accumulation of *CMKLR1*-overexpressing macrophages and monocytes. The replacement of homeostatic resident macrophages by monocyte-derived macrophages, which retain their pro-inflammatory phenotype long after the resolution of injury, is a critical pathophysiological process which may drive long-lasting pathogenic remodeling following the resolution of the initial lung injury (162, 163). Therefore, developing tools to monitor the accumulation of hematopoietic-derived lung macrophages may play a major role in ARDS precision medicine by providing insights into its long-term consequences, particularly through molecular imaging of lung macrophage ontogeny via CMKLR1.

Interestingly, a recent snRNA-seq study in an independent dataset has reported that COVID-19 is associated with the expansion of a subset of profibrotic *CD163*/*LGMN*-expressing monocyte-derived macrophages which overexpress *CMKLR1* and transcriptionally resemble a similar subset of profibrotic macrophages expanded in interstitial lung diseases (137). Consistent with this report, *CMKLR1*-expressing monocyte-derived and alveolar macrophages in our dataset shared significant transcriptional similarities with *CD163*/*LGMN*-expressing macrophages, suggesting the potential of our imaging approach to selectively target a population of macrophages previously identified in fibroproliferative ARDS and other fibrotic interstitial lung diseases. We therefore propose that CMKLR1 serves as a promising biomarker for COVID-19 as a clinical example of viral pneumonia-induced ARDS with a major healthcare concern. Given the heterogenous immunologic response and clinical course of patients with COVID-19 or other causes of ARDS, future studies should explore CMKLR1-targed PET for molecular endotyping of lung inflammation.

There are several limitations of this study. First, no experimental model fully recapitulates the pathogenesis of ARDS in humans. However, LPS-induced lung injury is the most extensively validated experimental model of ALI and shares important features with ARDS (164). Moreover, we established the potential clinical relevance of our data using three independent COVID-19 RNA-seq datasets. Second, while our data indicated that CMKLR1 expression in the murine model of ALI is predominantly restricted to monocyte-derived macrophages and interstitial macrophages with negligible CMKLR1 expression by alveolar macrophages, the human datasets demonstrated increased *CMKLR1* expression by the airspace macrophages of patients with COVID-19. Monocyte and macrophage tracing studies in mice have shown that monocyte-derived macrophages acquire a transcriptional phenotype which is almost indistinguishable from that of tissue-resident alveolar macrophages after an extended period of residence in the lungs (162). Moreover, recent work has highlighted that distinct subsets of monocyte-like cells and resident macrophages contribute to diversity of the alveolar macrophage pool in both health as well as disease in human lungs (165-167). Our study cannot discern the ontogeny of the expanded pool of *CMKLR1*-expressing alveolar macrophages in COVID-19. Therefore, it remains to be determined if these cells represent monocyte-derived alveolar macrophages which have acquired a close transcriptional resemblance to tissue-resident alveolar macrophages and/or embryonically-derived alveolar macrophages which are induced to express *CMKLR1* upon lung inflammation. Third, it remains to be determined if CMKLR1 expression plays a mechanistic role in the pathogenesis of lung injury in addition to its role as a biomarker of lung inflammation. However, the primary aim of this study was to validate the utility of CMKLR1 as an imaging biomarker for precision management of ALI by monitoring lung inflammation and response to anti-inflammatory therapy

irrespective of its mechanistical contribution to the pathogenesis of the disease. Finally, the imaging components of this study were only performed in animals, as no FDA approval currently exists for this novel radiotracer. However, the promising results of the current study open the possibility for future New Drug Application (NDA) and conduct of first-in-human PET studies.

In summary, our study demonstrates CMKLR1-targeted PET with [^{64}Cu]NODAGA-CG34 as a promising approach for molecular endotyping of lung inflammation and monitoring the therapeutic response through detection of a distinct subset of monocytes and macrophages. We speculate that [^{64}Cu]NODAGA-CG34 PET may provide similar promising results in the detection of monocyte and macrophage-driven inflammation in other lung diseases and monitoring response to selective immunomodulatory therapeutics. We envision CMKLR1-targeted PET as an emerging precision medicine tool facilitating the endotyping of inflammatory lung diseases. Finally, considering the growing recognition of the pathogenic roles of macrophages in many inflammatory processes (168) and relative specificity of CMKLR1 expression by macrophages, we anticipate that CMKLR1 may emerge as a potential biomarker of inflammation beyond diseases of the respiratory system.

4.0 Chemokine-like receptor 1 targeted positron emission tomography for non-invasive assessment of monocyte-derived macrophages in a preclinical model of pulmonary fibrosis

The work presented in this chapter is being prepared for submission to a peer-reviewed journal and has not been previously published.

This study was supported by the following grants: National Institute of Biomedical Imaging and Bioengineering (NIBIB, R21EB027871) and National Heart, Lung, and Blood Institute (NHLBI, K08HL144911) to Sina Tavakoli; NHLBI (F30HL158038) to Philip Mannes; and NHLBI (R01HL136143, P01HL114453, R01HL142084, and K24HL143285) to Janet Lee. This work utilized the Hillman Cancer Center In Vivo Imaging Facility, a shared resource at the University of Pittsburgh (supported by P30CA047904).

4.1 Abstract

There remains a lack of techniques for molecular endotyping of patients with pulmonary fibrosis. Here, we describe the utility of chemokine-like receptor 1 (CMKLR1) targeted positron emission tomography (PET) to noninvasively detect a monocyte-derived macrophage driven inflammatory phenotype in a murine model of bleomycin-induced lung injury and fibrosis. Lung uptake of our CMKLR1-selective radiotracer, [^{64}Cu]NODAGA-CG34, was significantly increased during the inflammatory phase and the early stages of fibrogenesis. The pattern of radiotracer uptake by PET closely matched the temporal pattern of monocyte-derived macrophage

accumulation in the lungs during bleomycin-lung injury, as measured with flow cytometry. Early CMKLR1-targeted PET following bleomycin treatment predicted the localization and severity of future pulmonary fibrosis. In patients with idiopathic pulmonary fibrosis, analysis of bronchoalveolar lavage samples with RNA-sequencing demonstrates that high pulmonary expression of *CMKLR1* is associated with increased expression of established inflammatory and fibrotic biomarkers. Further, the relative expression of *CMKLR1* prognosticates patient survival, critically during years 1 and 2 following bronchoalveolar lavage. In conclusion, CMKLR1-PET is a promising method for noninvasive monitoring of pulmonary monocyte-derived macrophages associated with pulmonary fibrosis. Additionally, we show CMKLR1 is a clinically relevant biomarker and represents an inflammatory endotype that may find use in stratification of clinical care.

4.2 Introduction

Lung fibrosis is an insidious condition characterized by the replacement of the elastic and compliant lung interstitium by a disorganized and collagen-rich extracellular matrix (ECM) (5, 169) which leads to various impairments in pulmonary function (e.g., restrictive lung physiology, impaired gas exchange, and ventilation/perfusion mismatch) (170). Triggers of pulmonary fibrosis are diverse (5) and include infectious (e.g., COVID-19) or non-infectious acute respiratory distress syndrome (ARDS), radiation, environmental exposures, and a wide range of interstitial lung diseases (ILD) due to known rheumatological and immunological diseases (e.g., scleroderma, sarcoidosis, and hypersensitivity pneumonitis) in addition to a diverse category of idiopathic ILDs. Collectively, pulmonary fibrosis resulting from interstitial lung disease alone represents a

substantial burden of disease with an overall prevalence around >80 cases per 100,000 people (5, 171), which does not account for the large number of patients with pulmonary fibrosis resulting from other causes.

The heterogeneous nature of fibrotic lung diseases, as reflected by the highly variable clinical course and treatment response of patients, is a major challenge to the individualized management of patients (172, 173). While some patients demonstrate a non-progressive disease or a slow physiologic deterioration over the course of years, others experience progressive fibrosis, occasionally interspersed with unpredictable episodes of acute exacerbations, leading to rapid decompensation and/or death in a few months (5, 10). Despite recent advances in the development and FDA approval of medications (e.g. pirfenidone and nintedanib) for both idiopathic and non-idiopathic pulmonary fibrosis which are able to slow the rate of functional decline in certain patients (12, 13, 174-176), the existing clinical, radiographic, physiologic, and laboratory biomarkers are suboptimal in stratifying the risk of progressive disease or predicting and monitoring the response to a specific therapy (7, 10). As such, noninvasive tools to monitor the molecular processes driving adverse ECM remodeling will be vital for a precision medicine approach to fibrotic lung diseases.

Despite the etiological heterogeneity of fibrotic lung diseases, dysregulated immune response is a major driver of adverse ECM remodeling across various diseases, which may be best exemplified by fibrosis caused by pneumonia, ARDS, rheumatological diseases, sarcoidosis, and hypersensitivity pneumonitis (5, 7, 162, 163, 177-180). Even in fibrotic diseases with a less robust inflammatory profiles, e.g., idiopathic pulmonary fibrosis (IPF), a growing body of evidence

supports the role of dysregulated innate and adaptive immune responses, such as high levels of proinflammatory cytokines (e.g., TNF-α and IL-8), in the pathogenesis of lung fibrosis (7, 8, 180-187).

The accumulation of proinflammatory and profibrotic monocyte-derived macrophages which replace or outnumber the homeostatic tissue-resident alveolar macrophages have garnered much attention over the past decade as monocyte-derived macrophages tip the balance towards either normal or pathogenic interstitial remodeling (7, 66, 155, 188). Homeostatic tissue-resident alveolar macrophages are ordinarily the predominant subtype in the lungs and remove pathogenic stimuli without triggering an inflammatory response (189). However, significant numbers of monocyte-derived macrophages are recruited into the lungs during injuries, which play major roles in the development of pulmonary fibrosis including the recruitment and activation fibroblasts (162, 178, 190-193). Further, infiltrating monocyte-derived macrophages persist in the lungs and maintain their acquired transcriptional program from the fibrotic and inflammatory microenvironment following the resolution of lung injury and fibrosis, and these macrophages may pathogenically influence future lung remodeling (162, 194). Therefore, measurement of the in vivo kinetics of monocyte-derived macrophage accumulation in the lungs represents a promising approach to monitor disease activity or treatment response.

A promising technology to non-invasively monitor dynamic changes in lung immune cell populations is positron emission tomography (PET). For instance, C-C chemokine receptor 2 (CCR2) targeted-PET with [^{64}Cu]ECL1i detects the influx of CCR2-expressing monocytes into inflamed lungs in animal models of acute lung injury (53), ischemia-reperfusion injury after lung

transplantation (195), and fibrotic lung injury indued by bleomycin or radiation (56). The feasibility of CCR2-targeted PET has also been recently demonstrated in a first-in-human study in patients with IPF (56). As CCR2 expression is rapidly downregulated upon differentiation of monocytes into macrophages, CCR2-targeted PET is a promising approach to monitor the ongoing flux of monocytes in the lungs (53, 56), while other approaches are needed to detect different kinetic aspects of monocyte-derived macrophages during lung diseases, for example the long-term retention of monocyte-derived macrophages. To address this need, we recently described that targeted imaging of chemokine-like receptor 1 (CMKLR1), a marker expressed by monocyte-derived macrophages, but not by tissue-resident alveolar macrophages, allows for noninvasive monitoring of total burden of lung monocyte-derived macrophages in a mouse model of acute lung injury (22). We also demonstrated the accumulation of distinct $CMKLR1^+$ monocytes and macrophages in the lungs of patients with fatal COVID-19 which transcriptionally resemble a recently described subset of $CD163^+$ and $LGMN^+$ monocytes-derived macrophages with a profibrotic phenotype in patients with COVID-19 (137).

The goal of the present study is to demonstrate the potential of CMKLR1-targeted PET to non-invasively track the accumulation of monocyte-derived macrophages in a murine model of bleomycin-induced fibrotic lung injury and to explore the potential of CMKLR1 expression as a clinically relevant biomarker of ongoing fibrogenesis and for disease prognostication.

4.3 Methods

4.3.1 Chemicals and reagents

The major chemicals and reagents (Table S1), plasmids (Table S2), flow cytometry reagents (Table S3), and histology antibodies (Table S4), are listed in the Supplementary Material.

4.3.2 Cell culture

CHO-K1 cells were grown in complete growth media formulated as Ham's F-12K (Kaighn's) Medium supplemented with 10% fetal bovine serum (FBS) and 1% penicillin/streptomycin. Resident peritoneal cells were harvested from C57BL/6J mice, as previously described (139), via peritoneal lavage with PBS and grown in RPMI Medium supplemented with 10% fetal bovine serum and 1% pencillin/streptomycin.

4.3.3 Transient transfection

CHO-K1 cells at 70-90% confluency were transiently transfected with mouse CMKLR1, mouse GPR1, or mouse CCRL2 plasmids using Lipofectamine 3000 according to manufacturer's instructions.

4.3.4 Stable transfection

CHO-K1 cells at 70-90% confluency were transfected with human CMKLR1 and $G_{\alpha 15}$ plasmids using Lipofectamine 3000 according to the manufacturer's instructions. The transfected cells were next treated with selection antibiotics (e.g., geneticin 400 ug/mL and hygromycin B 800ug/mL) and allowed to grow for about two weeks. Then, individual cell colonies were subcultured and grown until sufficient numbers were available to evaluate the expression of the transfected gene by flow cytometry.

4.3.5 Radiolabeling

NODAGA-CG34 was radiolabeled and characterized as previously reported (22). Radio-HPLC was performed to ensure a radiochemical purity of >95% for [^{64}Cu]NODAGA-CG34 prior to its use in all *in vitro* and *in vivo* experiments.

4.3.6 Mouse model of experimental lung injury

Animal experiments were performed on C57BL/6J mice under a protocol approved by the institutional animal care and use committee. Adult 9- to 12-week-old C57BL/6J mice (Jackson Laboratory, strain #000664) were used throughout the study. Mice were administered intratracheally with 1.5 U/kg bleomycin in 60 µl of phosphate-buffered saline (PBS) to induce lung injury. Control mice were intratracheally injected with 60 µl of PBS. Mice were euthanized

at either 1, 2, or 4 weeks after the induction of lung injury or if the weight loss was >25% of the initial body weight. Studies were performed in accordance with a protocol approved by the University of Pittsburgh Institutional Animal Care and Use Committee.

4.3.7 PET/CT and quantification of [^{64}Cu]NODAGA-CG34 uptake

Two days after intratracheal LPS or PBS instillation, mice were injected intravenously with [^{64}Cu]NODAGA-CG34 (6.76±0.07 MBq). Tracer specificity was addressed by co-injection of [^{64}Cu]NODAGA-CG34 and 100-fold molar excess of non-radiolabeled NODAGA-CG34. Static PET (~10-min) and low-resolution CT (Projections =180; Exposure = 140 msec; Rotation = 180°; Voltage = 80 kV; Current = 500 μA; Field-of-view = 78.5 x 100mm) were performed using a Siemens Inveon PET/CT at 90 minutes after [^{64}Cu]NODAGA-CG34 injection. High-resolution CT scans were similarly performed using a Siemens Inveon machine (Projections = 220; Exposure = 800 msec; Rotation = 220°; Voltage = 60 kV; Current = 500 μA; Field-of-view 30.2 x 31.1 mm).

Regions of interest were drawn over the left and right lungs, and the uptake in the left and right lungs of [^{64}Cu]NODAGA-CG34 was averaged and quantified as the mean and maximal standardized uptake value (%ID/mL$_{mean}$ and %ID/mL$_{max}$) (IRW software). Biodistribution was performed by γ-counting (Wizard2, PerkinElmer) of harvested organs. Data are reported as percentage of injected dose per gram tissue (%ID/g) after decay correction. Multiplanar reformats of PET/CT images were performed (Vivoquant software) to reconstruct planes matching the autoradiography and histology images.

4.3.8 [^{64}Cu]NODAGA-CG34 autoradiography of lungs

Immediately following PET/CT imaging, mice were euthanized, and the lungs were inflated with 1 mL of warmed (37 °C) optimal cutting temperature compound (OCT). Then, the lungs were placed in a block of OCT, quickly frozen, and placed at -20 °C. The following morning cryosections were cut (10 μm) and exposed to high-resolution phosphor screens (GE, BAS-IP SR2025 Super Resolution) overnight at 4 °C. Phosphor screens were scanned at 100-μm resolution using a Sapphire Biomolecular Imager.

4.3.9 Lung immunostaining

Mice treated with bleomycin or PBS were sacrificed and the pulmonary circulation was perfused with ~5 mL of PBS. The lungs were subsequently inflated by intratracheal instillation of 1 mL OCT and quickly frozen. Cryosections were cut (10 μm) and fixed with cold methanol-acetone (1:1). Primary antibodies (1:200 dilution) were applied and incubated at 4 °C overnight. After washing with PBS, fluorescently conjugated secondary antibodies (1:200 dilution) were added and incubated at 4 °C for 2 hours. Slides were mounted with ProLong Gold Antifade Mountant with DAPI and photographed with an Axio Vert microscope (Zeiss).

4.3.10 Binding/uptake of 6CF-CG34 or 6TAM-CG34 by peritoneal macrophages

Peritoneal cells were incubated in indicator-free RPMI in the presence of increasing concentrations of 6CF-CG34 or 6TAM-CG34 with or without co-incubation with unlabeled $Chem_{145-157}$ (2.5 μM). Uptake of 6CF-CG34 or 6TAM-CG34 was allowed to proceed at 37 °C for 1 hour, vortexing samples every ~15 minutes. After a single wash with PBS, flow cytometry was performed using a BD LSR II Flow Cytometer (BD Biosciences) and analyzed by FlowJo software version 10.7.2 (BD Biosciences). The total, non-specific, and specific saturation binding curves were generated using GraphPad Prism 9 Software.

4.3.11 Competitive binding/uptake assay of 6CF-CG34 or 6TAM-CG34 vs. NODAGA-CG34 in peritoneal macrophages

Peritoneal cells were incubated in indicator-free RPMI in the presence of 6CF-CG34 or 6TAM-CG34 (50 nM) with increasing concentrations of NODAGA-CG34 ($1x10^{-10}$ M to $1x10^{-5}$ M). The competitive binding of NODAGA-CG34 and 6CF-CG34 or 6TAM-CG34 was allowed to proceed at 37 °C for 1 hour, vortexing samples every ~15 minutes. After a single wash with PBS, flow cytometry was performed using a BD LSR II Flow Cytometer (BD Biosciences) and analyzed by FlowJo software version 10.7.2 (BD Biosciences). The competitive binding curves were generated using GraphPad Prism 9 Software.

4.3.12 Binding/uptake of fluorescently tagged CG34 peptides by CHO-K1 cells transiently expressing mouse or human CMKLR1, mouse GPR1, or mouse CCRL2

CHO-K1 cells transiently expressing mCMKLR1, hCMKLR1, mGPR1, or mCCRL2 were incubated in indicator-free RPMI in the presence of increasing concentrations of 6CF-CG34 or 6TAM-CG34 with or without co-incubation with unlabeled CG34 (2.5 μM). Uptake of 6CF-CG34 or 6TAM-CG34 was allowed to proceed at 37 °C for 1 hour, vortexing samples every ~15 minutes. After a single wash with PBS, flow cytometry was performed using a BD FACSCalibur or BD LSR II Flow Cytometer (BD Biosciences) and analyzed by FlowJo software version 10.7.2 (BD Biosciences). The total, non-specific, and specific saturation binding curves were generated using GraphPad Prism 9 Software.

4.3.13 Internalization of 6TAM-CG34 by mouse CMKLR1

CHO-K1 cells transiently expressing mCMKLR1 or non-transfected cells grown on glass coverslips coated with fibronectin were incubated in indicator-free RPMI with 6TAM-CG34 (250 nM) with or without co-incubation with CG34 (10 μM) for 1 hour at 37 ºC. The cells were washed with PBS and then treated with Alexa Fluor 647 conjugated wheat germ agglutinin (2 μg/mL) for 20 mins at 4 ºC. Next, the cells were fixed with formalin and the coverslips were mounted onto glass slides with ProLong Gold Antifade Mountant with DAPI and photographed with an Axio Vert microscope (Zeiss).

4.3.14 Flow cytometric immunophenotyping of murine lungs

Mice treated with bleomycin or PBS were euthanized and the pulmonary circulation was perfused with PBS via a right ventricular puncture. Both lungs were then minced with scissors and diluted with 5 mL of ice-cold dissociation buffer (50 mL RPMI, 1 mL FBS, and 100 µg DNase). The lungs were mechanically dissociated using a gentleMACS Dissociator (Miltenyi) using the cycle m_lung 1.02 (1X), followed by m_lung 02.01 (2X). The resulting cell suspensions were filtered using 40-µm cell strainers and red blood cells (RBC) were lysed. After counting the cells, Precision Count Beads (50 µL) were added to each sample. The cells were then divided between tubes and incubated in indicator-free RPMI in the absence or presence of 6CF-CG34 (50 nM) with or without co-incubation with $Chem_{145\text{-}157}$ (10 µM). Uptake of 6CF-CG34 was allowed to proceed at 37 °C for 1 hour, vortexing samples every ~15 minutes. After washing with PBS, cells were blocked using 1% BSA in PBS and treated first with Fc block (2.0 µL per sample), followed by a mixture of antibodies (0.5 µL per antibody per sample) and DAPI (5.0 µL 1 µg/mL per sample) for 0.5 hour at 4 °C. Finally, cells were washed and fixed with 4% formalin for 0.5 hour at room temperature. Flow cytometry was performed the following day using a LSR II Flow Cytometry (BD Biosciences) and analyzed using FlowJo software version 10.7.2 (BD Biosciences). The recovery of dendritic cells (both $CD11b^+$ and $CD11b^-$ subtypes) was low following mechanical dissociation, and they were therefore omitted from the subsequent analysis.

4.3.15 Hydroxyproline assay

At a specified timepoint following PET/CT imaging of mice treated intratracheally with

bleomycin or PBS, mice were euthanized and their lungs were immediately frozen on dry ice and stored at -80 ºC until further use. The lungs were then thawed, and the hydroxyproline content of the lungs (left only) was quantified using a commercially available kit following the manufacturer's protocol (Sigma).

4.3.16 RNA-sequencing analysis

We performed a reanalysis of a previously published RNA-sequencing dataset from bronchoalveolar lavage fluid from patients with idiopathic pulmonary fibrosis or healthy controls (GEO accession: GSE70867) (196). Initially, the data were harmonized using the ComBat package in the R software to reduce inter-study site variability. Patients were subsequently stratified by their *CMKLR1* expression using either the median (e.g., high or low) or tertiles. Similarly, patients were also grouped according to their GAP score (e.g., high or low). Pathway enrichment analysis was performed using the database Kyoto Encyclopedia of Genes and Genomes in R. Prism software was used to generate Kaplan-Meyer and receiver operator curves to determine patient survival using the harmonized *CMKLR1* expression values or comparison of the prognostic value of *CMKLR1* expression *vs.* that of the GAP score at different time points following bronchoalveolar lavage, respectively.

4.3.17 Immunofluorescence staining of paraffin-embedded lung tissues from patients

Patient-derived histology specimens (formalin fixed, embedded in paraffin) were provided by the University of Pittsburgh Biorepository and were cut at a thickness of 5 µm. Tissue sections

were then deparaffinized and rehydrated (xylenes→100% EtOH→95% EtOH→70% EtOH→distilled water). Antigen retrieval was performed by heating tissue sections to ~95 ºC in 10 mM sodium citrate buffer (pH 6.0) for 20 min, followed by an additional 20 min at room temperature. The tissue sections were incubated with the primary antibody (CMKLR1 = 1:2000; CD45 = 1:500) overnight at 4 ºC. After washing with PBS, fluorescently conjugated secondary antibodies were incubated with the tissue sections for 2 hr at 4 ºC. Slides were mounted with ProLong Gold Antifade Mountant with DAPI and photographed with an Axio Vert microscope (Zeiss).

4.4 Results

4.4.1 Monocyte-derived macrophages drive the uptake of CMKLR1-targeting peptide throughout different stages of bleomycin-induced fibrotic lung injury

To determine the kinetics of CMKLR1 expression by different immune cell subset during fibrotic lung injury, we used a fluorochrome-labeled analog of our CMKLR1-targeting radiotracer at 1-, 2-, and 4-weeks post-bleomycin administration, which approximately corresponds to the peak pneumonitis phase, early extracellular matrix remodeling with continued pneumonitis, and the resolution of inflammation with established fibrosis. Employing the gating strategy described in Appendix Figure 38, we identified the major immune cell populations and quantified their abundance at different stages of bleomycin-induced lung injury (Appendix Figure 41). We were particularly interested in characterization of macrophages as our recent work in a preclinical acute lung injury model demonstrated CMKLR1 expression was mostly restricted to monocyte-derived

macrophages (22). In other immune cell populations, including B-cells, natural killer cells, T-cells, eosinophils, and neutrophils, and non-leukocytes (e.g., $CD45^{neg}$), we generally noted a transient increase followed by decrease in the cell count, largely mirroring that of the macrophage populations (Appendix Figure 41).

We defined distinct pulmonary macrophage populations by taking advantage of their differential expression of CD11b, CD11c, and SiglecF, as previously established by lineage tracing studies (162, 178) as alveolar ($CD11b^{lo}/CD11c^{hi}/SiglecF^{hi}$), interstitial ($CD11b^{hi}/CD11c^{lo}/SiglecF^{lo}$), and monocyte-derived ($CD11b^{hi}/CD11c^{hi}/SiglecF^{int}$) macrophages (Figure 18). At baseline, alveolar macrophages were the most abundant population recovered from the lungs with fewer interstitial macrophages and almost no monocyte-derived macrophages. At 1 week following bleomycin, there was a significant accumulation of monocyte-derived macrophages, whereas the number of alveolar macrophages remained stable (Figure 18). Although by 2 weeks the number of monocyte-derived macrophages remained similar to that at 1 week, there was a large increase in the number of alveolar macrophages. Interestingly, the monocyte-derived macrophages at 2 weeks post-bleomycin demonstrated increasing resemblance to tissue-resident alveolar macrophages (i.e., increased SiglecF and decreased CD11b expression), in line with progressive differentiation of monocyte-derived macrophages into alveolar macrophages. By 4 weeks, the number of both monocyte-derived and alveolar macrophages returned to that of baseline. By contrast, the number of lung monocytes ($Ly6C^{hi}$ and $Ly6C^{lo}$) remained relatively stable from week 1 to week 4 after bleomycin-induced injury.

To identify the temporal changes in the abundance and phenotype of the immune cells contributing to the uptake of our CMKLR1-targeting tracer ([^{64}Cu]NODAGA-CG34) derived from

the carboxyl terminus of chemerin, we determined the specific uptake of its fluorescent analog 6CF-CG34)Appendix Figure 39). We confirmed that fluorochrome-modified CG34 maintained similar pharmacodynamic properties to those of NODAGA-CG34. Further we established that CG34-derived peptides are internalized in a CMKLR1-selective manner, with no significant binding/uptake by the two related G-protein-coupled receptors of chemerin, i.e., chemokine (C-C motif) receptor-like 2 (CCRL2) and G protein-coupled receptor 1 (GPR1) (Appendix Figure 40).

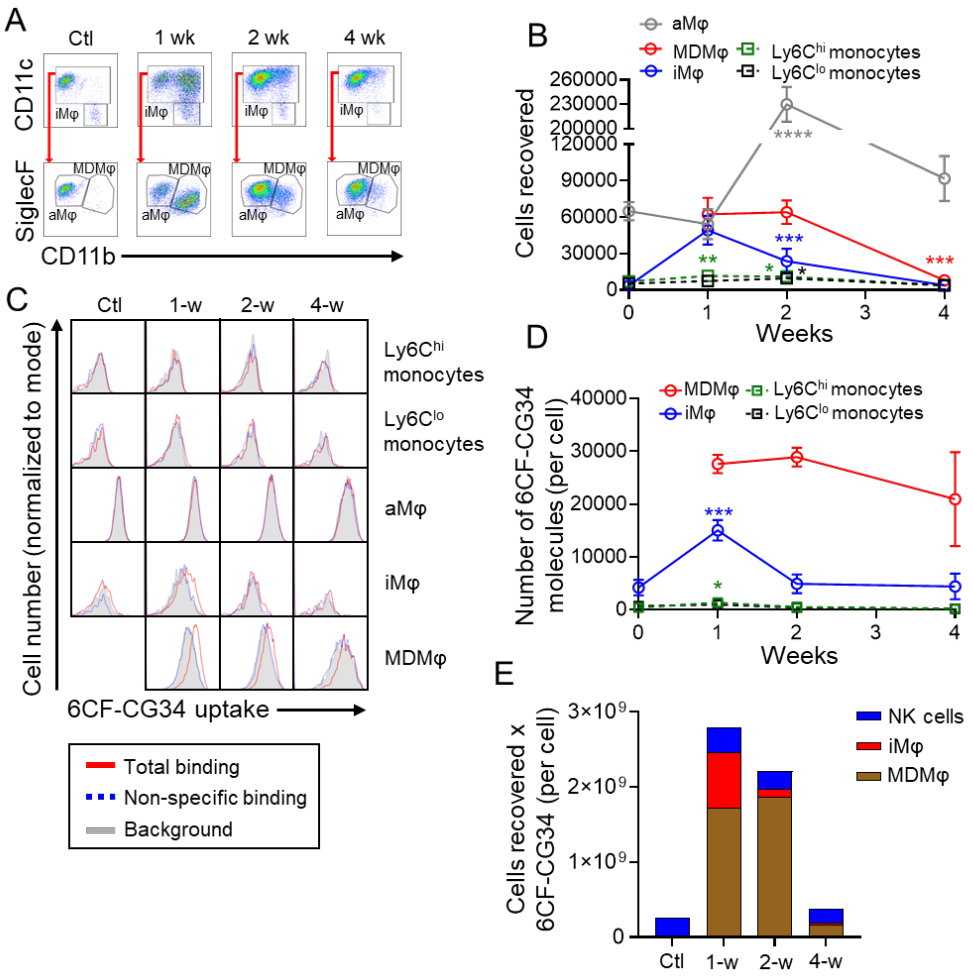

Figure 18. Flow cytometry identification of monocyte-derived macrophages as the primary CMKLR1 expressing cell population during bleomycin-induced lung injury.

(**A**) Different macrophage populations in mechanically dissociated lungs were defined based on their relative expression of CD11b, CD11c, and SiglecF. Following bleomycin administration, the expression of these three markers

in alveolar and interstitial macrophages remained consistent. By contrast, the initial distinct monocyte-derived macrophage population gradually demonstrated a decrease in CD11b and increase in SiglecF expression from 1 through 4 weeks resulting merging of the monocyte-derived and alveolar macrophage populations by 2 weeks. (**B**) The absolute number of recovered monocyte and macrophage populations. (**C**) Representative histograms showing the uptake of CMKLR1-selective fluorescent ligand 6CF-CG34 (50 nM) in various lung macrophage and monocyte populations following treatment with bleomycin or PBS (gray: background/autofluorescence; red: total-binding of 6CF-CG34 in the absence of $Chem_{145-157}$; blue: non-specific binding of 6CF-CG34 in the presence of 10 μM $Chem_{145-157}$). (**D**) Quantification of specific uptake (total minus non-specific uptake) of 6CF-CG34 (MFI was converted to molecules per cell) by selected monocyte and macrophage populations. Monocyte-derived macrophages showed the highest 6CF-CG34 uptake after instillation of intratracheal bleomycin. (**E**) A stacked-bar chart summary of the cell count for CMKLR1 expressing populations multiplied by the cellular uptake of 6CF-CG (molecules per cell) shows monocyte-derived macrophages account for 62% and 84% of the total lung uptake of 6CF-CG34, as a proxy for CMKLR1 expression, at 1- and 2-weeks following bleomycin treatment, respectively. Natural killer cells have N for PBS group = 3 male and 3 female mice; N for 1-w bleomycin group: 3 male and 3 female mice; N for 2-w bleomycin group: 3 male and 3 female; N for 4-w bleomycin group: 3 male and 2 female. aMφ: alveolar macrophages; Eosins: eosinophils; iMφ: interstitial macrophages; MDMφ: monocyte-derived macrophages; NK cells: natural killer cells; Neuts: neutrophils. Data are expressed as the mean ± SEM. Comparisons were made between the various treatment timepoints to the control group for alveolar macrophages, interstitial macrophages, $Ly6C^{hi}$ monocytes, and $Ly6C^{lo}$ monocytes or to 7-d treatment group for monocyte-derived macrophages (as the control group is omitted). *P*-values: * < 0.05; ** < 0.01; *** < 0.001; **** < 0.0001. Statistical significance between groups was calculated using a one-way ANOVA with a post-hoc two-tailed Fisher's exact test.

We found a high uptake of 6CF-CG34 by monocyte-derived macrophages during the first two weeks after bleomycin lung injury which appeared to begin decreasing by the 4^{th} week (Figure 18). Interestingly, interstitial macrophages demonstrated only a transient increase in 6CF-CG34 uptake at 1 week which returned to their baseline level at 2- and 4-weeks post-bleomycin. However, alveolar macrophages and monocytes ($Ly6C^{hi}$ and $Ly6C^{lo}$) did not demonstrate

appreciable uptake of 6CF-CG34 throughout the 4 weeks post-injury. The only other cell type exhibiting 6CF-CG34 uptake was natural killer cells (Appendix Figure 41). Notably, CMKLR1 expression by NK cells did not significantly change after bleomycin-induced injury.

To estimate the relative contribution of individual immune cell populations to the total uptake of the fluorescent CMKLR1-selective ligand, we multiplied the cell count of CMKLR1-expressing cells (e.g., monocyte-derived macrophages, interstitial macrophages, and natural killer cells) by the number of 6CF-CG34 molecules uptaken per cell (Figure 18). At baseline, we found minimal 6CF-CG34 uptake due to minimal numbers of known CMKLR1 expressing cells in the lungs under steady-state conditions. By contrast, the total 6CF-CG34 uptake at 1 and 2 weeks was significantly increased with monocyte-derived macrophages accounting for 62% and 84% of the observed uptake, respectively. This observed increase in 6CF-CG34 uptake was primarily driven by the recruitment of 6CF-CG34 avid (e.g., high CMKLR1 expressing) monocyte-derived macrophages into the lung. The amount of 6CF-CG34 uptake was decreased to approximately that of the baseline by 4 weeks reflecting a reduction in the abundance of CMKLR1-expressing monocyte-derived macrophages. Importantly, natural killer cells minimally contributed to the total 6CF-CG34 uptake by the bleomycin-injured lungs (12% and 11% at 1 and 2 weeks compared to 92% at baseline) due to their markedly lower abundance and lower CMKLR1 expression compared to those of monocyte-derived macrophages.

4.4.2 [^{64}Cu]NODAGA-CG34 PET quantitatively detects lung inflammation during the course of bleomycin-induced injury

Our flow cytometry data showed that monocyte-derived macrophages are the primary contributors to the uptake of our CMKLR1-selective 6CF-CG34 ligand. We next sought to determine the potential of CMKLR1-targeted PET with [^{64}Cu]NODAGA-CG34 to noninvasively monitor the kinetics of monocyte-derived macrophage accumulation during bleomycin-induced lung injury.

Kinetic PET studies in bleomycin-treated versus control mice demonstrated high blood pool activity during the first 30 minutes following radiotracer administration, precluding accurate quantification of [^{64}Cu]NODAGA-CG34 uptake in the lungs at timepoints <30 minutes (Figure 19). There was progressive blood pool clearance of the PET ligand from 30 – 60 minutes, which plateaued from 60 – 90 minutes. Therefore, we conducted static scans and radiotracer quantifications at 90 minutes post-injection.

Consistent with our flow cytometric observation, visual assessment of PET-derived [^{64}Cu]NODAGA-CG34 uptake demonstrated high radiotracer accumulation in the lungs of mice at 1 and 2 weeks following bleomycin, which decreased to nearly that of the control mice by 4 weeks (Figure 19). At early timepoints (e.g., 1 and 2 weeks), we generally observed globally increased radiotracer uptake by PET throughout the lungs despite the presence of discrete regions of airspace opacification on CT. *In vivo* PET-derived quantification of [^{64}Cu]NODAGA-CG34 uptake was consistent with that of our qualitative assessment of radiotracer uptake as we found >100% increases in uptake determined by both global (%ID/mL$_{max}$) and focal (%ID/mL$_{mean}$)

measures 1 and 2 weeks post-bleomycin *vs.* that of controls (Figure 19). Importantly, we confirmed radiotracer specificity in the lungs by blockade of [^{64}Cu]NODAGA-CG34 uptake upon co-injection with excess non-radiolabeled NODAGA-CG34.

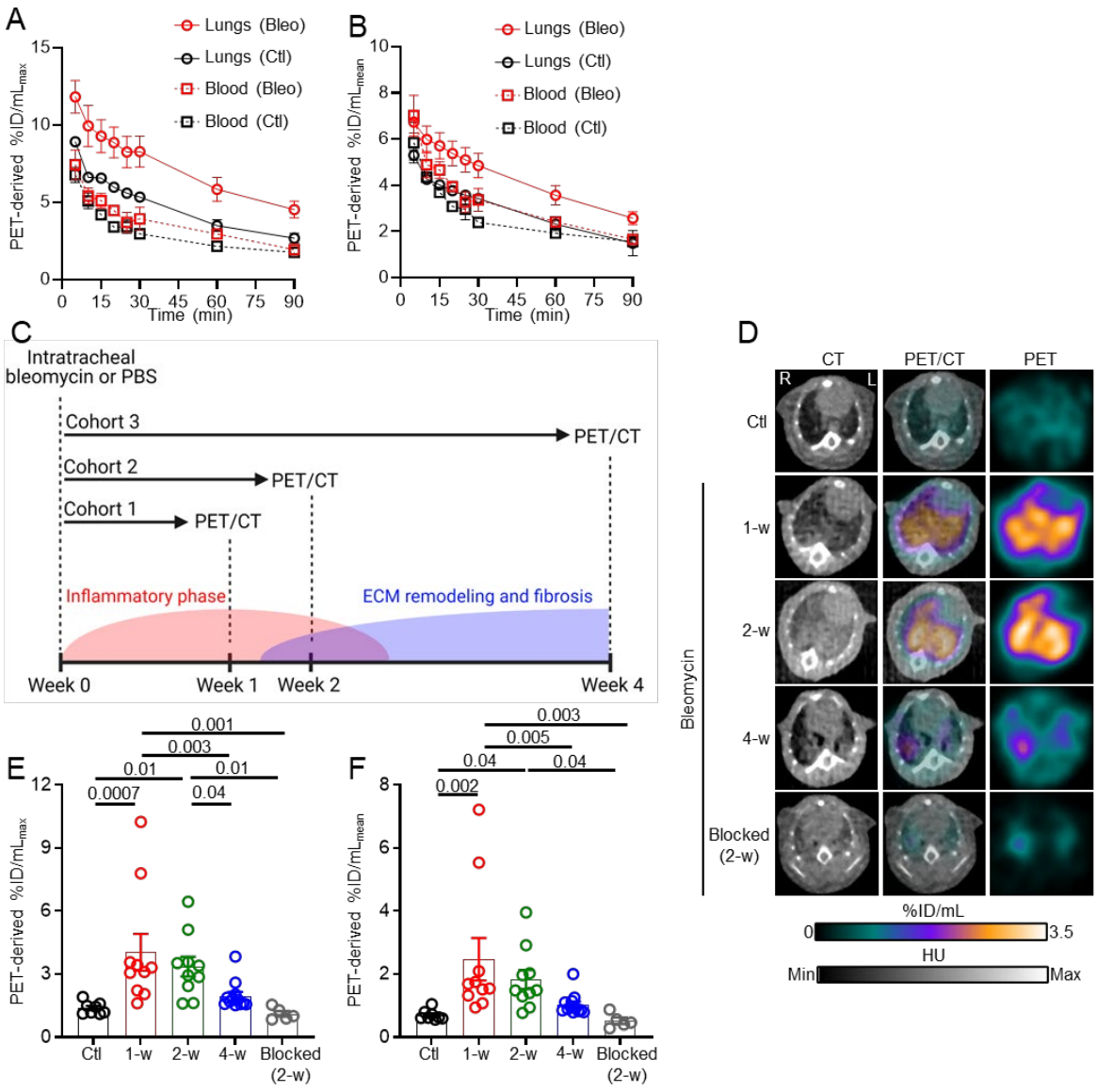

Figure 19. *In vivo* PET imaging of monocyte-derived macrophages with [^{64}Cu]NODAGA-CG34 PET/CT in bleomycin-induced lung injury.

(**A, B**) Kinetic *in vivo* PET-derived [^{64}Cu]NODAGA-CG34 uptake in the lungs and blood over the first 90 minutes following intravenous injection of the radiotracer into bleomycin and control treated mice (1-week after treatment). By 90 minutes, there was high accumulation of [^{64}Cu]NODAGA-CG34 in the lungs of bleomycin vs. control treated

mice, and the radiotracer is mostly cleared from systemic circulation. (**C**) The longitudinal study for quantifying [^{64}Cu]NODAGA-CG34 uptake at distinct stages during bleomycin induced lung injury and remodeling. (**D**) Representative axial CT, PET, and co-registered PET/CT imaging acquired ~90 minutes following intravenous administration of [^{64}Cu]NODAGA-CG34 to control or bleomycin treated mice at 1, 2, or 4 weeks after intratracheal instillation. Diffuse lung uptake of [^{64}Cu]NODAGA-CG34 was observed in the lungs of mice at 1 and 2 weeks after bleomycin treatment, which decreased to baseline by 4 weeks. The specificity of radiotracer uptake was confirmed by blockade of [^{64}Cu]NODAGA-CG34 uptake in the lungs when co-injected with 100x molar excess of non-radiolabeled NODAGA-CG34. (**E, F**) *In vivo* PET-derived quantification of the tracer demonstrates increased lung uptake of 192% and 142%, as well as 254% and 119%, for the %ID/mL$_{max}$ and %ID/mL$_{mean}$ at 1- and 2-weeks following administration of bleomycin vs. that of controls, respecitvely. %ID/mL$_{max}$ and %ID/mL$_{mean}$ data in panels A, B, E, and F represent the average values of the left and right lungs for each mouse. Ctl = control, i.e. phosphate-buffered saline; Bleo = bleomycin. Data are expressed as the mean ± SEM. Linear regressions are shown along with 95% confidence intervals. Statistical significance between groups was calculated using a one-way ANOVA with a post-hoc two-tailed Fisher's exact test. Linear correlations were determined by calculating the Pearson correlation coefficient.

Ex vivo γ-counting-derived radiotracer uptake (as the gold standard method for quantification of tracer accumulation) similarly found a 116% and 45% increase in radiotracer uptake at 1- and 2-weeks post-bleomycin, respectively, that was blocked by co-injection of the unlabeled tracer (Figure 20). To confirm the accuracy of PET quantification of radiotracer uptake, we found a strong correlation between *in vivo* PET- and *ex vivo* γ-counting-derived [^{64}Cu]NODAGA-CG34 uptake in the lungs (R^2 = 0.77; $P < 0.0001$) (Figure 20). Additionally, we observed increased radiotracer accumulation in several non-lung organs, several of which demonstrated specific uptake (Figure 20).

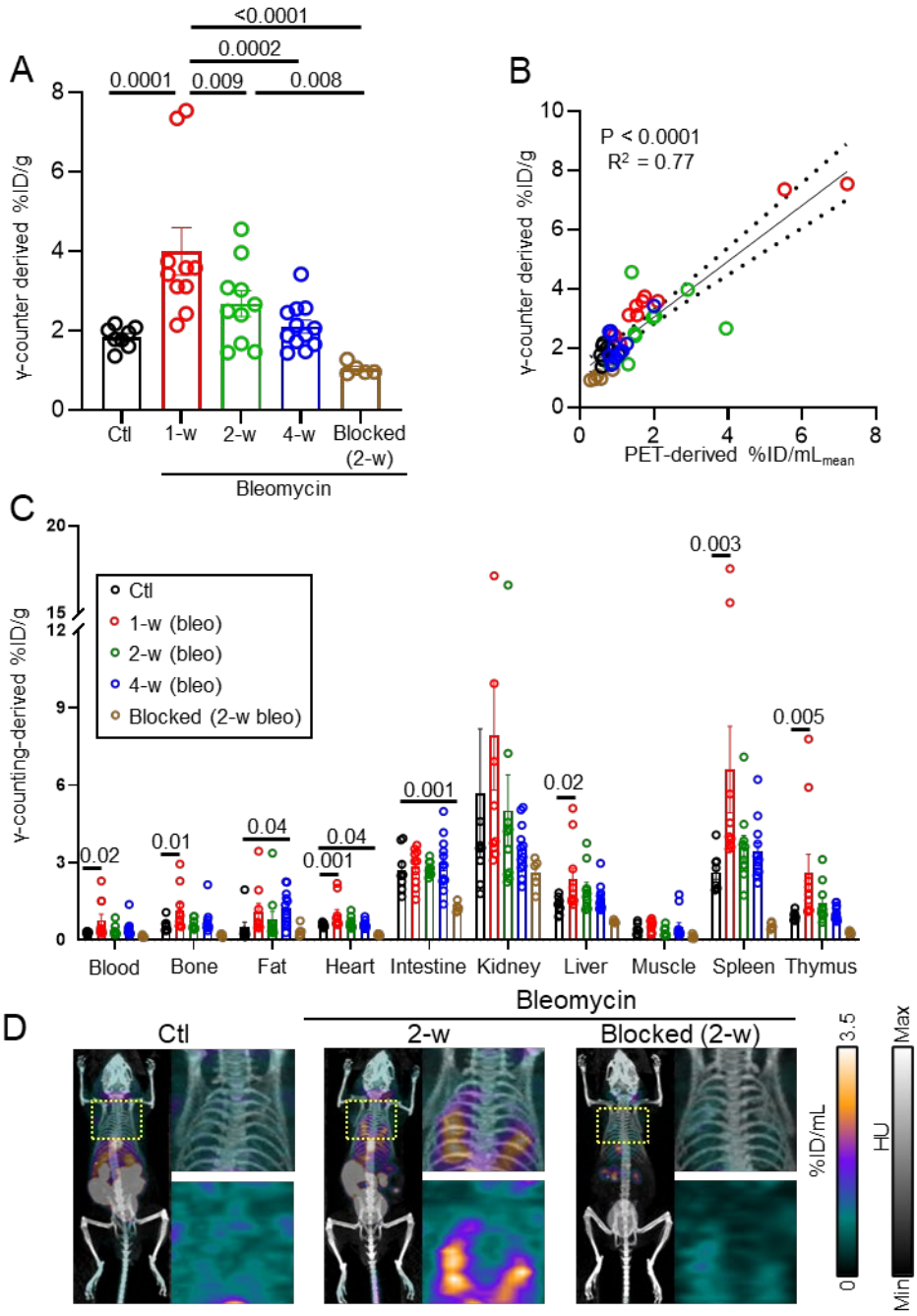

Figure 20. *Ex vivo* measurement of [^{64}Cu]NODAGA-CG34 uptake confirms accuracy and specificity of *in vivo* quantification of PET-derived radiotracer uptake.

(**A**) Radiotracer uptake in the lungs was quantified with *ex vivo* γ-counting (%ID/g), and (**B**) the strong correlation between *in vivo* PET- and *ex vivo* γ-counting-derived quantification of [^{64}Cu]NODAGA-CG34 uptake in the lungs confirms the accuracy of PET. (**C**) γ-counting-derived uptake of [^{64}Cu]NODAGA-CG34 uptake by non-lung organs.

(**D**) Representative full body PET/CT maximal intensity projections to visualize [^{64}Cu]NODAGA-CG34 uptake in mice in both lung and non-lung organs, with magnification (yellow box) of PET/CT and PET maximal intensity projections for the thoracic region. Linear regressions are shown along with 95% confidence intervals. *Ex vivo* uptake of radiotracer in various organs at different time points were compared to that of the control. Statistical significance between groups was calculated using a one-way ANOVA with a post-hoc two-tailed Fisher's exact test. Linear correlations were determined by calculating the Pearson correlation coefficient.

4.4.3 [^{64}Cu]NODAGA-CG34 uptake localizes to inflamed lung regions with increased CMKLR1 expression

To show [^{64}Cu]NODAGA-CG34 uptake is specific to regions of high-CMKLR1 expression, following PET imaging we conducted autoradiography of lung sections and subsequent immunofluorescence for CMKLR1 and a macrophage marker, F4/80 (Figure 21). Similar to what we found with PET, radiotracer uptake was increased in the lungs of bleomycin treated mice. Additionally, the regions of high [^{64}Cu]NODAGA-CG34 uptake were localized to inflamed areas with abundance of CMKLR1-expressing F4/80^{+} macrophages. Together, our data indicated that [^{64}Cu]NODAGA-CG34 PET allows for localization and quantitative monitoring of the accumulation of monocyte-derived macrophages throughout different stages of bleomycin-induced fibrotic lung injury.

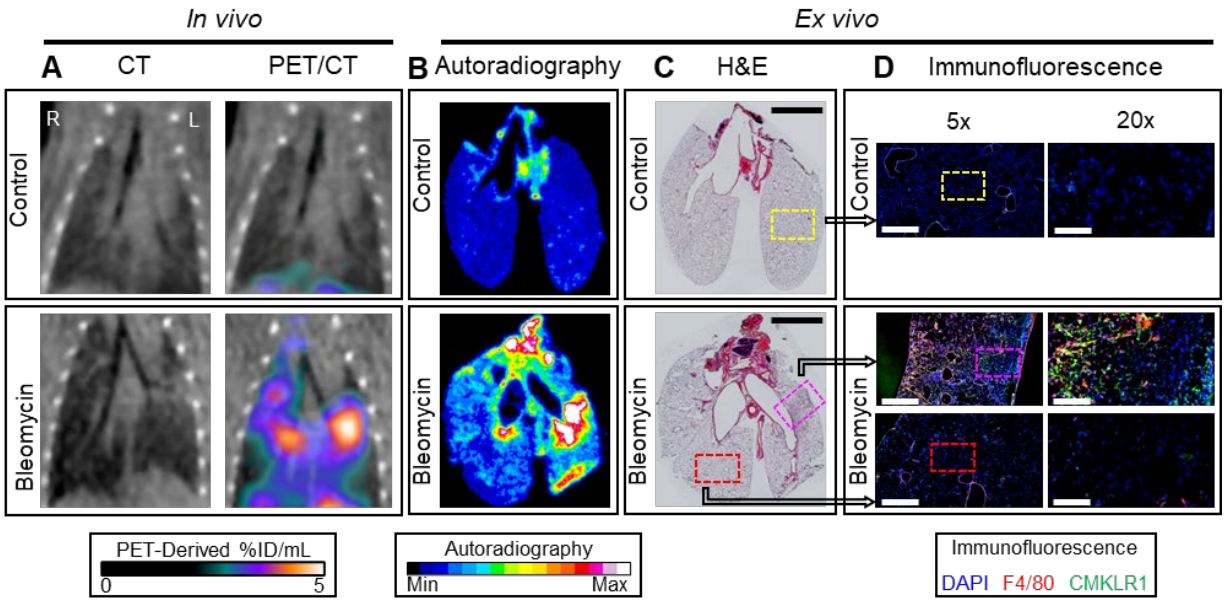

Figure 21. Co-localization of [^{64}Cu]NODAGA-CG34 uptake and CMKLR1 expression via PET/CT, autoradiography and immunohistology in murine lungs.

Representative PET/CT images (**A**) from control and bleomycin treated mice reformatted to the plane of *ex vivo* autoradiography (**B**) and hematoxylin and eosin-stained tissues (**C**) validate selective [^{64}Cu]NODAGA-CG34 uptake by inflamed lung regions. Representative low- and high-magnification immunofluorescent stained images (**D**) from adjacent lung tissues show high CMKLR1 and F4/80 expression and co-localization in inflamed lung regions (bottom pink box) with high [^{64}Cu]NODAGA-CG34 uptake. There was minimal expression of either marker in non-inflamed lung tissue from control (top yellow box) or bleomycin treated mice (bottom red box). [Scale bar in hematoxylin and eosin imaging = 5 mm, in 5X immunofluorescence images = 800 µm, and in 20X immunofluorescence images = 200 µm. N for PBS and bleomycin groups = 2 and 3 male mice, respectively].

4.4.4 [^{64}Cu]NODAGA-CG34 uptake during the early stage of bleomycin-induced injury predicts the severity of future pulmonary fibrosis

To determine the ability of CMKLR1-targeted PET to predict the future development of pulmonary fibrosis, we performed a longitudinal study in which mice underwent PET/CT during the early pneumonitis phase (i.e., 1 week following administration of bleomycin) and were

followed until 4 weeks to determine the extent of fibrosis (Figure 22). As shown by representative images from a control mouse and two mice with low vs. high levels of [^{64}Cu]NODAGA-CG34 uptake (Figure 22), different levels of increased radiotracer uptake were noted in the lungs at 1 week after bleomycin administration, which spatially colocalized with regions and severity of future fibrosis as identified by high-resolution CT performed at 4 weeks. We next quantitatively confirmed these findings by showing early PET-derived radiotracer uptake correlated with the magnitude of lung fibrosis, as measured by hydroxyproline content (Figure 22).

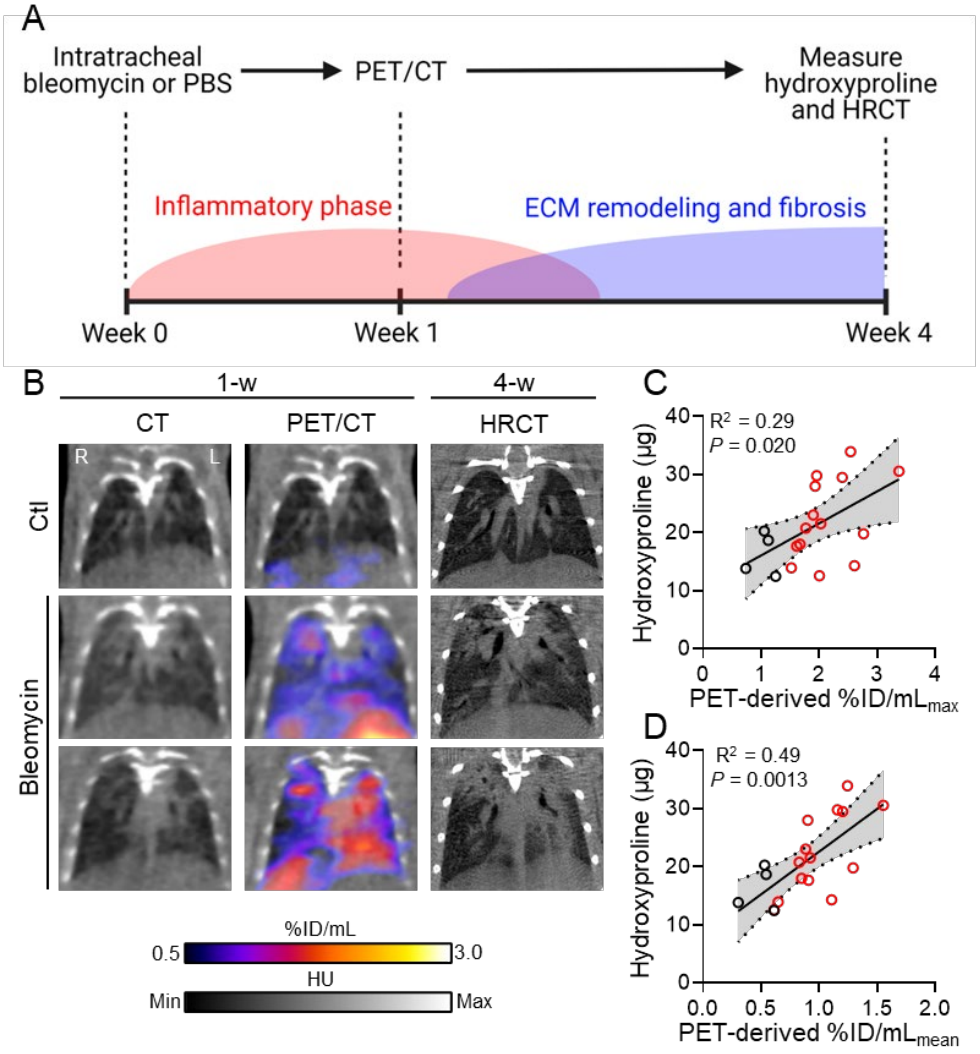

Figure 22. Early CMKLR1-targeted PET predicts the extent of pulmonary fibrosis in a preclinical murine model of lung fibrosis.

(**A**) Experimental design to establish early CMKLR1-PET during the inflammatory phase predicts the development of future fibrosis. (**B**) Representative PET/CT images show lung regions with increased [^{64}Cu]NODAGA-CG34 uptake at 1-week following bleomycin treatment develop more severe fibrosis by 4-weeks as visualized with high-resolution computed tomography (HRCT). (**C**, **D**) The extent of pulmonary fibrosis, measured by the hydroxyproline content in the left lung, at 4-weeks correlates with [^{64}Cu]NODAGA-CG34 uptake in the corresponding lung as measured by (**C**) %ID/mL$_{max}$ or (**D**) %ID/mL$_{mean}$ at 1-week. Linear correlations were determined by calculating the Pearson correlation coefficient.

4.4.5 *CMKLR1* expression by bronchoalveolar lavage cells is associated with an inflammatory phenotype in patients with IPF and is a predictor of mortality

To explore the potential of CMKLR1 to serve as a clinical biomarker for patient stratification and prognostication, we analyzed its expression by bronchoalveolar lavage cells through secondary analysis of a longitudinal cohort of patients with IPF from three sites, Freiburg, Leuven, and Siena (Appendix Figure 42) (196). We first compared *CMKLR1* expression in healthy controls *vs.* patients with IPF according to their Gender-Age-Physiology (GAP) index, a clinically accepted risk stratification model in IPF (197). While *CMKLR1* expression was significantly increased in patients with IPF versus that of healthy volunteers (Figure 23), its expression was not significantly different between different categories of GAP scores. Moreover, there was a marked heterogeneity in *CMKLR1* expression across patients stratified by the GAP index.

To determine if the heterogeneity of *CMKLR1* expression may be used to identify patients with different inflammatory phenotypes, we compared the BAL transcriptome in patients with *CMKLR1* expression above *vs.* below the median value, which revealed many differentially expressed genes (Figure 23). Of note, patients with high *CMKLR1* expression were found to have

a significantly increased expression of many genes with established roles in inflammation, including cytokines (e.g., *IL1R2*, *IL12RB2*) and chemokine (e.g., *CXCL14*, *CCL8*, *CCL2*) signaling, as well as extracellular matrix remodeling (e.g., *LGMN*, *MMP25*, *SSP1*, *COL1A1*, *FGFBP2*), as summarized by the volcano plot (Figure 23). Pathway enrichment analysis of the differentially overexpressed genes further confirmed this finding by demonstrating significant enrichment of several important inflammatory and extracellular matrix remodeling pathways (Figure 23). Together, our results support that a heterogeneous expression of CMKLR1 in patients with IPF may be harnessed for identification of distinct subsets of patients with a higher inflammatory and ECM remodeling profile.

We next assessed the potential of *CMKLR1* expression to serve as biomarker for prediction of future disease progression by comparing the survival of patients in different tertiles of *CMKLR1* expression (Figure 23). Interestingly, patients in the highest tertile of *CMLR1* expression demonstrated a significantly worse outcome median survival of 388 days *vs.* those in the middle (718 days) and lower (1394 days) tertiles. To determine if *CMKLR1* expression provides incremental risk stratification information compared to a clinically established prognostication, we repeated the survival analysis after stratifying patients by their GAP score. Indeed, in patients with both low GAP index (0 to 4, Figure 23) and high GAP index (5 to 8, Figure 23), *CMKLR1* expression was a significant predictive of survival.

Finally, we performed a receiver operating characteristic (ROC) analysis to compare the performance of *CMKLR1* expression by BAL cells *vs.* GAP index to predict the risk of mortality by 1st, 2nd, 3rd, and 4th years following BAL Figure 23. The comparison of the ROC curves

demonstrated that the areas under the curve (AUC) was higher for *CMKLR1* expression than the GAP score during the first two years, whereas the GAP score was higher at later timepoints (e.g., years 3 and 4), suggesting that *CMKLR1* expression, as a biomarker of ongoing inflammation and ECM remodeling, outperforms GAP index for predicting mortality over short to intermediate follow up while GAP index remains a more stable predictor of long-term survival.

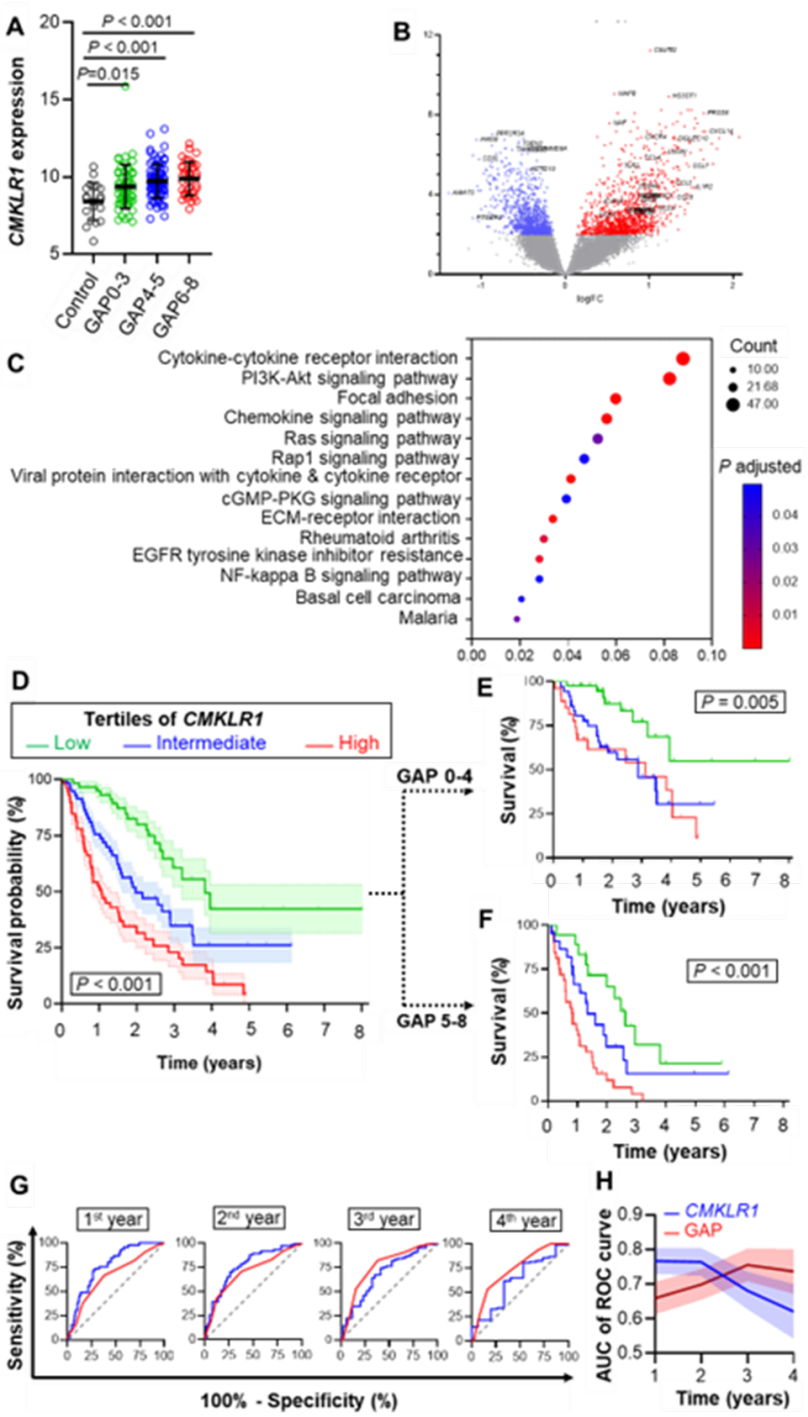

Figure 23. *CMKLR1* expression is associated with an inflammatory gene signature and predicts survival in patients with idiopathic pulmonary fibrosis.

(**A**) Patients were divided into tertiles based on their GAP score and their *CMKLR1* expression was plotted versus that of healthy donors. *CMKLR1* expression is increased in patients with IPF versus that of healthy donors but does not

differ based on the severity of the GAP score. (**B**) A volcano plot for differentially expressed genes in patients with IPF stratified by their CMKLR1 expression (lower 50th percentile = blue, higher 50th percentile = red). Patients with high CMKLR1 expression had significantly increased expression of inflammatory and fibrotic genes. (**C**) Pathway enrichment analysis in patients with high versus low CMKLR1 expression. Patients with high CMKLR1 expression show significant increases in inflammatory and fibrotic pathways. (**D**) Kaplan-Meier survival curves stratified by CMKLR1 expression alone (left) or in conjunction with GAP score (top = low GAP score, bottom = high GAP score). Higher CMKLR1 expression was associated with a worse survival. (**G**, **H**) Receiver operating characteristic curves comparing CMKLR1 expression versus GAP score for predicting patient mortality after the indicated timepoints following bronchoalveolar lavage. The area under the curve (AUC) is higher for CMKLR1 than that of GAP expression during the first two years.

4.5 Discussion

In the present study, we established the promise of CMKLR1-targeted PET as a noninvasive method to assess the lung inflammation-fibrosis axis through detecting the accumulation of MDMφ and predicting the severity of future fibrosis in the murine model of bleomycin-induced fibrotic lung injury. To establish the clinical relevance of our findings, we showed that *CMKLR1* expression is mainly restricted to a subset of *LGMN*- and *MERTK*-expressing macrophages which have been found to be expanded in the lungs of patients with fibrotic ILDs (137) and COVID-19 (22, 138). Finally, we demonstrated that high expression of *CMKLR1* in BAL identifies a subset of IPF patients with increased inflammation and ECM remodeling transcriptomics profile, and it strongly predicts mortality. These results support the potential of CMKLR1-targeted PET as a precision medicine approach in fibrotic lung diseases.

Current therapeutic approaches for fibrotic lung diseases do not consider the molecular

endotypes and the heterogeneity of the pathogenic processes which drive adverse ECM remodeling. As a result, these approaches primarily rely on long-term monitoring of functional and structural consequences of the diseases, for example by PFT and CT, to assess disease progression and response to therapy (14, 175). The inability to identify distinct molecular endotypes of fibrotic lung diseases not only hampers personalized patient management but has also contributed to the string of clinical trials with negative outcomes in fibrotic lung diseases as patient subgroups who are likely to respond to specific treatments cannot be prospectively identified and recruited (198, 199). Encouragingly, molecular endotyping using blood biomarkers (200, 201) or transcriptomics signature of BAL cells (202) has been recently shown to predict IPF progression risk (202, 203) and aids in selectively recruiting patients to clinical trials for pathway-specific therapies (204). However, blood biomarkers are affected by systemic processes and may not be representative of the ongoing pathogenic processes in the lungs. Although BAL-driven endotyping overcomes this limitation, its invasive nature hinders repetitive monitoring of temporal changes in disease endotype caused by the natural progression of the disease or response to therapy (205). Noninvasive imaging offers a solution to address both limitations and has been increasingly explored to monitor molecular processes underlying lung fibrosis (56, 60, 206-208), such as inflammation and adverse ECM remodeling.

We have recently identified CMKLR1 as a promising target for imaging MDMφ in a preclinical model of acute lung injury (22). Furthermore, we observed increased *CMKLR1* expression in transcriptionally distinct subsets of lung monocytes and macrophages in patients with fatal COVID-19 (22). Interestingly, another study in COVID-19 patients found that *CMKLR1* expression is predominantly in profibrotic $LGMN^{+}$ and $CD163^{+}$ MDMφ resembling macrophages

expanded in patients with fibrotic ILDs (137). Based on these findings, we aimed to evaluate the potential of CMKLR1-targeted PET for noninvasive assessment of the lung inflammation-fibrosis axis in a preclinical model and investigate CMKLR1 as a clinical biomarker for prognostication in IPF patients.

[^{64}Cu]NODAGA-CG34 is a peptidomimetic tracer that bears structural resemblance to the carboxyl terminus of the natural ligand of CMKLR1, known as chemerin, but it has been engineered with proteolytic stability through incorporating unnatural amino acids (22, 31). We recently demonstrated several favorable features of [^{64}Cu]NODAGA-CG34 as a molecular imaging probe, including facile radiolabeling with a high yield and molar activity, plasma stability, low plasma protein binding, and rapid clearance (22). Although its affinity (K_d ~ 200 nM) is lower compared to the natural ligand (22), here, we demonstrated that CG34 exhibits internalization similar to natural chemerin-derived peptides (146), which may explain the high accumulation of [^{64}Cu]NODAGA-CG34 in inflamed lungs. Furthermore, we demonstrated that CG34 specific binding is restricted to CMKLR1 with no detectable binding to the other two receptors of chemerin, i.e., CCRL2 and GPR1.

A major limitation of molecular imaging strategies is their tendency to target a single molecule or biological process, whereas accurate identification of specific cell subsets typically requires simultaneous assessment of multiple markers due to the lack of absolute specificity of a single marker for individual cell subsets. As a result, molecular imaging approaches are inherently less specific compared to immunoprofiling of specimens by flow cytometry or scRNA seq. Therefore, we determined the accuracy of CMKLR1 targeting by [^{64}Cu]NODAGA-CG34 in detecting

MDMφ by investigating the uptake of its fluorochrome-conjugated analog (6CF-CG34) by different immune cells at different stages of bleomycin-induced lung injury. Our findings revealed that MDMφ were the primary source of increased 6CF-CG34 uptake during the inflammatory phase of lung injury, contributing to ~62% and ~84% of total uptake at weeks 1 and 2 post-bleomycin, respectively. In contrast, 6CF-CG34 uptake by tissue-resident alveolar macrophages, monocytes, neutrophils, and lymphocytes was negligible. Interstitial macrophages were the only other major contributors to 6CF-CG34 uptake during the pneumonitis phase of lung injury, peaking at week 1 (approximately 26% of total uptake) and declining by week 2 (approximately 5%). It is worth noting that the interstitial stage is an obligatory step preceding the differentiation of monocytes into alveolar macrophages (209); therefore, it may be speculated that the observed transient increase in the uptake of TMRA-CG34 by interstitial macrophages reflects CMKLR1 expression during this intermediary differentiation stage of MDMφ. However, alternative explanations, such as the induction of CMKLR1 by tissue-resident interstitial macrophages, need to be explored through fate mapping studies. As previously reported (22), CMKLR1-expressing natural killer cells were the main contributors to 6CF-CG34 uptake in non-inflamed lungs, although their contribution to total 6CF-CG34 uptake during lung injury was overshadowed by that of MDMφ. Overall, our data support the potential of CMKLR1 as a favorable target for identifying MDMφ in inflamed lungs which can be effectively targeted by CG34-derived imaging probes.

PET-driven quantification of [^{64}Cu]NODAGA-CG34 at various timepoints after bleomycin administration revealed a temporal uptake pattern that closely mirrored the accumulation of CMKLR1-expressing lung MDMφ observed in our flow cytometric analysis. Specifically, we

observed increased [^{64}Cu]NODAGA-CG34 uptake at 1 and 2 weeks after bleomycin treatment which then returned to near-baseline levels by week 4. Despite challenges posed by respiratory motion (210), we demonstrated the accurate noninvasive quantification of lung uptake of [^{64}Cu]NODAGA-CG34, as evidenced by the strong correlation between PET- and γ-counting-derived measures of uptake. Importantly, we validated the prognostic value of CMKRL1-targeted PET by showing that [^{64}Cu]NODAGA-CG34 uptake during the early stage of bleomycin-induced injury predicts the extent and spatial distribution of future pulmonary fibrosis. These findings highlight the potential of CMKLR1-targeted PET as a promising precision medicine tool for monitoring the lung inflammation-fibrosis axis through the detection of MDMφ accumulation during the inflammatory phase of lung injury.

A comprehensive diagnostic approach that encompasses multiple aspects of the lung inflammation-fibrosis axis may facilitate pathway-specific therapeutic strategies for fibrotic lung diseases. Various molecular imaging approaches have been investigated for this purpose. For instance, the ongoing flux of monocytes to inflamed lungs has been successfully visualized using a CCR2-targeted tracer ([^{64}Cu]ECL1i) in preclinical models of lung inflammation and fibrosis (53, 56) as well in a first-in-human trial in patients with IPF (56). However, the downregulation of CCR2 upon differentiation of monocytes to macrophages (148) may limit the utility of [^{64}Cu]ECL1i for capturing the total burden of MDMφ (22), which can be detected by CMKLR1-targeted PET. Folate receptor-β, predominantly expressed by macrophages, represents another potential target for molecular imaging of macrophages and has been utilized in murine models of lung inflammation (55) and fibrosis (57). However, the specific immunophenotype of folate receptor-β-expressing macrophages in the lungs and their biological significance in fibrotic lung

diseases require further exploration. Additionally, tracers targeting receptors that are expressed by a broader range of leukocytes, such as [^{68}Ga]pentixafor (206) and [^{64}Cu]LLP2A (117), targeting CXCR4 and VLA-4, respectively, have shown promise in imaging lung inflammation. Furthermore, there is ongoing research on a separate class of imaging agents that target proteins involved in adverse ECM remodeling, rather than the inflammatory arm of the inflammation-fibrosis axis, such as fibroblast activation (211), collagen crosslinking (61), and tissue collagen content (58). By employing a multi-pronged complementary imaging approach, a more comprehensive understanding of the lung inflammation-fibrosis axis can be achieved, enabling the development of more targeted and effective therapeutic interventions.

For patients with pulmonary fibrosis, a current challenge remains identification of patients who display rapidly progressive disease or are at increased risk for acute exacerbations or death (212). Our secondary data analysis of IPF BAL transcriptomics revealed a heterogeneous expression of *CMKLR1* which allows distinction of a subset of patients with enrichment of inflammatory and ECM remodeling pathways who are at risk of more progressive disease. Additionally, measurement of pulmonary *CMKLR1* expression provides an incremental prognostication benefit over the GAP score, particularly over the short to intermediate term, which is a critical window for selecting patients at high risk of immediate adverse outcomes for prioritization of lung transplant recipients and more intensive care (212, 213). Furthermore, we speculate that identification and monitoring of patient inflammatory profiles may improve clinical trials. Many large clinical trials for pulmonary fibrosis have failed (198), possibly due to the heterogeneity of underlying patient pathophysiology combined with small sample sizes (173). Establishing inflammatory endotypes as inclusion criteria for clinical trials may assist in appropriately selecting

patients and allow for monitoring therapeutic response using molecular, rather than physiologic, endpoints (14). Additionally, clinical trials may benefit from measurement of lung specific inflammatory processes. While peripheral measures of inflammation may be more convenient and safer for serial sampling, a large post-hoc analysis found that measurement of blood inflammatory biomarkers was inferior to the GAP score for prediction of predicted patient outcomes (214). This result stands in contrast to our findings resulting from direct measurement of pulmonary *CMKLR1* expression.

This study has several limitations. First, there are relatively few preclinical models of pulmonary fibrosis and none entirely replicates the pathological complexities of the diverse diseases which lead to lung fibrosis in humans (215). Nevertheless, the bleomycin-induced lung fibrosis model is widely validated and recapitulates key pathogenic aspects of fibrosis, such as the release of similar cytokines and growth factors and activation of relevant signaling pathways which are observed in clinical disease (162, 216, 217). Additionally, we confirmed the relevance of CMKLR1 as a clinical biomarker of MDMφ accumulation in inflamed and fibrotic lungs in patients with COVID-19 (22) and fibrotic ILDs in multiple scRNA seq datasets. Another limitation of our study is that our analysis of the prognostic role of *CMKLR1* expression in BAL cells was restricted to patients with IPF (196). While pulmonary fibrosis can have various other underlying etiologies, we focused on IPF as it represents the prototypical and most common fibrotic ILD. Additionally, we are not aware of other publicly available BAL transcriptomics dataset with longitudinal follow up in other diseases, which limits our ability to explore the potential of CMKLR1 in predicting outcome in other diseases. Another limitation of this study is that BAL sampling underestimates the extent of CMKLR1 expression which can be detected by PET as

interstitial CMKLR1^{+} macrophages (22) are not efficiently recovered by BAL. To address this issue, we performed an exploratory study to determine CMKLR1 expression in lung tissues from patients with different causes of pulmonary fibrosis, including IPF, scleroderma, rheumatoid arthritis, sarcoidosis, and occupational lung diseases (Appendix Figure 43). Our findings demonstrated that CMKLR1 is widely expressed in the lungs of patients across all these etiologies, albeit at different levels, suggesting that CMKLR1 may serve as a biomarker in non-IPF pulmonary fibrotic diseases as well. Finally, due to the lack of FDA approval for this novel tracer, we were unable to perform PET studies in patients. However, the promising results of [^{64}Cu]NODAGA-CG34 in two independent preclinical models of lung diseases and the clinical relevance of CMKLR1 as a biomarker of MDM in patients with COVID-19 (22) and IPF will provide a strong foundation for future application of an Investigational New Drug (IND) for the first-in-human use of this tracer in fibrotic lung diseases.

In conclusion, assessment of monocyte-derived macrophage accumulation in the lungs with CMKLR1-PET is a promising method for molecular endotyping of ongoing inflammation associated with the development of pulmonary fibrosis. We highlight the translational relevance of CMKLR1 in clinical disease and demonstrate the clinical value of identifying patients demonstrating an inflammatory phenotype. Given the pathogenic role of monocyte-derived macrophages across organ systems (168, 218), we anticipate CMKLR1-PET may find uses in additional pulmonary and non-pulmonary diseases.

5.0 Future directions and potential relevance to human disease

We demonstrate that CMKLR1 is a promising biomarker for non-invasive PET imaging of monocyte-derived macrophages in preclinical models of acute lung injury and pulmonary fibrosis (22). To highlight the translational potential of CMKLR1, we show that the pattern of CMKLR1 expression in clinical disease (e.g., COVID-19 and pulmonary fibrosis resulting from various etiologies) closely resembles that of our preclinical models. While these studies have provided contributions to our understanding of CMKLR1 biology, we envision many future studies resulting from our findings.

To our knowledge, there have been no prior clinical investigations of CMKLR1-PET. We believe our results collectively form the rationale for further preclinical development of CMKLR1 with the ultimate goal of filing an Investigational New Drug (IND) Application with the U.S. Food & Drug Administration (FDA) to conduct first-in-human studies. Prior to filing an IND application, there are many remaining preclinical validations focused on pharmacokinetics and toxicology, as well as manufacturing information (e.g., good manufacturing process for radiopharmaceuticals) (219). Should CMKLR1-PET be advanced into clinical trials, the initial studies may focus on imaging healthy volunteers with the eventual aim of enrolling patients with acute lung injury or pulmonary fibrosis to prognosticate outcomes, enable molecular endotyping, and monitor therapeutic response.

While we establish CMKLR1 as a biomarker of lung inflammation in both preclinical models and clinical disease, an outstanding question concerns whether CMKLR1 is mechanistically

relevant to inflammatory processes. Our studies were not designed to provide mechanistical data, and many of the conclusions in the original reports regarding the function of CMKLR1 in the lungs were overly simplistic (21, 37-39). To investigate CMKLR1 as a biomarker and function during inflammation, future experiments may examine the function of CMKLR1 through use of CMKLR1-knockout mice or pharmacologic modulation of the CMKLR1-chemerin axis. Additionally, we have noticed expression of CMKRL1, by single-cell RNA-sequencing, on non-monocyte-derived macrophage lung populations, such as fibroblasts and endothelial cells, which we believe warrant more investigation. Studies in the future might incorporate altered flow cytometry panels for the detection of individual subpopulations of non-leukocytes and compare the function of CMKLR1 across cell lineages. For these *in vitro* and *ex vivo* studies, there remains the need for a fully validated anti-CMKLR1 antibody, particularly for flow cytometry. Although our studies have thus far primarily focused on pulmonary inflammation, we are aware of early reports implicating CMKLR1 in the pathobiology non-lung diseases (220-222). We have started branching out from exclusively studying CMKLR1 in the lungs, and our preliminary findings from RNA-sequencing and preclinical studies suggest several exciting new directions for CMKLR1 biology.

Should CMKLR1 prove mechanistically relevant for pulmonary inflammation, there will likely be desire to continue development of CMKLR1-targeted therapeutics. There have been several prior reports of potent CMKLR1 agonists and antagonists (32, 36, 223-226), however we are unaware of any compounds reaching clinical trials. In the age of targeted immunotherapies, our PET imaging methods may also assist in evaluating CMKLR1-selective therapeutics, especially during the *in vivo* and clinical testing stages. During preclinical studies, CMKLR1-PET

may allow for serial non-invasive monitoring of the CMKLR1-chemerin axis to enhance mechanistical insights gained from *in vitro* and *ex vivo* studies. In clinical trials, CMKLR1-PET may enable molecular endotyping of patients to appropriately select and monitor patients' treatment response.

Another area of interest is the development of newer generations of CMKLR1-targeted PET agents to alter specific pharmacologic properties. To our knowledge, a limited number of PET tracers, including [^{68}Ga]DOTA-CG34 (31) and [^{64}Cu]NODAGA-CG34 (22), have been previously disclosed, differing only by the radiometal and chelator. Thus, the medical chemistry of CMKLR1-PET remains relatively unexplored, and many opportunities exist for optimization of the current radiotracers. For example, future tracers may address the high [^{64}Cu]NODAGA-CG34 uptake by the liver and other gastrointestinal organs, to improve tracer quantification in liver-adjacent thoracic organs (e.g., inferior lung lobes and heart apex and inferior wall) and permit abdominal CMKLR1-PET. Also, there is a need to evaluate different targeting peptides for the radiotracer backbone. While our current targeting peptide, CG34, has been promising, structural modification incorporating elements from other known CMKLR1 agonists may improve imaging performance (e.g., target-to-background ratio) and pharmacologic properties (e.g., binding affinity, elimination half-life). Further, newer radiotracers may compare the use of different PET isotopes to that of Cu-64 for CMKLR1-PET, such as gallium-68 and fluorine-18. However, inherent to the process of medicinal chemistry is a significant degree of trial and error.

In conclusion, our results should inspire additional investigations into the biology of CMKLR1 for which there are many unanswered questions. Hopefully, a better understanding of the biologic

role of CMKLR1 will enable future studies into its use for medical imaging, patient prognostication, and therapeutic purposes with the ultimate goal of improving human health.

Appendix A Supplemental information for "2-deoxy-2-[^{18}F]fluoro-D-glucose positron emission tomography to monitor lung inflammation and therapeutic response to dexamethasone in a murine model of acute lung injury"

Appendix A.1 Supplemental Figures

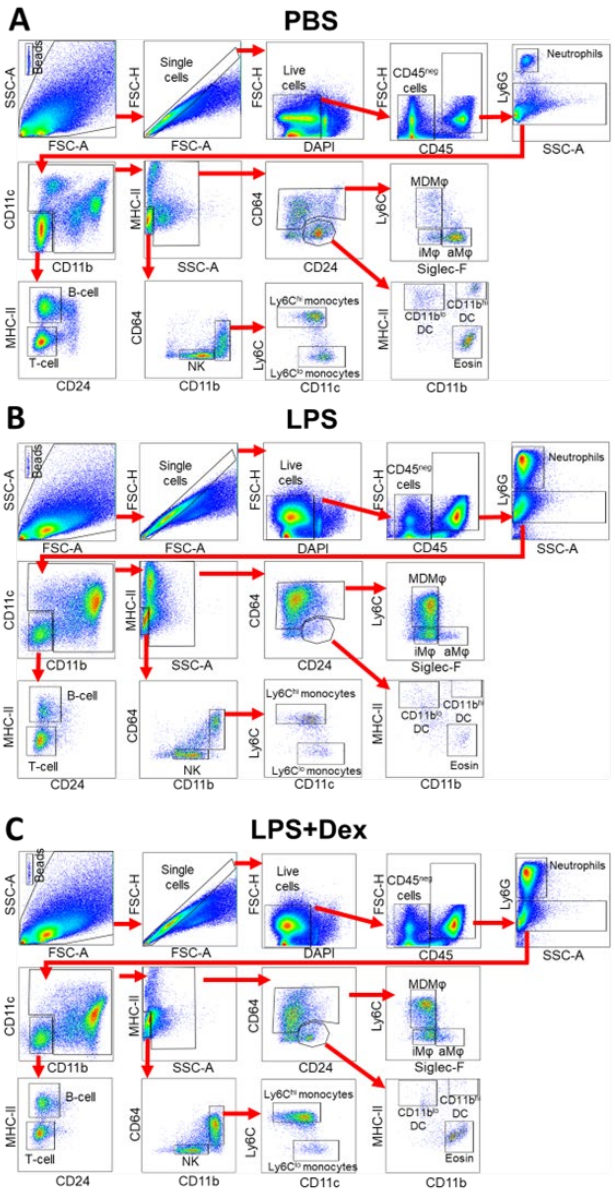

Appendix Figure 24. Gating strategy used for separation of cell types by flow cytometry under different treatment conditions.

The gating strategy used to identify the indicated cell populations is shown for mice treated with (**A**) PBS (top), (**B**) LPS (middle), and (**C**) LPS+Dex (bottom). The same gating strategy was applied to the isolated cells under all treatment conditions. Abbreviations: PBS = phosphate buffered saline, LPS = lipopolysaccharide, Dex = dexamethasone.

Appendix A.2 Supplemental Tables

Supplemental Table 1. List of reagents used for flow cytometry.

Reagent	Assay	Company	Catalog
Anti-CD11b-PE	Flow cytometry	BioLegend	101208
Anti-CD11c-PerCP	Flow cytometry	BioLegend	117326
Anti-CD24-AF700	Flow cytometry	BioLegend	101836
Anti-CD45-BV421	Flow cytometry	BioLegend	103134
Anti-CD64-APC	Flow cytometry	BioLegend	139306
Anti-Ly6C-APC-Cy7	Flow cytometry	BioLegend	128026
Anti-Ly6G-BV395	Flow cytometry	BD Biosciences	563978
Anti-MHC-II-BV605	Flow cytometry	BioLegend	107639
Anti-SiglecF-BV510	Flow cytometry	BD Biosciences	740158
DAPI	Flow cytometry	BD Biosciences	564907
Mouse Fc block	Flow cytometry	BD Pharmingen	553141
Precision count beads	Flow cytometry	BioLegend	424902

Supplemental Table 2. Composition of 10x cytokine lysis buffer used in preparing lung homogenates for ELISA.

Cytokine lysis buffer pH 7.4	Amount of reagents per 100 mL	Concentration of 10x stock
Triton-X 100	5.0 mL	5%
NaCl	8.77 g	1500 mM
Tris	1.82 g	150 mM
$CaCl_2$	1 mL of 1.0 M	10 mM
$MgCl_2$	1 mL of 1.0M	10 mM
diH_2O	Add to a final volume of 100	---

Supplemental Table 3. List of ELISA kits used to measure lung cytokine or chemokine protein expression.

Protein	Company	Catalog #
IL-1β	R&D Systems	DY401
IFN-γ	R&D Systems	DY485
IL-6	R&D Systems	DY406
CXCL1	R&D Systems	DY453

Supplemental Table 4. Hexokinase activity assay buffer.

Reagent	Concentration
Distilled water	---
Tris-base	50 mM
$MgCl_2$	10 mM
Glucose	100 mM
Glycose-6-phosphate dehydrogenase	0.25 U/mL
$NADP^+$	0.20 mM
ATP	0.60 mM
1-methoxy-5-methylphenazinium methyl sulfate	0.32 mM
Nitro blue tetrazolium chloride	0.70 mM
Note: The reagents were added in order (top to bottom), and the pH was adjusted to 7.5 with NaOH (1.0 M) or HCl (1.0 M) after the addition of each chemical.	

Supplemental Table 5. Lactate dehydrogenase activity assay buffer.

Reagent	Concentration
PBS (1x)	---
NaN_3	5.0 mM
NAD^+	3.0 mM
Sodium lactate	125 mM
1-methoxy-5-methylphenazinium methyl sulfate	0.32 mM
Nitro blue tetrazolium chloride	0.70 mM
Note: The reagents were added in order (top to bottom), and the pH was adjusted with NaOH (1.0 M) or HCl (1.0 M) after the addition of each chemical.	

Appendix B Supplemental information for "Molecular Imaging of Chemokine-Like Receptor 1 (CMKLR1) in Experimental Acute Lung Injury"

Appendix B.1 Supplemental Methods

Appendix B.1.1 Tracer synthesis and characterization

NODAGA-CG34, $Chem_{145\text{-}157}$ and 6CF-$Chem_{145\text{-}157}$ were synthesized by the University of Pittsburgh Peptide and Peptoid Synthesis Core Facility. NODAGA-CG34 (NODAGA-Ahx-Y-Cha-Hyp-G-Cit-F-a-Tic-S-COOH) synthesis was performed on a Liberty CEM microwave synthesizer using fluorenylmethyloxycarbonyl (Fmoc) chemistry at a 0.1 mmol scale. Stepwise addition of each Fmoc-protected amino acid to p-alkoxybenzyl alcohol (Wang) resin was accomplished using ethyl-(2Z)-2-cyano-2-hydroxyiminoacetate/N,N-Diisopropylcarbodiimide (Oxyma/DIC) activation chemistry. Upon completion of peptide chain assembly, the N-terminal amino group of the peptide resin was manually coupled with 6-(Fmoc-amino)hexanoic acid (Fmoc-6-Ahx-OH) using N,N-diisopropylethylamine/N,N,N′,N′-tetramethyl-O-(benzotriazol-1-yl)uronium tetrafluoroborate/1-hydroxybenzotriazole (DIPEA/TBTU/HOBt) for 2 hours at room temperature. Manual deprotection of the final Fmoc group using 20% piperidine was followed by on-resin attachment of NODAGA-NHS (5 eq.) in DIPEA / N,N-dimethylformamide (DMF) for 2 hours at room temperature. Cleavage of NODAGA-CG34 from the Wang resin was performed using trifluoroacetic acid (TFA): triisopropylsilane:H_2O (TFA:TIPS:H_2O) (90:25:25) for 2 hours at room temperature followed by precipitation in diethyl Ether (Et_2O). The resulting crude peptide was purified by preparative C-18 RP-HPLC on a Waters Delta Prep 4000 chromatography system

and standard acetonitrile (ACN) / 0.1%TFA gradient conditions. Analytical C-18 RP-HPLC characterization on a Waters Alliance chromatography system followed by high resolution mass spectrometry (HRMS) using a Thermo Scientific Q-Exactive Oribtrap (Mass Spectrometry Lab, University of Pittsburgh) confirmed the expected purity (>95%) and mass of the final product (FTMS -p ESI, Expected $C_{77}H_{108}O_{22}N_{15}$ = 1594.77879, found 1594.78165), respectively. The characterization for NODAGA-CG34 (NODAGA-Ahx-Y-Cha-Hyp-G-Cit-F-a-Tic-S-COOH) is shown in Fig. S1 and Fig. S2. Two additional peptides, $Chem_{145\text{-}157}$ (P-H-S-F-Y-F-P-G-Q-F-A-F-S-COOH) and 6CF-$Chem_{145\text{-}157}$ (6-carboxyfluorescein-P-H-S-F-Y-F-P-G-Q-F-A-F-S-COOH) were also synthesized using related solid phase peptide chemistry and were similarly characterized using HPLC and mass spectrometry.

Appendix B.1.2 Transient transfection

HeLa cells at 70-90% confluency were transiently transfected with mouse CMKLR1 and/or $G_{\alpha 15}$ cDNA plasmids using Lipofectamine 3000 according to manufacturer's instructions. Co-transfections of mouse CMKLR1 and $G_{\alpha 15}$ were conducted at a ratio of 4:1. On day one post-transfection, cells were seeded on poly-D-lysine coated black or clear 96-well plate for calcium mobilization or radioligand bind assays, respectively, at a density of ~40,000 cells/well. The transfected cells were grown in complete growth media until use in a calcium flux or radioligand binding assay on day two post-transfection.

Appendix B.1.3 Calcium mobilization assay

The calcium flux assay was performed according to the manufacturer's instructions with minor

modifications. HeLa cells transiently transfected with mouse CMKLR1 and/or $G_{\alpha 15}$ were washed with assay buffer (HBSS with Ca^{+2} and Mg^{+2}, supplemented with 20 mM HEPES and 2 mM probenecid), and loaded with Fluo-4 AM dye dissolved in loading buffer (assay buffer supplemented with 2.5 μM Fluo-4 and 0.2% Pluronic F-127) for 30 minutes at 37 °C in the dark. Then, cells were washed twice and incubated with assay buffer. A baseline fluorescence measurement was recorded by a Synergy H4 Hybrid Multi-Mode Microplate Reader (Biotek) using the following parameters for 4 minutes: excitation: 490 nm, emission: 515 nm, bandwidths: 9 nm, and frequency: 10 seconds. Subsequently, cells were stimulated with different concentrations of either NODAGA-CG34 or $Chem_{145\text{-}157}$, and kinetic fluorescent measurements were performed every 10 seconds for 4 minutes. The maximum response values (F) were normalized to baseline values (F_0) for each well with the following equation: response = F/F_0. Dose-response curves were generated using GraphPad Prism 9 Software.

Appendix B.1.4 Radioligand binding assay

HeLa cells transiently transfected with mouse CMKLR1 were washed with a binding buffer (50 mM HEPES, 1.0 mM $CaCl_2$, 5.0 mM $MgCl_2$, 0.5% BSA, pH: 7.5). Cells were then incubated at room temperature in the binding buffer with [^{64}Cu]NODAGA-CG34 (0 to 1,000 nM) in the absence or presence of 2.5 μM $Chem_{145\text{-}157}$ to measure total and non-specific binding, respectively. After 1 hour, cells were washed twice with ice-cold binding buffer and lysed with 0.2 M NaOH / 1% SDS. The radioactivity of cell lysates was quantified in a γ-counter (Wizard2, PerkinElmer). The total, non-specific, and specific saturation binding curves were generated (227) using GraphPad Prism 9 Software.

Appendix B.1.5 Measurement of octanol/water partition coefficient (logD)

Approximately 1.48 MBq of [^{64}Cu]NODAGA-CG34 (in 5 µL) was added to a 1 mL mixture of 1-octanol (500 µL) and PBS (500 µL). The mixture was vigorously vortexed for one minute and then centrifuged at 1,000 rpm for 5 minutes. The sample was then placed at room temperature for 30 minutes to allow the phases to completely separate. An equal aliquot (25-50 µL) was carefully removed from each the organic and aqueous layers and counted with a γ-counter (Wizard^2, PerkinElmer). The octanol/water partition coefficient (logD) was calculated as: log([^{64}Cu]NODAGA-CG34$_{Octanol}$ / [^{64}Cu]NODAGA-CG34$_{PBS}$).

Appendix B.1.6 Plasma stability assay

Plasma stability assay was performed according to previous reports (228) with minor modifications. [^{64}Cu]NODAGA-CG34 (~22 – 26 MBq in 70 µL of radiolabeling buffer) was added to 700 µL of C57BL/6 mouse plasma (Innovative Research). The mixture was incubated at 37 °C. At specific time points, an aliquot of ~60 µL (0, 2, and 4 hours) or 100 µL (19 hours) was removed, diluted with acetonitrile (> 1:1 plasma/radiotracer: acetonitrile), and centrifuged at 14,000 g for 5 minutes. Supernatant was carefully removed and diluted up to 200 µL with water and analyzed by radio-HPLC using the method described above.

Appendix B.1.7 Plasma protein binding assay

Plasma protein binding assay was performed per previous reports (229) with minor modifications. [^{64}Cu]NODAGA-CG34 (1.0 µL undiluted from radiolabeling stock, ~0.185 MBq)

was added to 50 µL of mouse plasma. The mixture was briefly vortexed and incubated at 37 °C. At 15 or 90 minutes after incubation, 25 µL of the plasma/radioligand mixture was carefully added to the resin of a prepared (protocol from manufacturer) G50 Microspin column. The samples were centrifuged at 2,000 *g* for 2 minutes. The radioactivity in both the eluent and remaining on the column were counted with a γ-counter (Wizard2, PerkinElmer). Plasma protein binding was calculated as follows: $[^{64}Cu]NODAGA\text{-}CG34_{eluent}$ / ($[^{64}Cu]NODAGA\text{-}CG34_{eluent}$ + $[^{64}Cu]NODAGA\text{-}CG34_{column}$).

Appendix B.1.8 Radiolysis stability measurement

Undiluted samples of $[^{64}Cu]$NODAGA-CG34 in radiolabeling buffer (~ 37 MBq/0.100 mL of initial activity) were left overnight at room temperature. The following morning, an aliquot of $[^{64}Cu]$NODAGA-CG34 (~ 1.1 – 1.9 MBq) was analyzed by radio-HPLC to evaluate radiolysis.

Appendix B.1.9 $[^{64}Cu]$NODAGA-CG34 autoradiography of lungs

Immediately following PET/CT imaging, mice were euthanized, and the lungs were inflated with 1 mL of warmed (37 °C) optimal cutting temperature compound (OCT). Then, the lungs were placed in a block of OCT, quickly frozen, and placed at -20 °C. The following morning cryosections were cut (10 µm) and exposed to high-resolution phosphor screens (GE, BAS-IP SR2025 Super Resolution) overnight at 4 °C. Phosphor screens were scanned at 100-µm resolution using a Sapphire Biomolecular Imager.

Appendix B.1.10 Binding/uptake of 6CF-Chem$_{145-157}$ by peritoneal macrophages

Peritoneal cells were incubated in indicator-free RPMI in the presence of 6CF-Chem$_{145-157}$ (0 – 500 nM) with or without co-incubation with unlabeled Chem$_{145-157}$ (2.5 μM). Uptake of 6CF-Chem$_{145-157}$ was allowed to proceed at 37 °C for 1 hour, vortexing samples every ~15 minutes. After a single wash with PBS, flow cytometry was performed using a BD FACSCalibur (BD Biosciences) and analyzed by FlowJo software version 10.7.2 (BD Biosciences). The total, non-specific, and specific saturation binding curves were generated using GraphPad Prism 9 Software.

Appendix B.1.11 Competitive binding assay of 6CF-Chem$_{145-157}$ and NODAGA-CG34 in peritoneal macrophages

Peritoneal cells were incubated in indicator-free RPMI in the presence of 6CF-Chem$_{145-157}$ (100 nM) with increasing concentrations of NODAGA-CG34 ($1x10^{-10}$ M to $1x10^{-5}$ M). The competitive binding of NODAGA-CG34 and 6CF-Chem$_{145-157}$ was allowed to proceed at 37 °C for 1 hour, vortexing samples every ~15 minutes. After a single wash with PBS, flow cytometry was performed using a BD FACSCalibur (BD Biosciences) and analyzed by FlowJo software version 10.7.2 (BD Biosciences). The competitive binding curves were generated using GraphPad Prism 9 Software.

Appendix B.1.12 Flow cytometry for peritoneal macrophages

Peritoneal cells were incubated in indicator-free RPMI in the absence or presence of 6CF-Chem$_{145-157}$ (100 nM) with or without co-incubation with Chem$_{145-157}$ (10 μM). Uptake of 6CF-

Chem$_{145\text{-}157}$ was allowed to proceed at 37 °C for 1 hour, vortexing samples every ~15 minutes. After washing with PBS, blocking was performed by 1% BSA in PBS and Fc block (2.0 µL per sample). Subsequently, a mixture of antibodies (0.5 µL per antibody per sample) was added for 0.5 hour at 4 °C. Finally, cells were washed and fixed with 4% formalin for 0.5 hour at room temperature. Flow cytometry was performed the following day using a LSR II Flow Cytometry (BD Biosciences) and analyzed by FlowJo software version 10.7.2 (BD Biosciences).

Appendix B.1.13 Single-nuclei RNA sequencing (snRNA-seq) of COVID-19 and control lungs

A secondary analysis of a previously published snRNA-seq dataset from the autopsied lungs of nineteen patients with lethal COVID-19 and lung tissue (biopsy or lung resection) from seven pre-pandemic control patients without COVID-19 was performed to determine the expression of *CMKLR1* among different cell types in the lungs. The RNA sequencing data are available in the Gene Expression Omnibus (GEO) database under accession number GSE171524. Data collection and analysis were conducted as previously reported (138). Major cell populations were identified using UMAP analysis, as described in the original paper (138). The abundance and expression level of *CMKLR1* among different cell subsets were determined and compared between COVID-19 patients and controls.

Differential gene expression was performed using the Seurat (v4.1.0) (140) function 'FindAllMarkers' to identify markers in *CMKLR1*-positive and *CMKLR1*-negative cell populations. MAST algorithm was used to identify differentially expressed genes between the two groups, which were averaged across *CMKLR1*-positive and *CMKLR1*-negative cell populations

for heat map representation with maximum and minimum display values clipped at 0.75 and -0.75, respectively.

Appendix B.1.14 Statistical analysis

Statistical analysis was performed using Prism 9 (GraphPad). Data are presented as mean ± SEM. A student's *t*-test was performed to compare the means values between two groups. One-way analysis of variance, followed by Fisher's Exact post hoc test, was used to compare mean values in > 2 groups. Pearson's test was used to determine the correlations between continuous variables. For snRNA-seq data, the percentage of cells positive for *CMKLR1* and the average *CMKLR1* expression in different cell subsets were compared between COVID-19 and control groups using Fisher's Exact and Wilcoxon rank-sum tests, respectively. Statistical significance was considered as $P < 0.05$.

Appendix B.2 Supplemental Figures

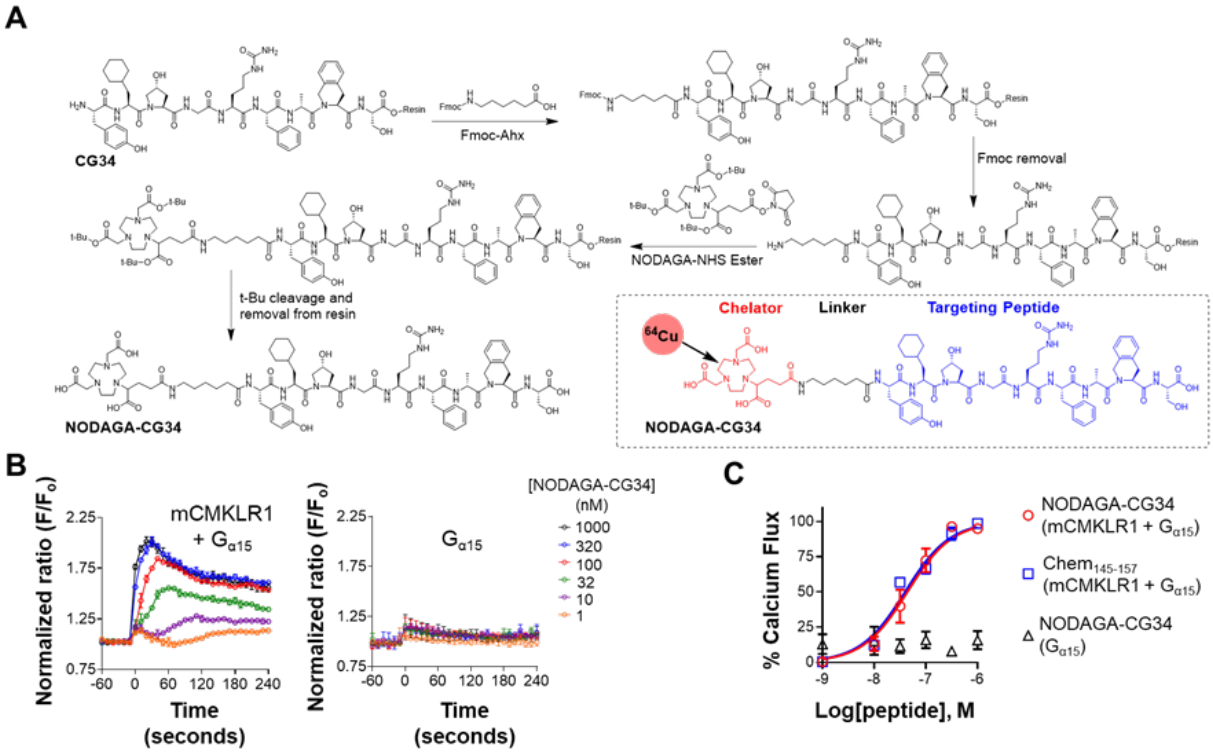

Appendix Figure 25. Synthesis and potency of NODAGA-CG34.

(**A**) Synthetic overview of NODAGA-CG34 which is composed of three moieties: CMKLR1-targeting peptide (CG34), 6-aminohexanoic acid (Ahx) linker, and chelator (NODAGA). (**B**) Representative examples of Ca^{+2} mobilization assay elicited by different concentrations of NODAGA-CG34 demonstrate a transient increase in intracellular calcium, detected by a Fluo-4 fluorescent signal, in HeLa cells transiently expressing mouse CMKLR1 (mCMKLR1) and $G_{\alpha15}$ (left) but not in cells transfected with $G_{\alpha15}$ alone (right). (**C**) Concentration-response curves demonstrate the high potency of NODAGA-CG34 to CMKLR1 which is similar to a natural chemerin-derived peptide ($Chem_{145-157}$) (EC_{50} of 45.7 ± 15.4 nM *vs.* 42.2 ± 3.8 nM, respectively, $P = 0.95$, N = 3 independent experiments). Data are expressed as the mean ± SEM. Statistical significance was calculated using a two-tailed Student's t-test.

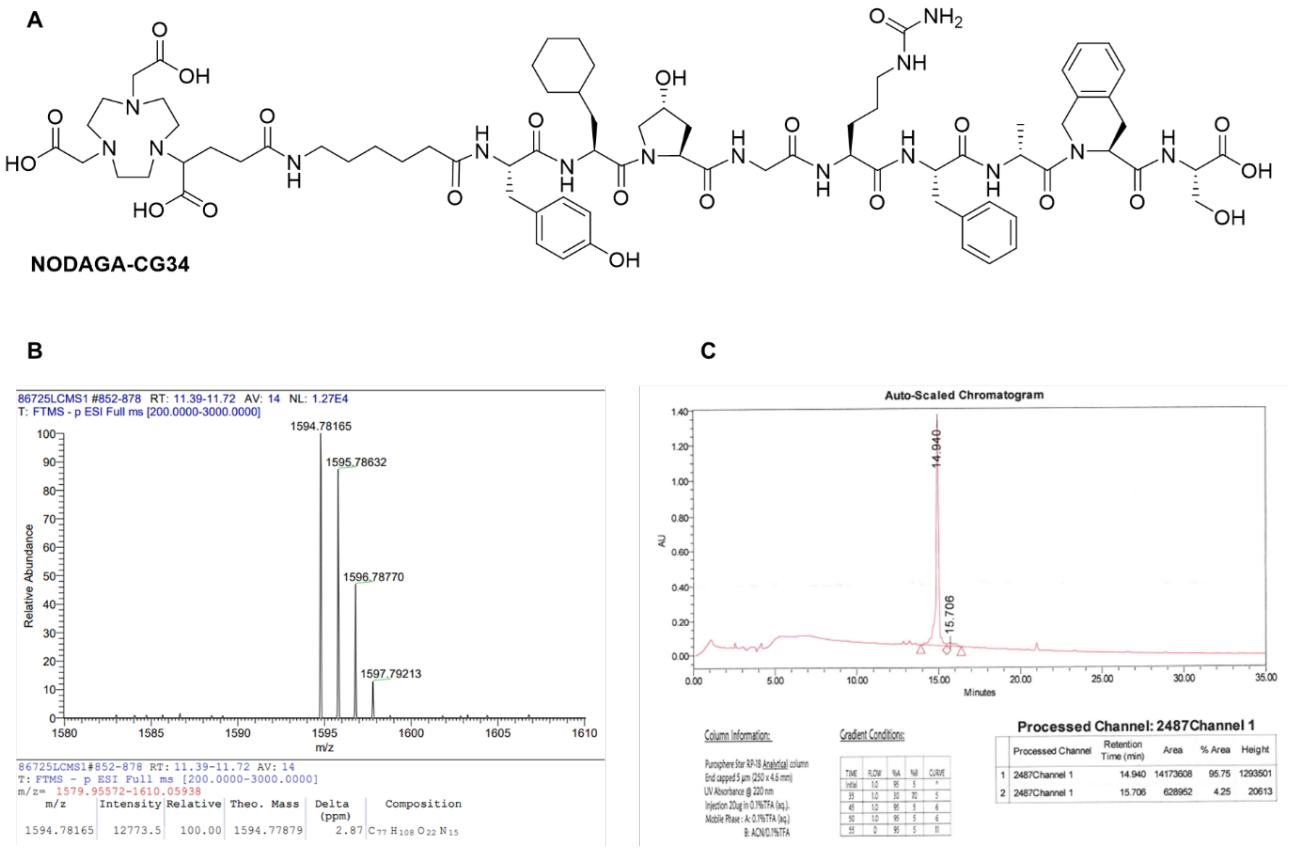

Appendix Figure 26. Confirmation of the identity and purity of NODAGA-CG34.

(**A**) Structure of NODAGA-CG34. (**B**) High resolution mass spectrometry confirms the expected mass and molecular formula of NODAGA-CG34 ($C_{77}H_{108}O_{22}N_{15}$ = 1594.77879, found: 1594.78165). (**C**) The chemical purity (96%) of NODAGA-CG34 is confirmed by analytical reverse-phase high performance liquid chromatography.

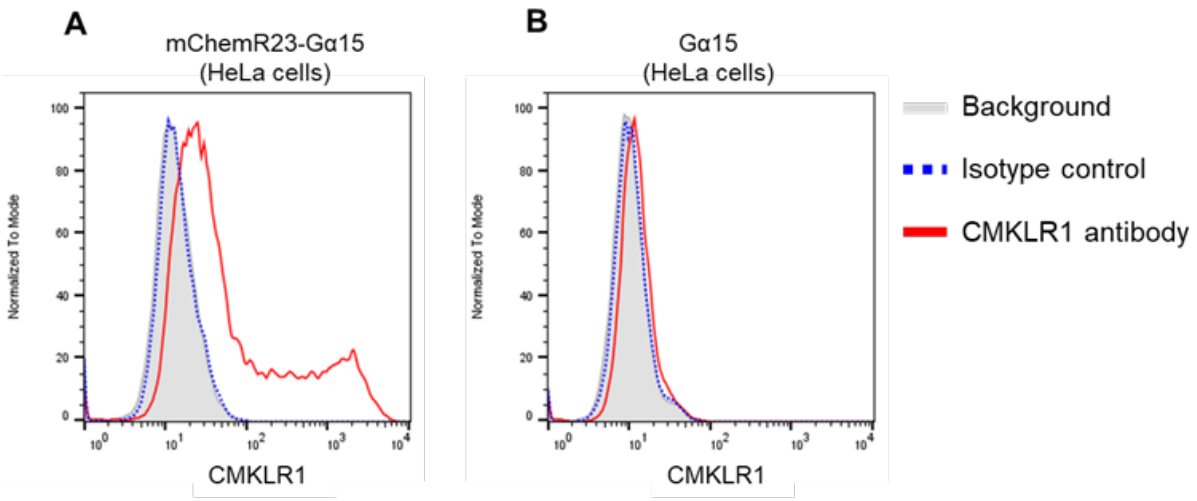

Appendix Figure 27. Surface expression of CMKLR1 in HeLa cells transfected with CMKLR1 and $G_{\alpha 15}$ *vs.* $G_{\alpha 15}$ alone.

(**A**) HeLa cells transiently transfected with mouse CMKLR1 (mCMKLR1) and Gα15 demonstrate surface expression of mCMKLR1 as confirmed by flow cytometry using an anti-mCMKLR1 antibody. (**B**) By contrast, HeLa cells transiently transfected with $G_{\alpha 15}$ alone do not show binding of the anti-mCMKLR1 antibody. N = 3 independent experiments.

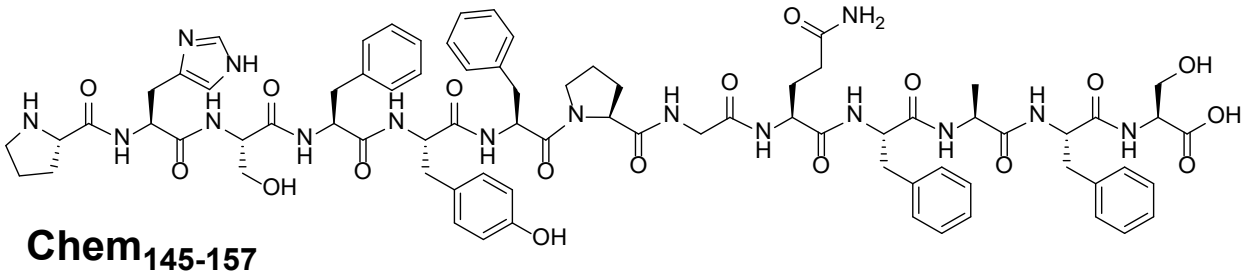

Appendix Figure 28. Structure of Chem145-157 peptide.

The structure of $Chem_{145-157}$ is shown above.

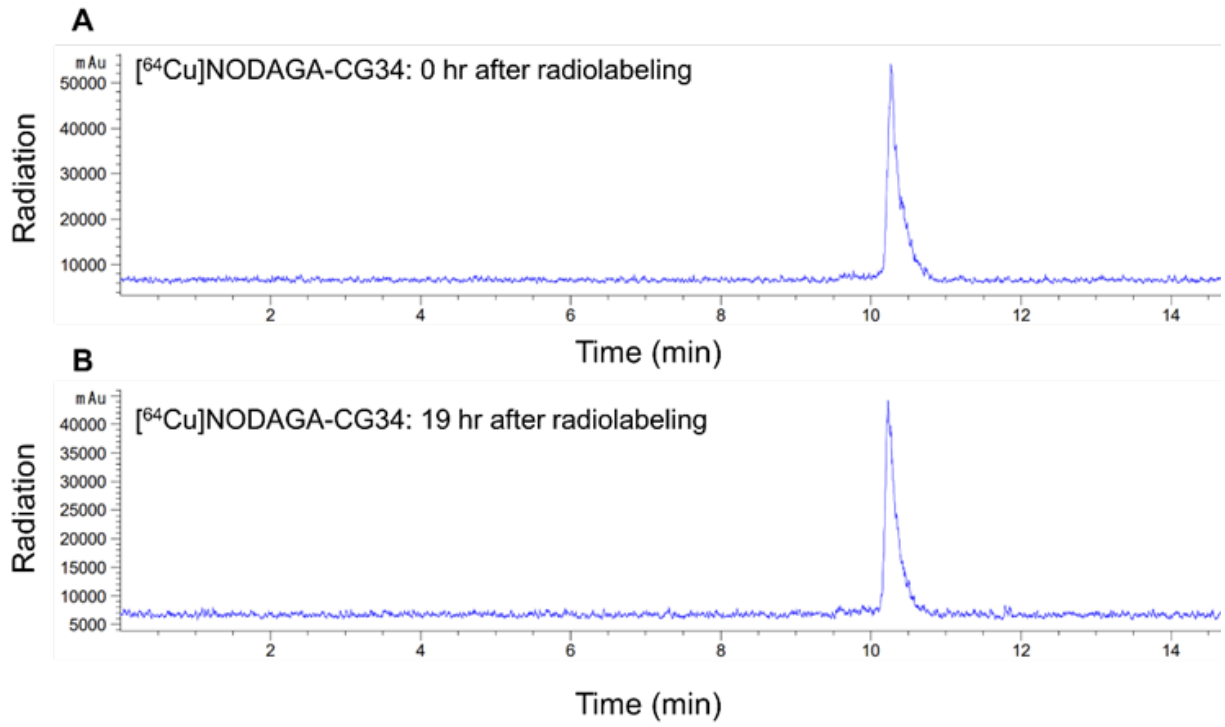

Appendix Figure 29. Stability of [^{64}Cu]NODAGA-CG34.

(**A**) A radio-HPLC immediately following radiolabeling of NODAGA-CG34 with [^{64}Cu]Cu^{+2} shows ~100% radiochemical purity. (**B**) A repeat radio-HPLC after [^{64}Cu]NODAGA-CG34 was stored overnight under ambient conditions shows no new peaks, demonstrating a high degree of stability with no observable radiolysis. N = 2 independent experiments.

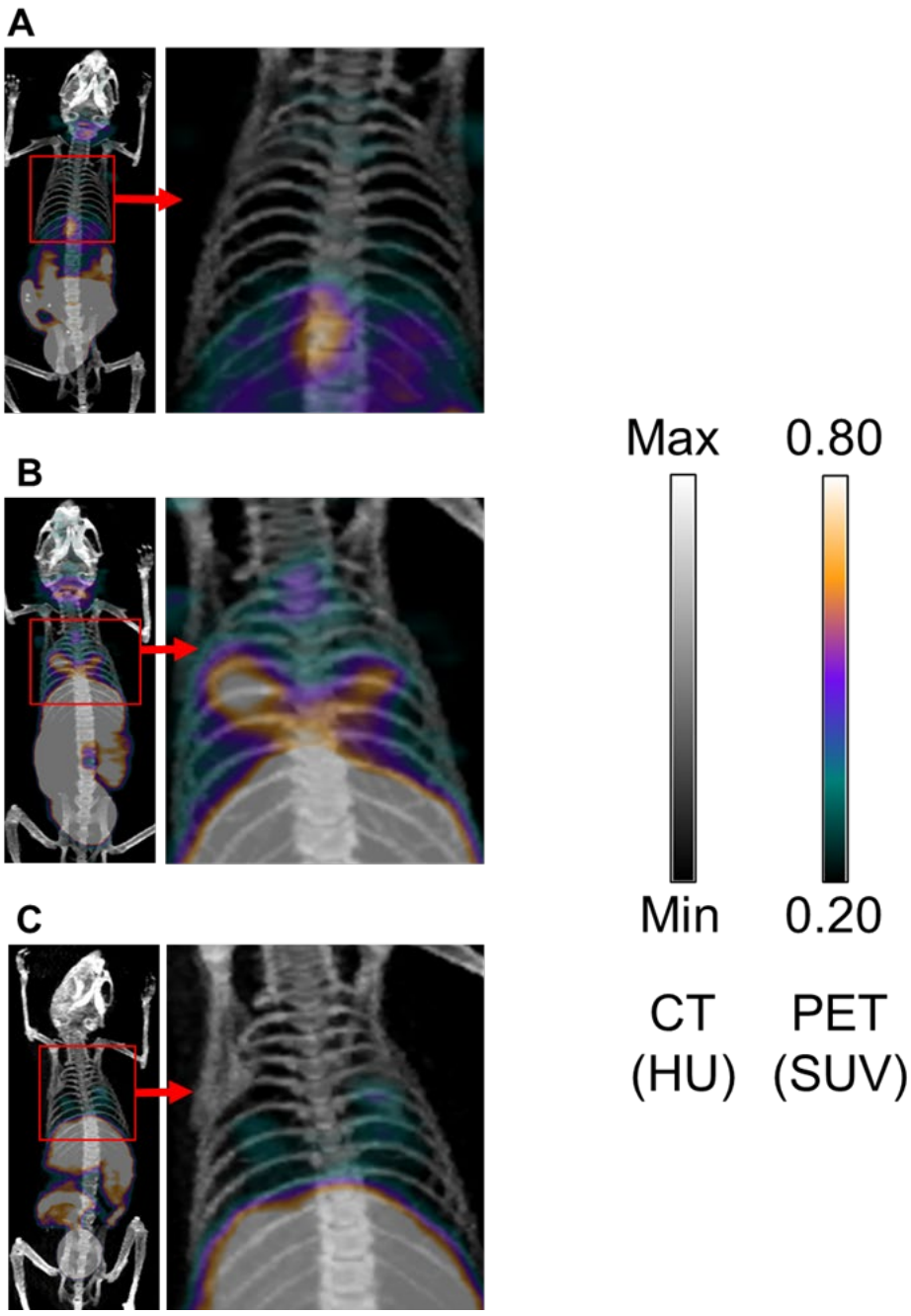

Appendix Figure 30. [^{64}Cu]NODAGA-CG34 PET/CT in LPS-induced lung injury.

Maximum intensity projection (MIP) PET/CT images from a control mouse (**A**) *vs.* a mouse at day 2 post-LPS administration (**B**) demonstrate focal areas of increased tracer uptake in ALI. The specificity of tracer uptake is confirmed by co-injection of 100-fold molar excess of non-radiolabeled NODAGA-CG34 which blocks the lung uptake of [^{64}Cu]NODAGA-CG34 in ALI (**C**). The notable increase in the specific uptake of [^{64}Cu]NODAGA-CG34

in the liver, intestines and spleen of ALI mice is compatible with the induction of a systemic inflammatory response by intra-tracheal LPS.

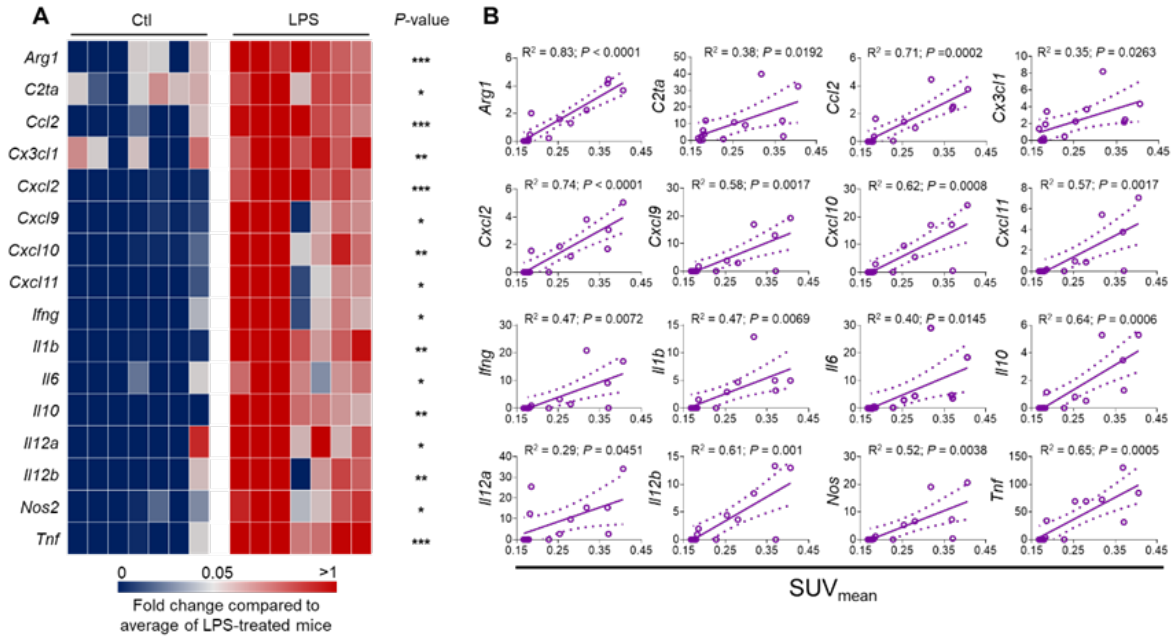

Appendix Figure 31. Correlation of [^{64}Cu]NODAGA-CG34 uptake and the expression of inflammatory markers.

(**A**) The mRNA expression of multiple inflammatory markers is markedly increased in the lungs two days after induction of LPS-induced experimental lung injury. (**B**) PET-derived quantification of lung [^{64}Cu]NODAGA-CG34 uptake significantly correlates with the expression of multiple inflammatory markers. mRNA transcript levels are normalized to the geometric mean of *Rn18s*, the housekeeping gene. PBS = phosphate buffered saline; LPS = lipopolysaccharide. Linear regressions are shown along with 95% confidence intervals. *P*-values: * < 0.05; ** < 0.01; *** < 0.001; **** < 0.0001. Statistical significance was calculated using a two-tailed Student's t-test. Linear correlations were determined by calculating the Pearson correlation coefficient.

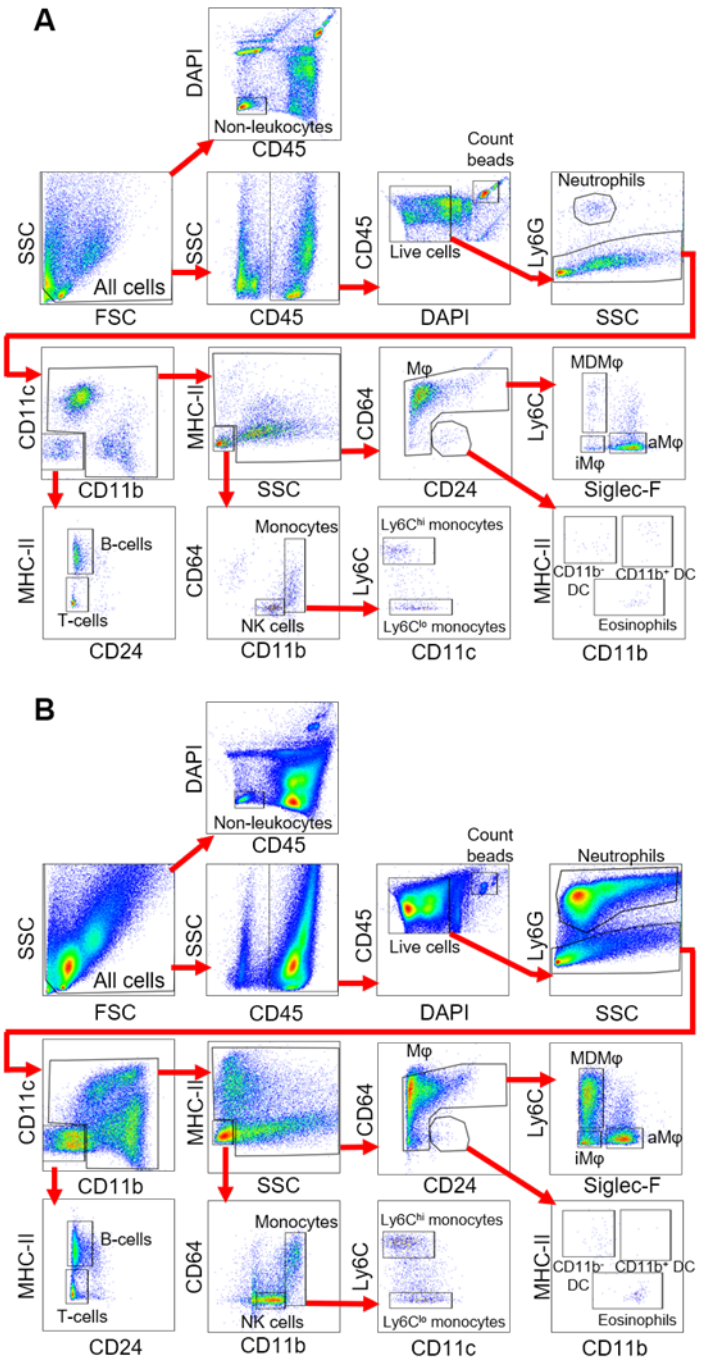

Appendix Figure 32. Flow cytometric gating strategy for identification of major leukocyte subsets in murine lungs.

An 11-color flow cytometry panel was adapted for identification of major leukocyte subsets in murine lungs. Representative examples are shown from lungs of PBS (**A**) *vs.* lipopolysaccharide (**B**) treated mice. aMφ: alveolar

macrophages; DC: dendritic cells; iMφ: interstitial macrophages; Mφ: macrophages; MDMφ: monocyte-derived macrophages; NK: natural killer cells.

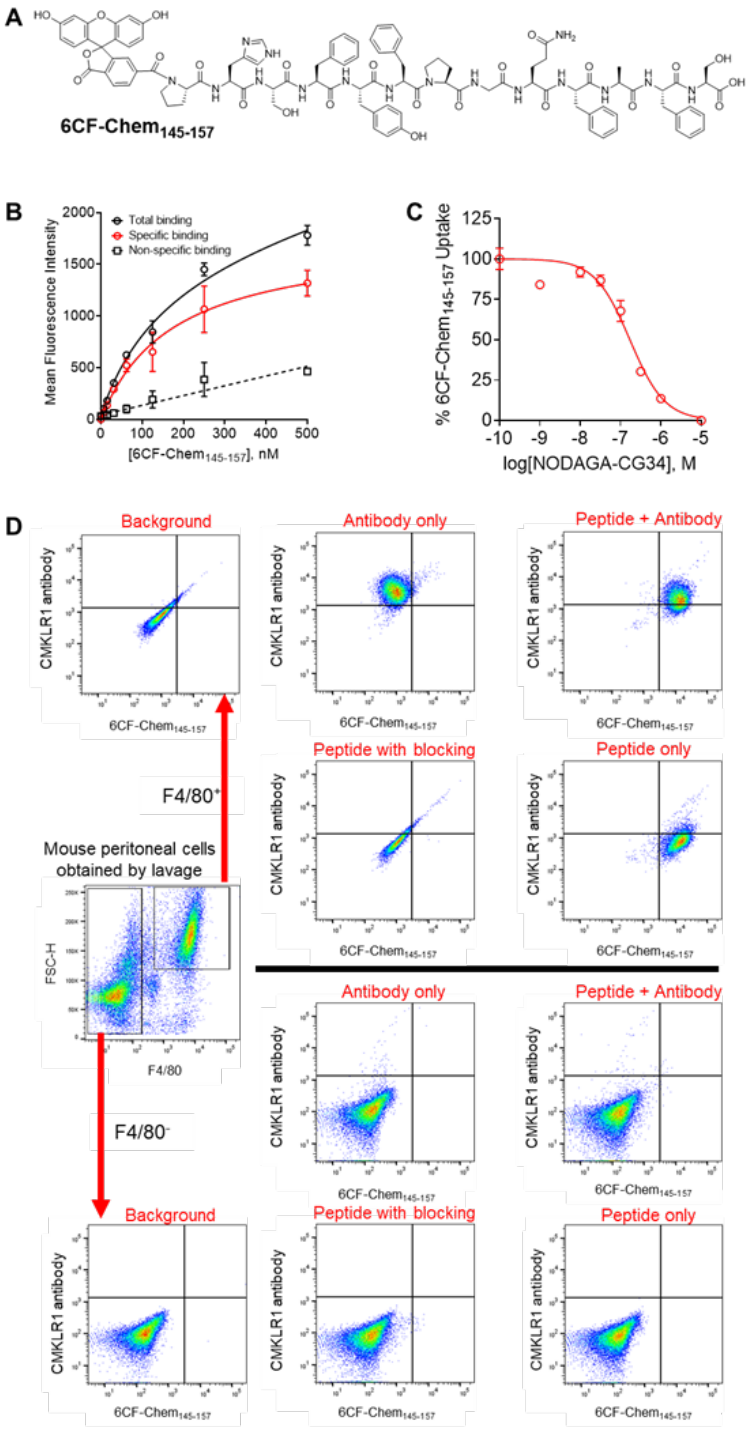

Appendix Figure 33. Specificity of 6CF-Chem$_{145-157}$ for mCMKLR1.

(**A**) The structure of 6CF-Chem$_{145-157}$ is shown. (**B**) The potency (EC_{50}) of 6CF-Chem$_{145-157}$ at mCMKLR1 on F4/80^{+} peritoneal macrophages is 246.3±48.3 nM (N = 3 independent experiments). (**C**) NODAGA-CG34 competes with 6CF-Chem$_{145-157}$ for binding and uptake at CMKLR1 (IC_{50} = 163.3±21.0 nM; N = 3 independent experiments). (**D**) CMKLR1-expressing F4/80^{+} peritoneal macrophages demonstrate specific uptake of 6CF-Chem$_{145-157}$. In contrast, there is no binding of 6CF-Chem$_{145-157}$ in the remaining non-macrophage peritoneal cells (F4/80^{-}). Together, these data confirm the specificity and restricted binding of 6CF-Chem$_{145-157}$ to CMKLR1-expressing cells. Blocking studies were conducted by co-incubation of cells with 6CF-Chem$_{145-157}$ and 100-fold excess Chem$_{145-157}$.

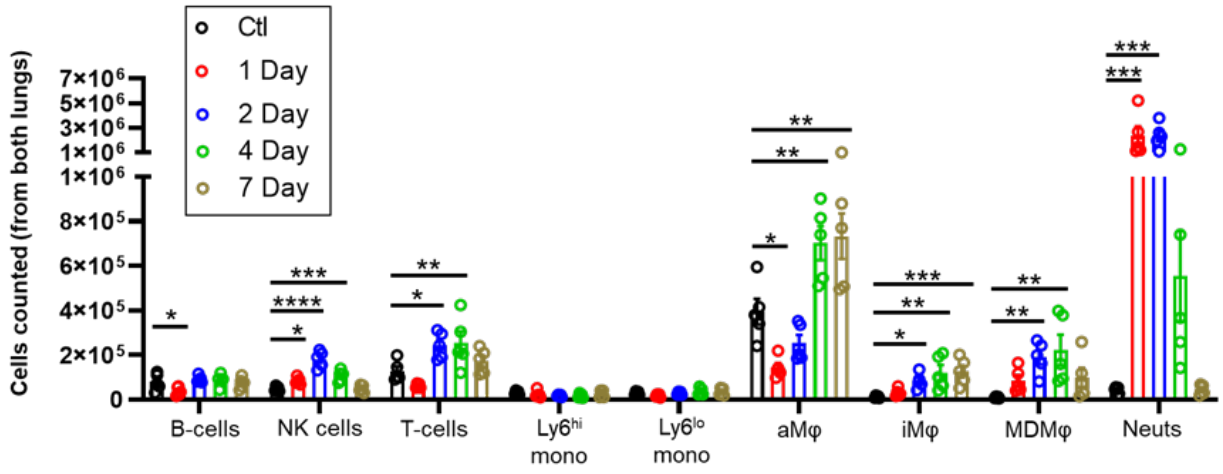

Appendix Figure 34. Kinetics of lung leukocyte populations during LPS-induced ALI as determined by flow cytometry.

The absolute cell count for the indicated cell populations at specific time points in lipopolysaccharide (LPS) treated or untreated control mice. Ctl = untreated mice; LPS = lipopolysaccharide; Ly6C^{hi} mono = Ly6C^{hi} monocytes; Ly6C^{lo} mono = Ly6C^{lo} monocytes; aMφ = alveolar macrophages; iMφ = interstitial macrophages; MDMφ = monocyte derived macrophages. n=3 male and n=2 female mice in each group, except for day 2 with n=2 male and n=3 female mice. aMφ: alveolar macrophages; iMφ: interstitial macrophages; MDMφ: monocyte-derived macrophages; NK cells: natural killer cells; Neuts: neutrophils. Data are expressed as the mean ± SEM. *P*-values: * < 0.05; ** < 0.01; *** < 0.001; **** < 0.0001. Statistical significance was calculated using a one-sided ANOVA with a post-hoc two-tailed Fisher's exact test comparing the control group with each treatment group.

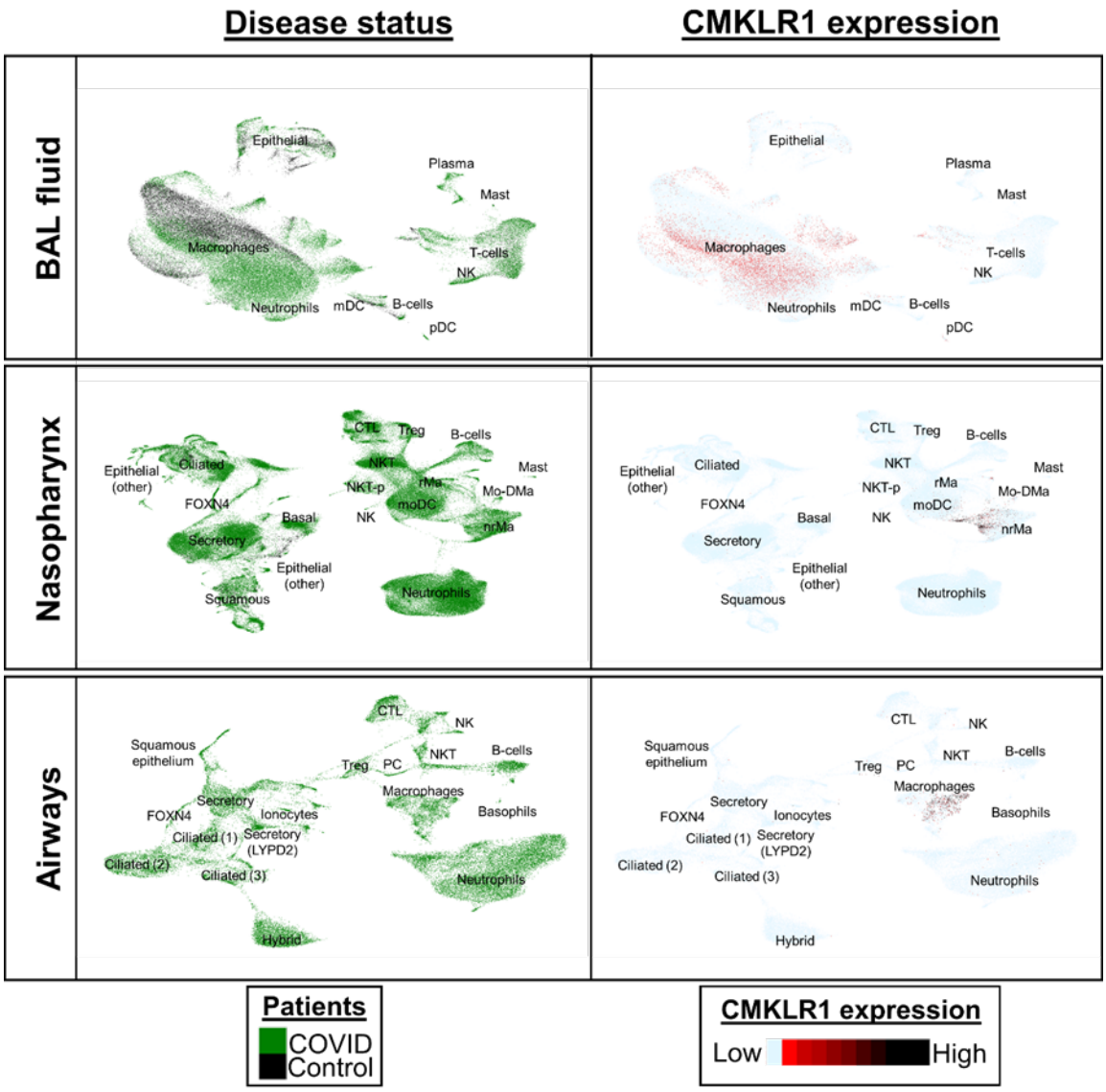

Appendix Figure 35. Increased expression of *CMKLR1* in the respiratory tract of COVID-19 patients is mostly restricted to macrophages.

UMAP display of major cell types (left columns) identified from single-cell RNA sequencing of bronchoalveolar (BAL) fluid (top panel), nasopharynx (middle panel) or airway (lower panel) specimens from patients with COVID-19 or SARS-CoV-2-negative healthy controls. The expression of *CMKLR1* in specimens obtained from all three sites is predominantly restricted to macrophages. Moreover, BAL fluid analysis demonstrates a distinct increase in the expression of *CMKLR1* in macrophages of COVID-19 patients compared to those of controls. The number of patients per panel is as follows: top panel (BAL fluid): N = 9 patients with COVID-19 and 4 healthy controls; middle panel (nasopharynx): N = 19 patients with COVID-19 and 5 healthy controls; and bottom panel (airways): N = 2 patients

with COVID-19. The raw and processed data is available in the Gene Omnibus (GSE145926) and European Genome-Phenome Archive (EGAS00001004481) (141, 142). Data was accessed and analyzed using the UCSC Cell Browser software (144). A link is provided in Table S7 (https://cells-test.gi.ucsc.edu/?ds=ams-supercluster&gene=CMKLR1).

Abbreviations: Ciliated: ciliated epithelial cells; FOXN4: FOXN4^{+} epithelial cells; Secretory: secretory epithelial cells; Squamous: squamous epithelial cells; rMa: resident macrophages; moDC: monocyte-derived dendritic cells; nrMa: non-resident macrophages; Treg: regulatory T-cells; CTL: cytotoxic T-cells; NKT: natural killer T-cells; NKT-p: proliferating natural killer T-cells; NK: natural killer cells; Neu: neutrophils; pDC: plasmacytoid dendritic cells; MC: mast cell; mDC: myeloid dendritic cells.

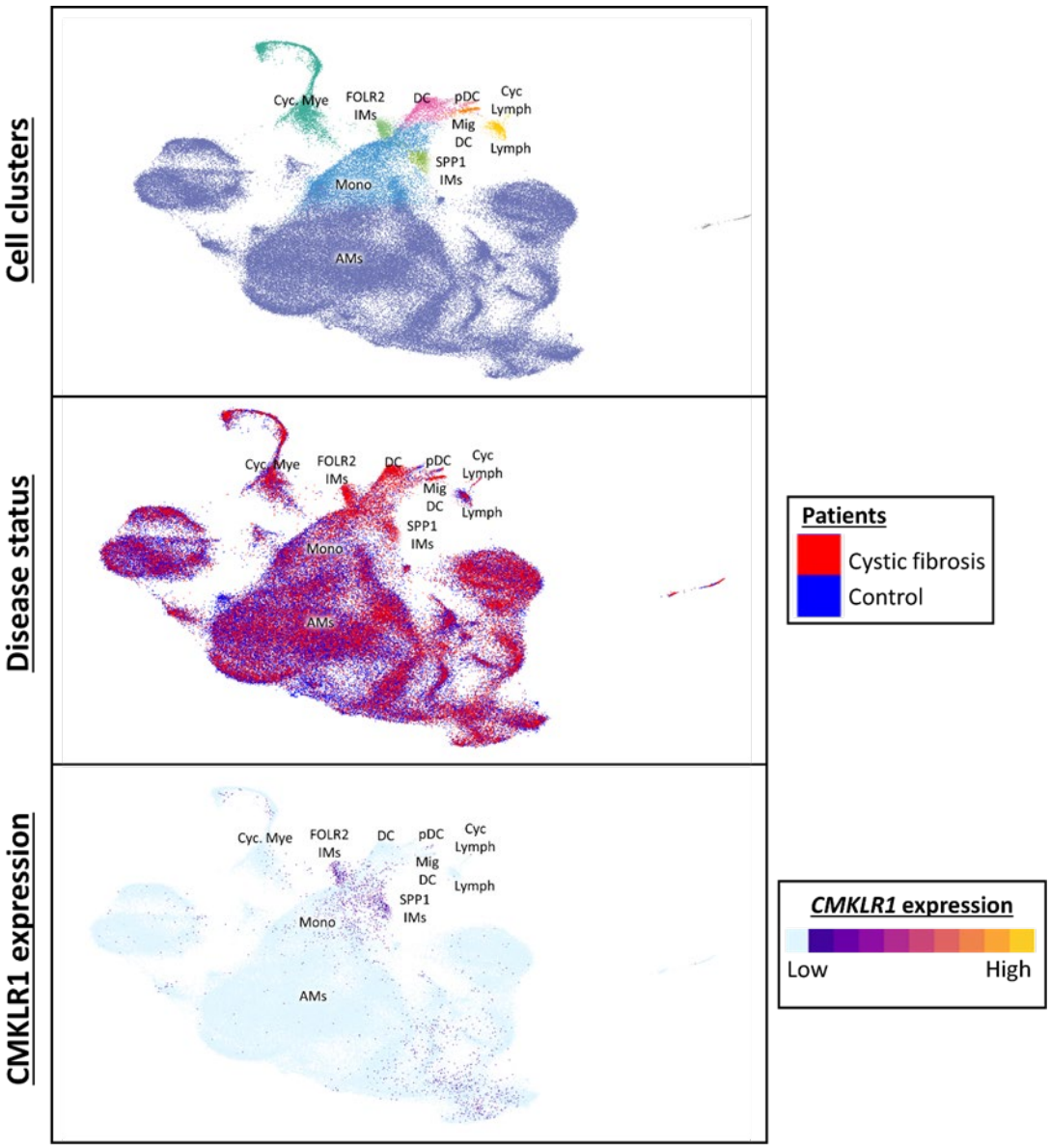

Appendix Figure 36. Restricted expression of *CMKLR1* by macrophages in bronchoalveolar fluid specimens from patients with cystic fibrosis.

UMAP display of major cell types identified from single-cell RNA sequencing of bronchoalveolar lavage (top panel) and their distribution by disease status (middle panel) in three patients with mild cystic fibrosis and four healthy control participants. *CMKLR1* expression (bottom panel) was predominantly restricted to FOLR2^{+} and SPP1^{+} interstitial macrophages in patients with cystic fibrosis with less abundant expression in monocytes and macrophages. The raw and processed data is available in the Gene Omnibus (GSE193782) (143). Data was accessed and analyzed

using the UCSC Cell Browser website (144). A link is provided in Table S7 (https://cells-test.gi.ucsc.edu/?ds=ams-supercluster&gene=CMKLR1).

Abbreviations: AMs: alveolar macrophages; Cyc Lymph: lymphoid cycling cells; FOLR2 IM: FOLR2^{+} interstitial macrophages; SPP1 IM: SPP1^{+} interstitial macrophages; Mig DC: migratory dendritic cells; pDC: plasmacytoid dendritic cells; Lym: lymphocytes.

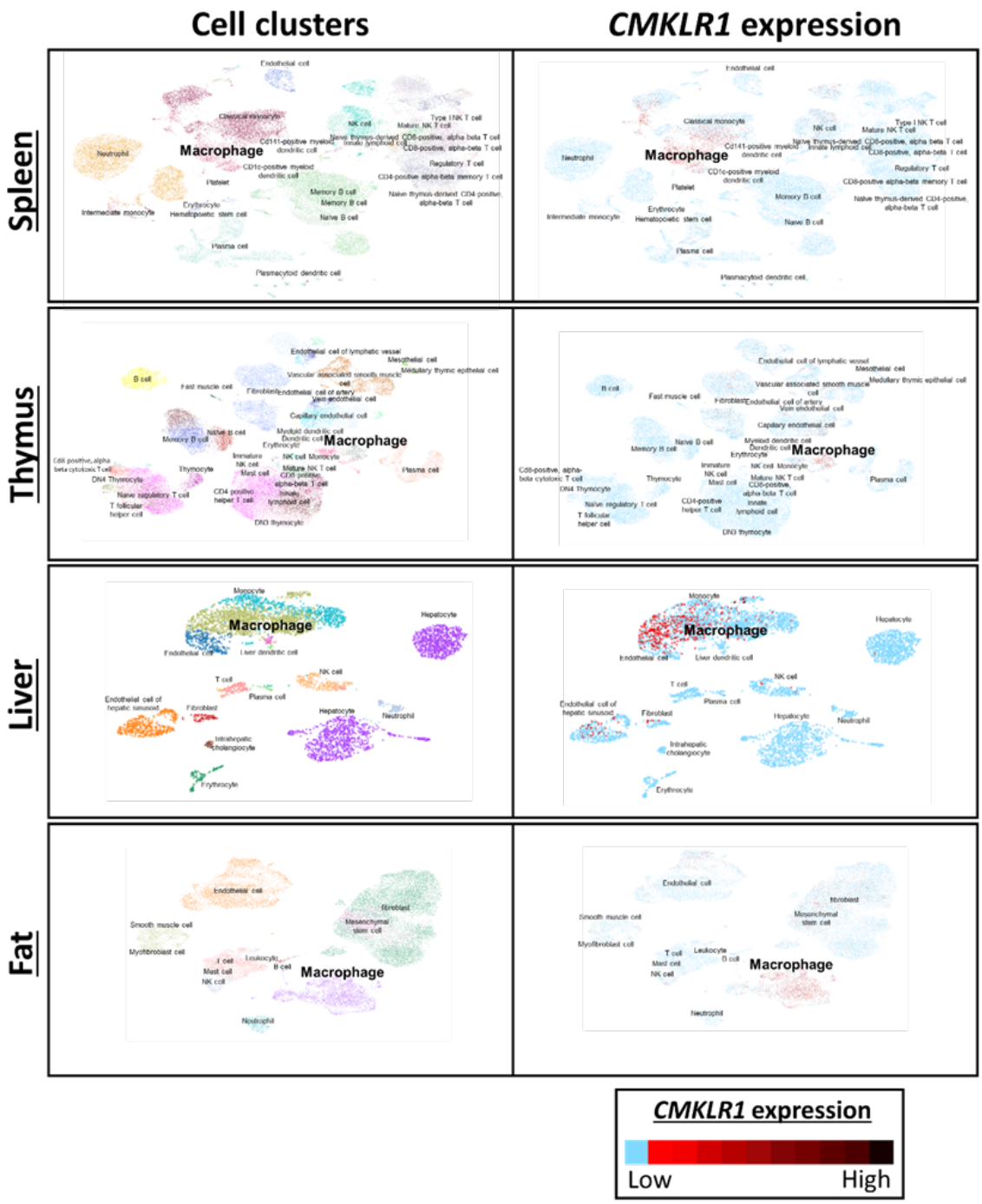

Appendix Figure 37. *CMKLR1* is predominantly expressed on macrophages in various non-pulmonary tissues. UMAP display of major cell types identified from single-cell RNA sequencing of the indicated tissue (left panel) and their *CMKLR1* expression (right panel) in donor tissue. *CMKLR1* expression was largely restricted to macrophages. The raw and processed data is available in the Gene Omnibus (GSE201333). Data was accessed and analyzed using the UCSC Cell Browser website (144). Links to the data are provided in Table S7.

Abbreviations: AMs: alveolar macrophages; Cyc Lymph: lymphoid cycling cells; FOLR2 IM: $FOLR2^{+}$ interstitial macrophages; SPP1 IM: $SPP1^{+}$ interstitial macrophages; Mig DC: migratory dendritic cells; pDC: plasmacytoid dendritic cells; Lym: lymphocytes.

Appendix B.3 Supplemental tables

Supplemental Table 6. List of general reagents.

Reagent	Company	Catalog #
Black 96-well plate	Thermo Fisher	165305
C57BL/6 plasma	Innovative Research	IGMSC57PLAK2E10ML
Cell strainer (70 um)	VWR	10199-656
Clear 96-well plate	Fisher	FB012931
Dexamethasone	Fresenius Kabi USA	500601
DMEM	Thermo Fisher	10566016
DNase I	Sigma	D4527-10KU
Fetal bovine serum	Gibco	10082147
Fluo-4 AM	Thermo Fisher	F14201
G50 Microspin column	GE	27-5330-01
HBSS with Ca^{+2} and Mg^{+2}	Gibco	14025-076
Lipofectamine 3000	Thermo Fisher	L3000008
Lipopolysaccharide	Millipore Sigma	437627
Low retention tubes (radiolabeling)	Eppendorf	022431081
Qiagen Plasmid Maxi Kit	Qiagen	12162
PBS	Lonza	17-512F
Penicillin/streptomycin	Gibco	15070-063
Pluronic F-127	Millipore Sigma	P2443
Poly-D-lysine	Thermo Fisher	A3890401
Protease Inhibitor	Thermo Fisher	A32963
RBC Lysis Buffer (10X)	Biolegend	420301
QuantiTect Reverse Transcription Kit	Qiagen	205313
Rodent Intubation Stand	Braintree Scientific	RIS 100
Taqman Master Mix	Thermo Fisher	4369510
Trizol	Thermo Fisher	15596026

Supplemental Table 7. Plasmids for transient transfections.

Plasmid	Company	Catalog
$G_{\alpha 15}$	cDNA Resource Center	GNA1500000
mCMKLR1	Origene	MC208581

Supplemental Table 8. Radio-HPLC methods (Agilent 1260 Infinity HPLC, C18 Luna Analytical Column).

Time (min)	**Solvent 1 (%)** (H_2O with 0.1% v/v trifluoroacetic acid)	**Solvent 2 (%)** (Acetonitrile with 0.1% v/v trifluoroacetic acid)	**Flow rate (mL/min)**
0	100	0	2.0
5	95	5	2.0
15	5	95	2.0

Supplemental Table 9. List of reagents used for flow cytometry.

Reagent	Assay	Company	Catalog #
Anti-CCR2-Fluorescein	Flow cytometry	R&D Biosystems	FAB5538F-100
Anti-CD11b-PE	Flow cytometry	BioLegend	101208
Anti-CD11c-PerCP	Flow cytometry	BioLegend	117326
Anti-CD24-AF700	Flow cytometry	BioLegend	101836
Anti-CD45-BV421	Flow cytometry	BioLegend	103134
Anti-CD64-APC	Flow cytometry	BioLegend	139306
Anti-CMKLR1-AF488	Flow cytometry	R&D Biosystems	FAB7610G
Anti-Ly6C-APC-Cy7	Flow cytometry	BioLegend	128026
Anti-Ly6G-BV395	Flow cytometry	BD Biosciences	563978
Anti-MHC-II-BV605	Flow cytometry	BioLegend	107639
Anti-SiglecF-BV510	Flow cytometry	BD Biosciences	740158
DAPI	Flow cytometry	BD Biosciences	564907
IgG_{2B} isotype control-AF488	Flow cytometry	R&D Biosystems	IC013G
IgG_{2B} isotype control-fluorescein	Flow cytometry	R&D Biosystems	IC013F
Mouse Fc block	Flow cytometry	BD Pharmingen	553141
Precision count beads	Flow cytometry	BioLegend	424902

Supplemental Table 10. List of reagents used for immunofluorescent histology.

Antibody	Assay	Company	Catalog #
Anti-rabbit IgG (H+L) - Cy5	Immunofluorescence	Jackson ImmunoResearch	711-175-152
Anti-rat IgG (H+L) - Cy3	Immunofluorescence	Jackson ImmunoResearch	712-165-150
ProLong Gold Antifade Mountant with DAPI	Immunofluorescence	Thermo Fisher	P36931
Rabbit anti-mouse CMKLR1	Immunofluorescence	LSBio	B12924
Rat anti-mouse CD45	Immunofluorescence	BioLegend	103101
Rat anti-mouse F4/80	Immunofluorescence	Thermo Fisher	14-4801-81
Rat anti-mouse Ly6G	Immunofluorescence	BioLegend	127601

Supplemental Table 11. List of mouse primers used for quantitative RT-PCR.

Assay Name	Gene	Assay ID
Arg1	Arginase 1	Mm00475988_m1
Ccl2	C-C motif chemokine ligand 2	Mm00441242_m1
Ciita	Class II major histocompatibility complex transactivator	Mm00482914_m1
Cx3cl1	C-X3-C motif chemokine ligand 1	Mm00436454_m1
Cxcl10	C-X-C motif chemokine ligand 10	Mm00445235_m1
Cxcl11	C-X-C motif chemokine ligand 11	Mm00444662_m1
Cxcl2	C-X-C motif chemokine ligand 2	Mm00436450_m1
Cxcl9	C-X-C motif chemokine ligand 9	Mm00434946_m1
Ifng	Interferon-γ	Mm01168134_m1
Il10	Interleukin 10	Mm01288386_m1
Il12a	Interleukin 12A	Mm00434169_m1
Il12b	Interleukin 12B	Mm00434174_m1
Il1b	Interleukin 1β	Mm00434228_m1
Il6	Interleukin 6	Mm00446190_m1
Nos2	Nitric oxide synthase 2	Mm00440502_m1
Rn18s	18S ribosomal RNA	Mm03928990_m1
Tnf	Tumor necrosis factor	Mm00443258_m1

Supplemental Table 12. Single-cell RNA-seq datasets for CMKLR1 expression.

Sample	Disease	Direct link for dataset	Figure	Ref
Bronchoalveolar lavage	COVID-19	https://cells-test.gi.ucsc.edu/?ds=covid19-balf&gene=CMKLR1	Fig. S11	(141)
Nasopharynx	COVID-19	https://cells-test.gi.ucsc.edu/?ds=covid-airways+nasopharynx&gene=CMKLR1	Fig. S11	(142)
Airways	COVID-19	https://cells-test.gi.ucsc.edu/?ds=covid-airways+all&gene=CMKLR1	Fig. S11	(142)
Bronchoalveolar lavage	Cystic fibrosis	https://cells-test.gi.ucsc.edu/?ds=ams-supercluster&gene=CMKLR1	Fig. S12	(143)
Spleen	Various	https://cells.ucsc.edu/?ds=tabula-sapiens+by-organ+spleen	Fig. S13	(145)
Thymus	Various	https://cells.ucsc.edu/?ds=tabula-sapiens+by-organ+thymus&gene=CMKLR1	Fig. S13	(145)
Liver	Various	https://cells.ucsc.edu/?ds=tabula-sapiens+by-organ+liver&gene=CMKLR1	Fig. S13	(145)
Fat	Various	https://cells.ucsc.edu/?ds=tabula-sapiens+by-organ+fat&gene=CMKLR1	Fig. S13	(145)

Appendix C Supplemental information Chemokine-like receptor 1 targeted positron emission tomography for "Non-invasive assessment of monocyte-derived macrophages in a preclinical model of pulmonary fibrosis"

Appendix C.1 Supplemental Figures

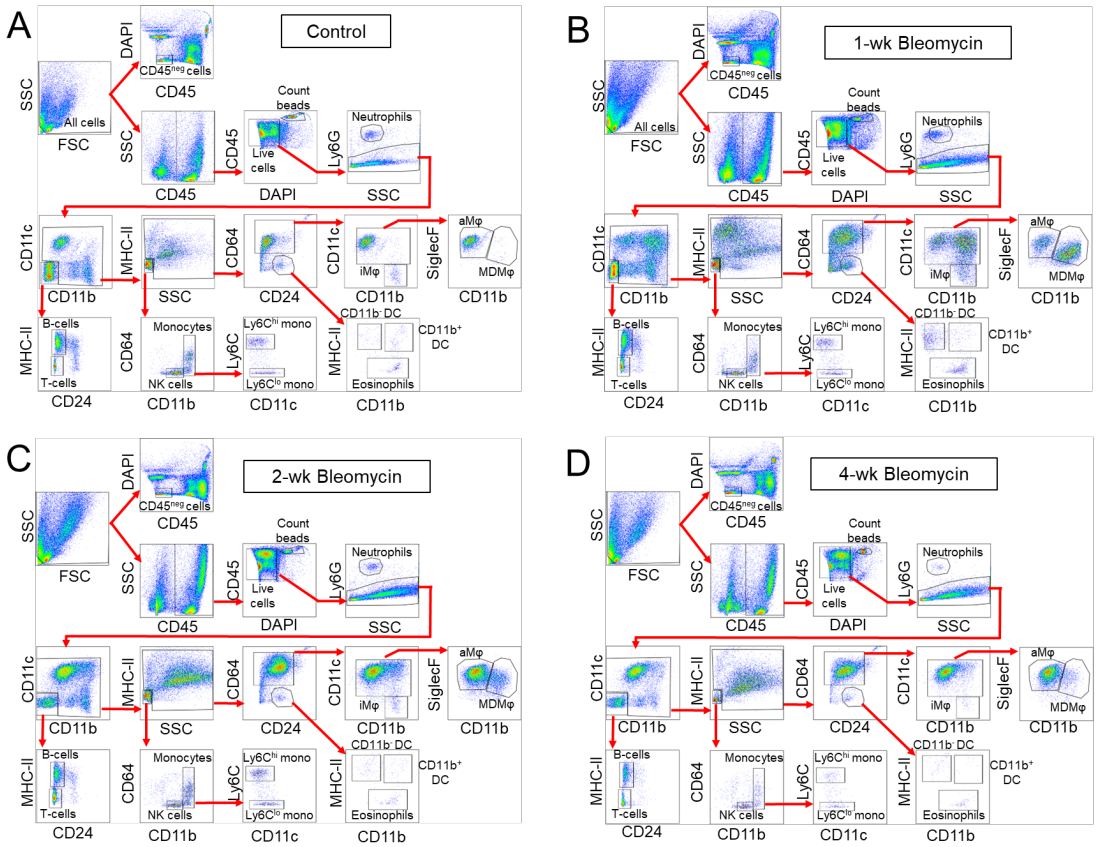

Appendix Figure 38. Gating strategy for flow cytometric analysis of pulmonary immune cell populations.

The gating strategies used to identify the specific leukocyte populations in control (**A**) or bleomycin treated mice at 1 (**B**), 2 (**C**), and 4 (**D**) weeks following intratracheal administration. aMφ: alveolar macrophages; CD11b$^-$ DC: CD11b$^-$ dendritic cells; CD11b$^+$ DC: CD11b$^+$ dendritic cells; iMφ: interstitial macrophages; Ly6C^{hi} mono: LyC6^{hi} monocytes; Ly6C^{lo} mono: Ly6^{lo} monocytes; MDMφ: monocyte-derived macrophages; NK cells: natural killer cells; Neuts: neutrophils.

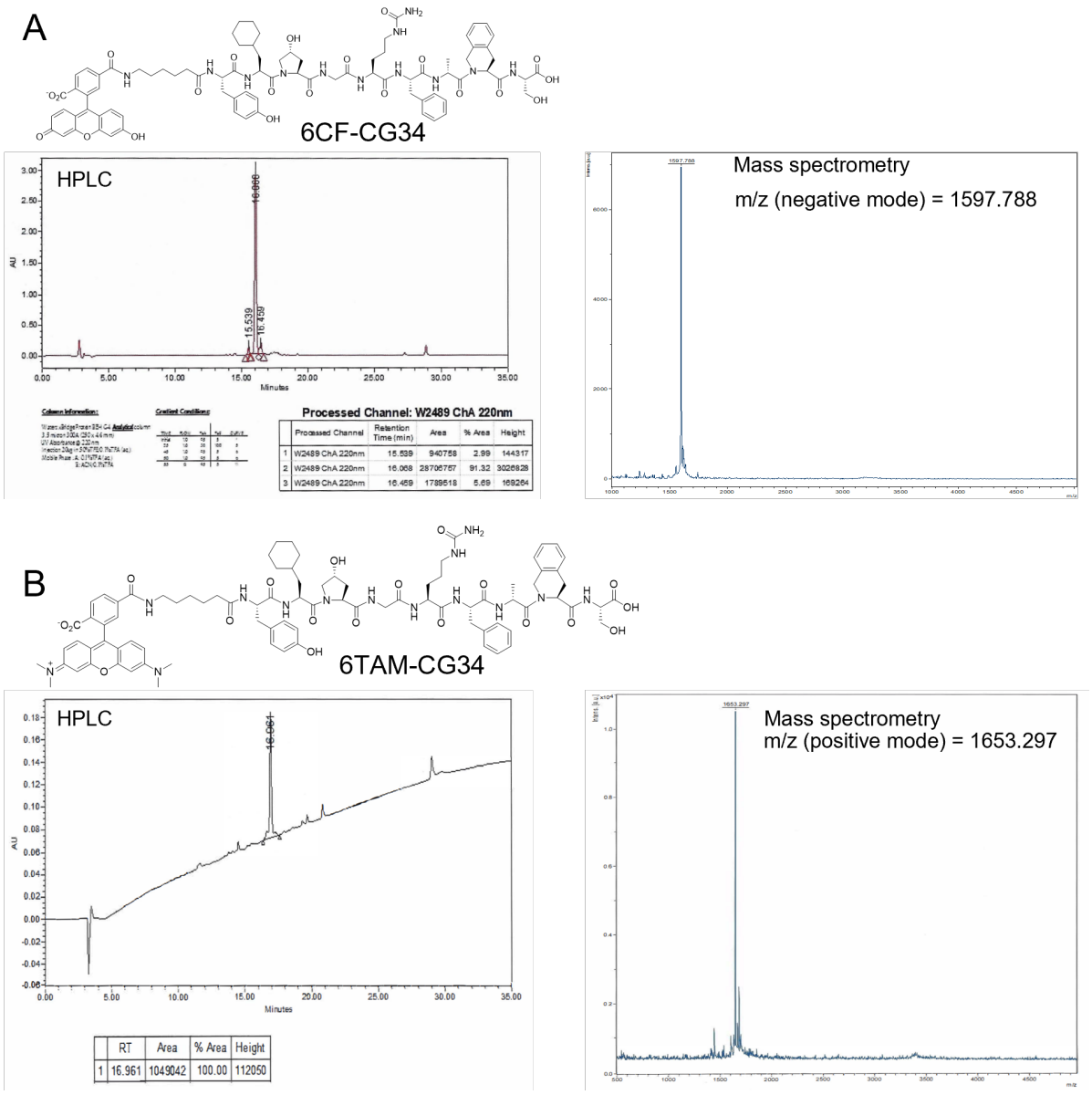

Appendix Figure 39. Characterization of 6CF-CG34 and 6TAM-CG34.

The purity and molecular mass for CG34 fluorescent analogs (**A**) 6CF-CG34 and (**B**) 6TAM-CG34 were confirmed by high-performance liquid chromatography (HPLC) and high-resolution mass spectrometry, respectively. The compounds were synthesized by the University of Pittsburgh Peptide and Peptoid Synthesis Core using the chemistry described in our previous publication (22).

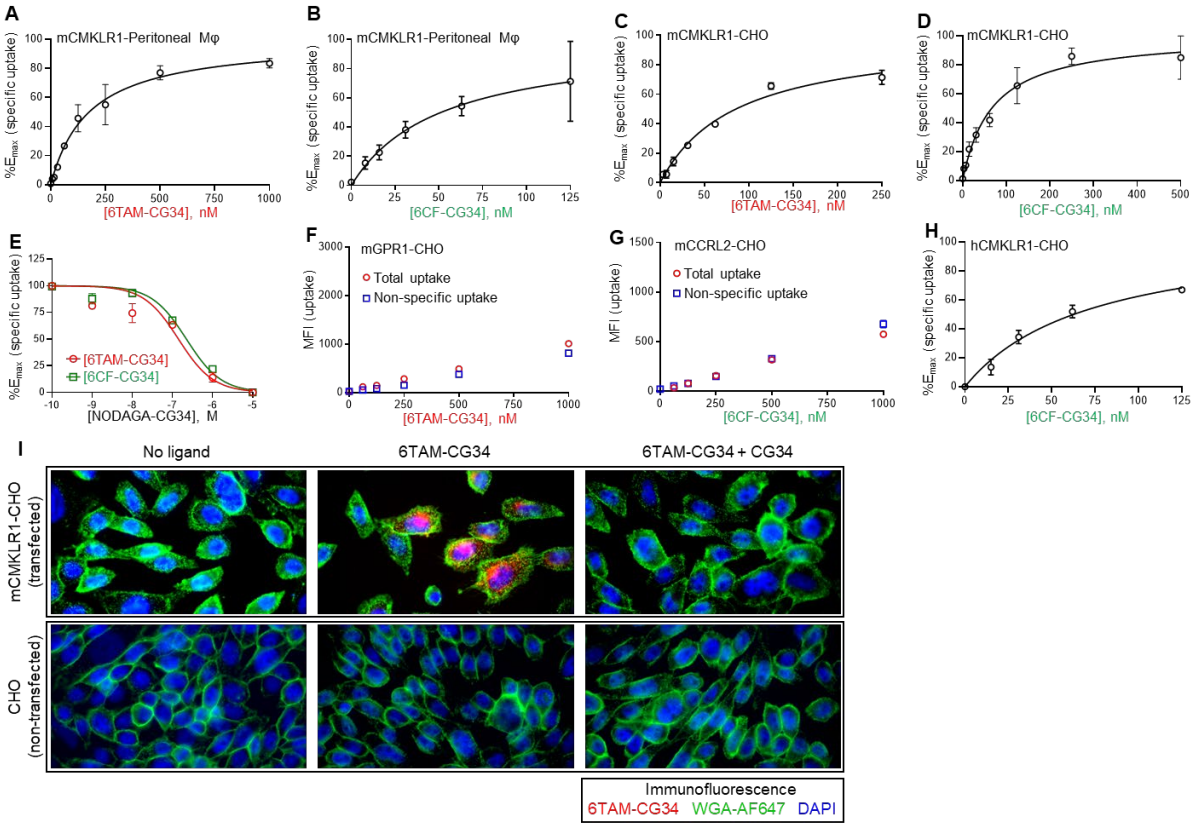

Appendix Figure 40. Pharmacologic potency and selectively of 6CF-CG34 and 6TAM-CG34 for CMKLR1. (**A-D**) Both fluorescent ligands showed comparable binding and uptake to in both mouse CMKLR1$^+$ peritoneal macrophages (22) and CHO cells transiently expressing mCMKLR1. (**E**) NODAGA-CG34 displaces 6CF-CG34 and 6TAM-CG34 in a competitive uptake assay with CMKLR1$^+$ peritoneal macrophages. (**F**, **G**) No significant binding and uptake was observed for fluorescent CG34 analogs to CMKLR1 related receptors GPR1 or CCRL2. (**H**) 6CF-CG34 demonstrates potency at hCMKLR1 to that of mCMKLR1. (**I**) 6TAM-CG34 (250 nM) is internalized by CHO cells transiently expressing mCMKLR1. The specificity of 6TAM-CG34 internalization by mCMKLR1 is confirmed by co-incubation with non-fluorescent CG34 (10 μM). No 6TAM-CG34 is observed in non-transfected CHO cells. The cell membrane was stained with wheat germ agglutinin conjugated to Alexa Fluor 647 (WGA-AF647).

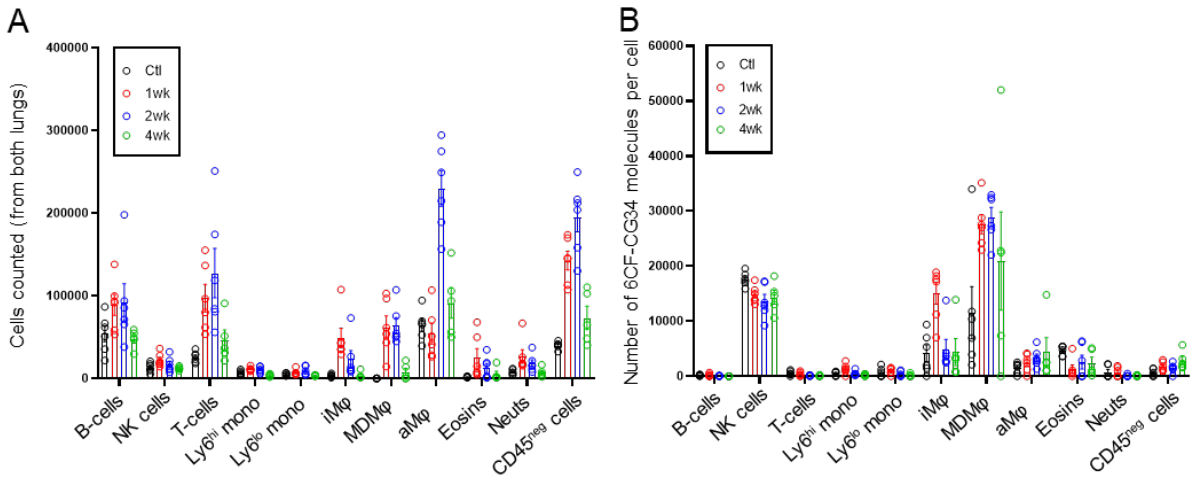

Appendix Figure 41. Flow cytometric quantification of cell count and uptake of 6CF-CG34 by pulmonary leukocyte subset.

Following treatment with either bleomycin or PBS (e.g. control), the (**A**) absolute cell count and (**B**) per cell uptake of 6CF-CG34 for individual cell populations from the lungs was determined with flow cytometry. aMφ: alveolar macrophages; Eosins: eosinophils; iMφ: interstitial macrophages; Ly6C^{hi} mono: LyC6^{hi} monocytes; Ly6C^{lo} mono: Ly6^{lo} monocytes; MDMφ: monocyte-derived macrophages; NK cells: natural killer cells; Neuts: neutrophils. Statistical significance between groups was calculated using a one-way ANOVA with a post-hoc two-tailed Fisher's exact test.

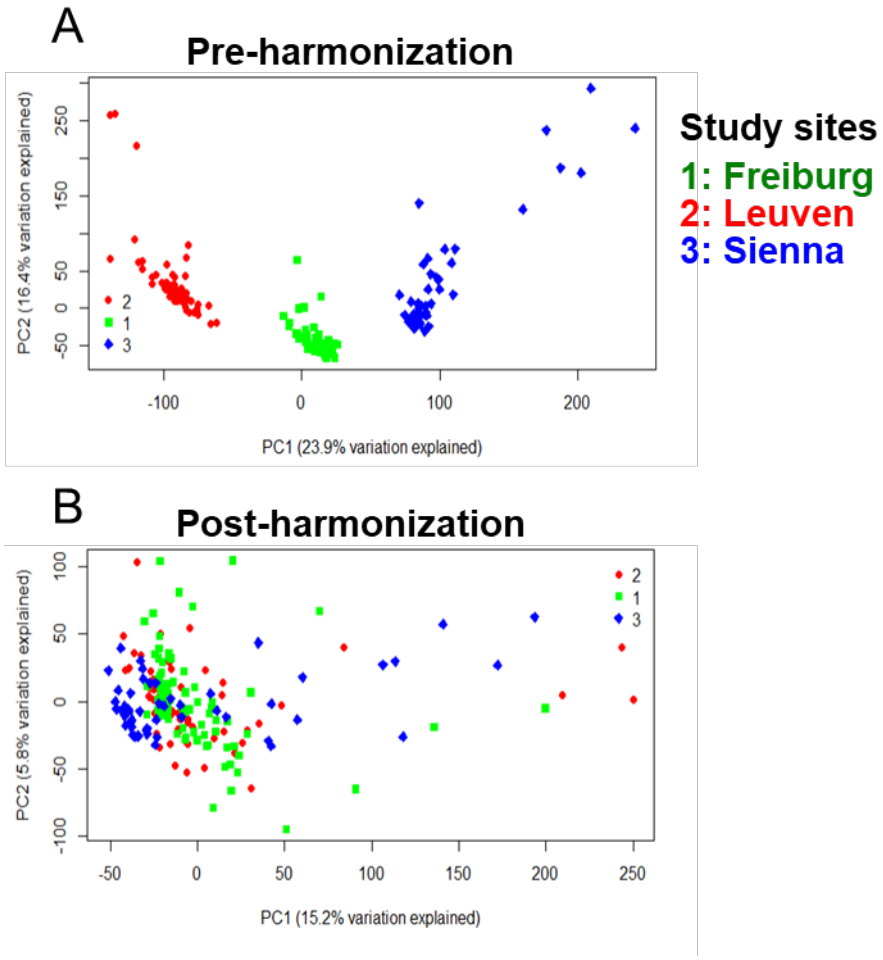

Appendix Figure 42. Harmonization of inter-study site RNA-sequencing data from patients with idiopathic pulmonary.

Analysis of RNA-sequencing data from bronchoalveolar lavage fluid demonstrates inter-site variability (**A**) that was reduced following harmonization (**B**). These data are a reanalysis of a previously published dataset (GEO accession: GSE70867) (196).

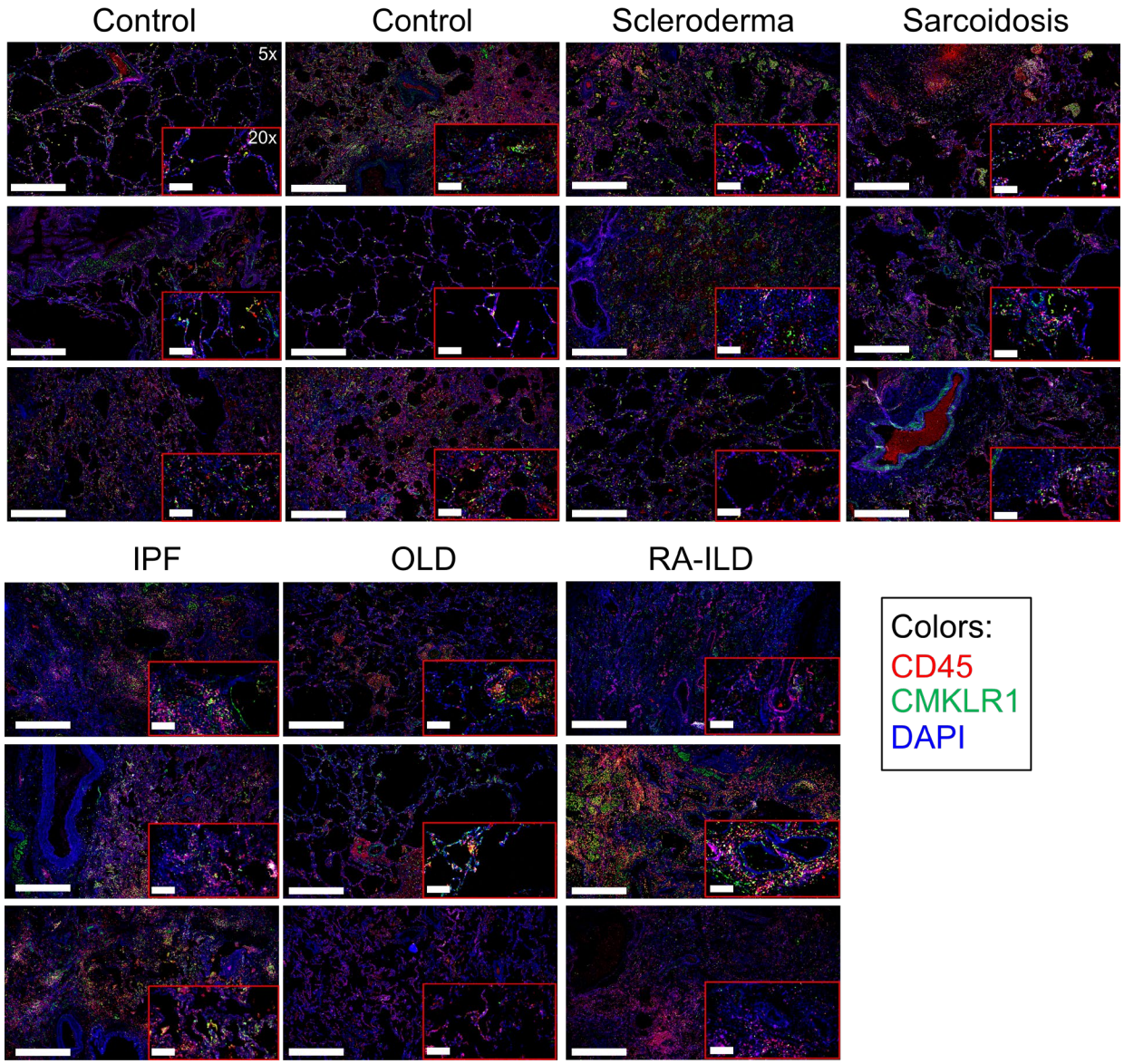

Appendix Figure 43. CMKLR1 expression and its colocalization with CD45 in the lungs of patients with pulmonary fibrosis.

Immunofluorescence imaging to visualize CMKLR1 and CD45 expression in the lungs of deceased donors who had previously been diagnosed with or without (e.g., controls) pulmonary fibrosis. CMKLR1 expression is heterogenous among patients with lung fibrosis and generally colocalizes with CD45 expression. Scale bars: 5x = 800 µm; 20x = 200 µm. Abbreviations: IPF = idiopathic pulmonary fibrosis; OLD = occupational lung disease; RA-ILD = rheumatoid arthritis-associated interstitial lung disease.

Appendix C.2 Supplemental Tables

Supplemental Table 13. List of general reagents.

Reagent	Company	Catalog #
Bleomycin	Sigma	B8416-15UN
C57BL/6 plasma	Innovative	IGMSC57PLAK2E10ML
Cell strainer (70 um)	VWR	10199-656
Clear 96-well plate	Fisher	FB012931
DNase I	Sigma	D4527-10KU
Fetal bovine serum	Gibco	10082147
Geneticin	Fisher	10-131-035
Ham's F-12K Medium	Thermo Fisher	21127022
Hydroxyproline assay kit	Sigma	MAK008-1KT
Hygromycin B	Thermo Fisher	10687010
Lipofectamine 3000	Thermo Fisher	L3000008
Low retention tubes (radiolabeling)	Eppendorf	022431081
PBS	Lonza	17-512F
Penicillin/streptomycin	Gibco	15070-063
Poly-D-lysine	Thermo Fisher	A3890401
Qiagen Plasmid Maxi Kit	Qiagen	12162
RBC Lysis Buffer (10X)	Biolegend	420301
Rodent Intubation Stand	Braintree	RIS 100
RPMI-1640	Gibco	11879-020

Supplemental Table 14. Plasmids for transient transfections.

Plasmid	Company	Catalog
$G_{\alpha 15}$	Sino Biological	HG12687-CF
hCMKLR1	cDNA Resource Center	CMKL100000
mCCRL2	Origene	MG205519
mCMKLR1	Origene	MC208581
mGPR1	Origene	MG205364

Supplemental Table 15. List of reagents used for flow cytometry.

Reagent	Assay	Company	Catalog #
Anti-CD11b-PE	Flow cytometry	BioLegend	101208
Anti-CD11c-PerCP	Flow cytometry	BioLegend	117326
Anti-CD24-AF700	Flow cytometry	BioLegend	101836
Anti-CD45-BV421	Flow cytometry	BioLegend	103134
Anti-CD64-APC	Flow cytometry	BioLegend	139306
Anti-CMKLR1-AF488	Flow cytometry	R&D Biosystems	FAB7610G
Anti-Ly6C-APC-Cy7	Flow cytometry	BioLegend	128026
Anti-Ly6G-BV395	Flow cytometry	BD Biosciences	563978
Anti-MHC-II-BV605	Flow cytometry	BioLegend	107639
Anti-SiglecF-BV510	Flow cytometry	BD Biosciences	740158
DAPI	Flow cytometry	BD Biosciences	564907
IgG_{2B} isotype control-AF488	Flow cytometry	R&D Biosystems	IC013G
Mouse Fc block	Flow cytometry	BD Pharmingen	553141
Precision count beads	Flow cytometry	BioLegend	424902

Supplemental Table 16. List of reagents for immunofluorescent histology.

Antibody	Assay	Company	Catalog #
Anti-rabbit IgG (H+L) - Cy5	Immunofluorescence	Jackson ImmunoResearch	711-175-152
Anti-rat IgG (H+L) - Cy3	Immunofluorescence	Jackson ImmunoResearch	712-165-150
ProLong Gold Antifade Mountant	Immunofluorescence	Thermo Fisher	P36931
Rabbit anti-mouse CMKLR1	Immunofluorescence	LSBio	B12924
Rat anti-mouse F4/80	Immunofluorescence	Thermo Fisher	14-4801-81
Wheat germ agglutinin	Immunofluorescence	Fisher	W32466
Rabbit anti-human CMKLR1	Immunofluorescence	Abcam	ab306554
Mouse anti-mouse CD45	Immunofluorescence	Thermo Fisher	Ma1-19111

Bibliography

1. A. D. T. Force *et al.*, Acute respiratory distress syndrome: the Berlin Definition. *JAMA* **307**, 2526-2533 (2012).
2. O.-Y. Cheung, P. Graziano, M. L. Smith, "6 - Acute Lung Injury" in Practical Pulmonary Pathology: A Diagnostic Approach (Third Edition), K. O. Leslie, M. R. Wick, Eds. (Elsevier, 2018), https://doi.org/10.1016/B978-0-323-44284-8.00006-5, pp. 125-146.e123.
3. M. A. Matthay *et al.*, Acute respiratory distress syndrome. *Nat Rev Dis Primers* **5**, 18 (2019).
4. R. Blondonnet, J. M. Constantin, V. Sapin, M. Jabaudon, A Pathophysiologic Approach to Biomarkers in Acute Respiratory Distress Syndrome. *Dis Markers* **2016**, 3501373 (2016).
5. M. Wijsenbeek, V. Cottin, Spectrum of Fibrotic Lung Diseases. *N Engl J Med* **383**, 958-968 (2020).
6. M. S. Wilson, T. A. Wynn, Pulmonary fibrosis: pathogenesis, etiology and regulation. *Mucosal Immunol* **2**, 103-121 (2009).
7. K. Shenderov, S. L. Collins, J. D. Powell, M. R. Horton, Immune dysregulation as a driver of idiopathic pulmonary fibrosis. *The Journal of clinical investigation* **131** (2021).
8. B. D. Bringardner, C. P. Baran, T. D. Eubank, C. B. Marsh, The role of inflammation in the pathogenesis of idiopathic pulmonary fibrosis. *Antioxid Redox Signal* **10**, 287-301 (2008).
9. P. Heukels, C. C. Moor, J. H. von der Thusen, M. S. Wijsenbeek, M. Kool, Inflammation and immunity in IPF pathogenesis and treatment. *Respir Med* **147**, 79-91 (2019).

10. B. Ley, H. R. Collard, T. E. King, Jr., Clinical course and prediction of survival in idiopathic pulmonary fibrosis. *Am J Respir Crit Care Med* **183**, 431-440 (2011).

11. V. Cottin *et al.*, Presentation, diagnosis and clinical course of the spectrum of progressive-fibrosing interstitial lung diseases. *Eur Respir Rev* **27** (2018).

12. T. E. King, Jr. *et al.*, A phase 3 trial of pirfenidone in patients with idiopathic pulmonary fibrosis. *N Engl J Med* **370**, 2083-2092 (2014).

13. K. R. Flaherty *et al.*, Nintedanib in Progressive Fibrosing Interstitial Lung Diseases. *N Engl J Med* **381**, 1718-1727 (2019).

14. W. S. Bowman, G. A. Echt, J. M. Oldham, Biomarkers in Progressive Fibrosing Interstitial Lung Disease: Optimizing Diagnosis, Prognosis, and Treatment Response. *Front Med (Lausanne)* **8**, 680997 (2021).

15. A. M. Hoffmann-Vold *et al.*, Endotype-phenotyping may predict a treatment response in progressive fibrosing interstitial lung disease. *EBioMedicine* **50**, 379-386 (2019).

16. I. Gantz *et al.*, Molecular cloning of a novel receptor (CMKLR1) with homology to the chemotactic factor receptors. *Cytogenet Cell Genet* **74**, 286-290 (1996).

17. M. Samson *et al.*, ChemR23, a putative chemoattractant receptor, is expressed in monocyte-derived dendritic cells and macrophages and is a coreceptor for SIV and some primary HIV-1 strains. *Eur J Immunol* **28**, 1689-1700 (1998).

18. A. J. Kennedy, A. P. Davenport, International Union of Basic and Clinical Pharmacology CIII: Chemerin Receptors CMKLR1 (Chemerin(1)) and GPR1 (Chemerin(2)) Nomenclature, Pharmacology, and Function. *Pharmacol Rev* **70**, 174-196 (2018).

19. V. Wittamer *et al.*, Specific recruitment of antigen-presenting cells by chemerin, a novel processed ligand from human inflammatory fluids. *J Exp Med* **198**, 977-985 (2003).

20. W. Meder *et al.*, Characterization of human circulating TIG2 as a ligand for the orphan receptor ChemR23. *FEBS Lett* **555**, 495-499 (2003).

21. S. Luangsay *et al.*, Mouse ChemR23 is expressed in dendritic cell subsets and macrophages, and mediates an anti-inflammatory activity of chemerin in a lung disease model. *J Immunol* **183**, 6489-6499 (2009).

22. P. Z. Mannes *et al.*, Molecular imaging of chemokine-like receptor 1 (CMKLR1) in experimental acute lung injury. *Proc Natl Acad Sci U S A* **120**, e2216458120 (2023).

23. W. Vermi *et al.*, Role of ChemR23 in directing the migration of myeloid and plasmacytoid dendritic cells to lymphoid organs and inflamed skin. *J Exp Med* **201**, 509-515 (2005).

24. K. B. Goralski *et al.*, Chemerin, a novel adipokine that regulates adipogenesis and adipocyte metabolism. *J Biol Chem* **282**, 28175-28188 (2007).

25. A. Del Prete, R. Bonecchi, A. Vecchi, A. Mantovani, S. Sozzani, CCRL2, a fringe member of the atypical chemoattractant receptor family. *Eur J Immunol* **43**, 1418-1422 (2013).

26. B. A. Zabel *et al.*, Chemerin activation by serine proteases of the coagulation, fibrinolytic, and inflammatory cascades. *J Biol Chem* **280**, 34661-34666 (2005).

27. B. A. Zabel *et al.*, Chemerin regulation and role in host defense. *Am J Clin Exp Immunol* **3**, 1-19 (2014).

28. L. Zhao *et al.*, Chemerin 156F, generated by chymase cleavage of prochemerin, is elevated in joint fluids of arthritis patients. *Arthritis Res Ther* **20**, 132 (2018).

29. M. C. Ernst, C. J. Sinal, Chemerin: at the crossroads of inflammation and obesity. *Trends in Endocrinology & Metabolism* **21**, 660-667 (2010).

30. V. Wittamer *et al.*, The C-terminal nonapeptide of mature chemerin activates the chemerin receptor with low nanomolar potency. *J Biol Chem* **279**, 9956-9962 (2004).

31. S. Erdmann *et al.*, CMKLR1-targeting peptide tracers for PET/MR imaging of breast cancer. *Theranostics* **9**, 6719-6733 (2019).

32. J. R. Doyle *et al.*, Development of a membrane-anchored chemerin receptor agonist as a novel modulator of allergic airway inflammation and neuropathic pain. *J Biol Chem* **289**, 13385-13396 (2014).

33. J. Wang *et al.*, Cryo-EM structure of the human chemerin receptor 1-Gi protein complex bound to the C-terminal nonapeptide of chemerin. *Proc Natl Acad Sci U S A* **120**, e2214324120 (2023).

34. K. Shimamura *et al.*, Identification of a stable chemerin analog with potent activity toward ChemR23. *Peptides* **30**, 1529-1538 (2009).

35. O. De Henau *et al.*, Signaling Properties of Chemerin Receptors CMKLR1, GPR1 and CCRL2. *PLoS One* **11**, e0164179 (2016).

36. A. J. Kennedy *et al.*, Chemerin Elicits Potent Constrictor Actions via Chemokine-Like Receptor 1 (CMKLR1), not G-Protein-Coupled Receptor 1 (GPR1), in Human and Rat Vasculature. *J Am Heart Assoc* **5** (2016).

37. B. Bondue *et al.*, ChemR23 dampens lung inflammation and enhances anti-viral immunity in a mouse model of acute viral pneumonia. *PLoS Pathog* **7**, e1002358 (2011).

38. T. Demoor *et al.*, The role of ChemR23 in the induction and resolution of cigarette smoke-induced inflammation. *J Immunol* **186**, 5457-5467 (2011).

39. S. Provoost *et al.*, Pro- and Anti-Inflammatory Role of ChemR23 Signaling in Pollutant-Induced Inflammatory Lung Responses. *J Immunol* **196**, 1882-1890 (2016).

40. C. Albanesi *et al.*, Chemerin expression marks early psoriatic skin lesions and correlates with plasmacytoid dendritic cell recruitment. *J Exp Med* **206**, 249-258 (2009).

41. J. Skrzeczynska-Moncznik *et al.*, Potential role of chemerin in recruitment of plasmacytoid dendritic cells to diseased skin. *Biochem Biophys Res Commun* **380**, 323-327 (2009).

42. Y. Xie *et al.*, Chemerin/CMKLR1 Axis Promotes Inflammation and Pyroptosis by Activating NLRP3 Inflammasome in Diabetic Cardiomyopathy Rat. *Front Physiol* **11**, 381 (2020).

43. C. Wang *et al.*, Chemokine-like receptor 1 deficiency impedes macrophage phenotypic transformation and cardiac repair after myocardial infarction. *Int J Cardiol* **372**, 6-14 (2023).

44. E. Dander *et al.*, The chemerin/CMKLR1 axis regulates intestinal graft-versus-host disease. *JCI Insight* **8** (2023).

45. C. Trilleaud *et al.*, Agonist anti-ChemR23 mAb reduces tissue neutrophil accumulation and triggers chronic inflammation resolution. *Sci Adv* **7** (2021).

46. L. Vass *et al.*, Advances in PET to assess pulmonary inflammation: A systematic review. *Eur J Radiol* **130**, 109182 (2020).

47. D. L. Chen *et al.*, [18F]fluorodeoxyglucose positron emission tomography for lung antiinflammatory response evaluation. *Am J Respir Crit Care Med* **180**, 533-539 (2009).

48. D. L. Chen, D. B. Rosenbluth, M. A. Mintun, D. P. Schuster, FDG-PET imaging of pulmonary inflammation in healthy volunteers after airway instillation of endotoxin. *J Appl Physiol (1985)* **100**, 1602-1609 (2006).

49. D. L. Chen, D. P. Schuster, Positron emission tomography with [18F]fluorodeoxyglucose to evaluate neutrophil kinetics during acute lung injury. *Am J Physiol Lung Cell Mol Physiol* **286**, L834-840 (2004).

50. L. W. Locke *et al.*, A novel neutrophil-specific PET imaging agent: cFLFLFK-PEG-64Cu. *J Nucl Med* **50**, 790-797 (2009).

51. N. Kondo *et al.*, Development of matrix metalloproteinase-targeted probes for lung inflammation detection with positron emission tomography. *Sci Rep* **8**, 1347 (2018).

52. E. Puuvuori *et al.*, PET Imaging of Neutrophil Elastase with (11)C-GW457427 in Acute Respiratory Distress Syndrome in Pigs. *J Nucl Med* **64**, 423-429 (2023).

53. Y. Liu *et al.*, PET-based Imaging of Chemokine Receptor 2 in Experimental and Disease-related Lung Inflammation. *Radiology* **283**, 758-768 (2017).

54. H. J. Huang *et al.*, Imaging pulmonary inducible nitric oxide synthase expression with PET. *J Nucl Med* **56**, 76-81 (2015).

55. W. Han *et al.*, Molecular imaging of folate receptor beta-positive macrophages during acute lung inflammation. *Am J Respir Cell Mol Biol* **53**, 50-59 (2015).

56. S. L. Brody *et al.*, Chemokine Receptor 2-targeted Molecular Imaging in Pulmonary Fibrosis. A Clinical Trial. *Am J Respir Crit Care Med* **203**, 78-89 (2021).

57. J. Schniering *et al.*, (18)F-AzaFol for Detection of Folate Receptor-beta Positive Macrophages in Experimental Interstitial Lung Disease-A Proof-of-Concept Study. *Front Immunol* **10**, 2724 (2019).

58. P. Desogere *et al.*, Type I collagen-targeted PET probe for pulmonary fibrosis detection and staging in preclinical models. *Sci Transl Med* **9** (2017).

59. P. Desogere *et al.*, Optimization of a Collagen-Targeted PET Probe for Molecular Imaging of Pulmonary Fibrosis. *J Nucl Med* **58**, 1991-1996 (2017).

60. S. B. Montesi *et al.*, Type I Collagen-targeted Positron Emission Tomography Imaging in Idiopathic Pulmonary Fibrosis: First-in-Human Studies. *Am J Respir Crit Care Med* **200**, 258-261 (2019).

61. J. Wahsner *et al.*, (68)Ga-NODAGA-Indole: An Allysine-Reactive Positron Emission Tomography Probe for Molecular Imaging of Pulmonary Fibrogenesis. *J Am Chem Soc* **141**, 5593-5596 (2019).

62. P. Z. Mannes *et al.*, 2-deoxy-2-[(18)F]fluoro-D-glucose Positron Emission Tomography to Monitor Lung Inflammation and Therapeutic Response to Dexamethasone in a Murine Model of Acute Lung Injury. *Mol Imaging Biol* 10.1007/s11307-023-01813-w, 1-11 (2023).

63. T. Pham, G. D. Rubenfeld, Fifty Years of Research in ARDS. The Epidemiology of Acute Respiratory Distress Syndrome. A 50th Birthday Review. *Am J Respir Crit Care Med* **195**, 860-870 (2017).

64. K. W. Hendrickson, I. D. Peltan, S. M. Brown, The Epidemiology of Acute Respiratory Distress Syndrome Before and After Coronavirus Disease 2019. *Critical care clinics* **37**, 703-716 (2021).

65. G. Musch *et al.*, Regional gas exchange and cellular metabolic activity in ventilator-induced lung injury. *Anesthesiology* **106**, 723-735 (2007).

66. T. J. Barreiro, I. Perillo, An approach to interpreting spirometry. *Am Fam Physician* **69**, 1107-1114 (2004).

67. E. K. Pauwels, V. R. McCready, J. H. Stoot, D. F. van Deurzen, The mechanism of accumulation of tumour-localising radiopharmaceuticals. *Eur J Nucl Med* **25**, 277-305 (1998).

68. B. M. Gallagher *et al.*, Metabolic trapping as a principle of oradiopharmaceutical design: some factors resposible for the biodistribution of [18F] 2-deoxy-2-fluoro-D-glucose. *J Nucl Med* **19**, 1154-1161 (1978).

69. J. R. Barrio *et al.*, Does 2-FDG PET Accurately Reflect Quantitative In Vivo Glucose Utilization? *J Nucl Med* **61**, 931-937 (2020).

70. M. Graebe *et al.*, Molecular pathology in vulnerable carotid plaques: correlation with [18]-fluorodeoxyglucose positron emission tomography (FDG-PET). *European journal of vascular and endovascular surgery : the official journal of the European Society for Vascular Surgery* **37**, 714-721 (2009).

71. L. A. O'Neill, R. J. Kishton, J. Rathmell, A guide to immunometabolism for immunologists. *Nat Rev Immunol* **16**, 553-565 (2016).

72. N. de Prost, M. R. Tucci, M. F. Melo, Assessment of lung inflammation with 18F-FDG PET during acute lung injury. *AJR Am J Roentgenol* **195**, 292-300 (2010).

73. S. Capitanio, A. J. Nordin, A. R. Noraini, C. Rossetti, PET/CT in nononcological lung diseases: current applications and future perspectives. *Eur Respir Rev* **25**, 247-258 (2016).

74. D. R. Subramanian *et al.*, Assessment of pulmonary neutrophilic inflammation in emphysema by quantitative positron emission tomography. *Am J Respir Crit Care Med* **186**, 1125-1132 (2012).

75. D. A. Torigian *et al.*, In vivo quantification of pulmonary inflammation in relation to emphysema severity via partial volume corrected (18)F-FDG-PET using computer-assisted analysis of diagnostic chest CT. *Hell J Nucl Med* **16**, 12-18 (2013).

76. H. A. Jones, P. S. Marino, B. H. Shakur, N. W. Morrell, In vivo assessment of lung inflammatory cell activity in patients with COPD and asthma. *Eur Respir J* **21**, 567-573 (2003).

77. H. Y. Yoon, S. H. Lee, S. Ha, J. S. Ryu, J. W. Song, The Value of (18)F-FDG PET/CT in Evaluating Disease Severity and Prognosis in Idiopathic Pulmonary Fibrosis Patients. *J Korean Med Sci* **36**, e257 (2021).

78. D. L. Chen *et al.*, Quantifying pulmonary inflammation in cystic fibrosis with positron emission tomography. *Am J Respir Crit Care Med* **173**, 1363-1369 (2006).

79. T. Ishii *et al.*, Neutrophil elastase contributes to acute lung injury induced by bilateral nephrectomy. *Am J Pathol* **177**, 1665-1673 (2010).

80. Y. Zhao *et al.*, Thrombospondin-1 restrains neutrophil granule serine protease function and regulates the innate immune response during Klebsiella pneumoniae infection. *Mucosal Immunol* **8**, 896-905 (2015).

81. T. TeSlaa, M. A. Teitell, Techniques to monitor glycolysis. *Methods Enzymol* **542**, 91-114 (2014).

82. D. Jelinek *et al.*, Mapping Metabolism: Monitoring Lactate Dehydrogenase Activity Directly in Tissue. *J Vis Exp* 10.3791/57760 (2018).

83. M. A. Lokuta, G. H. Mehring, D. M. Paulnock, Spectrophotometric determination of oxidative metabolism. *Biotechniques* **22**, 841-844 (1997).

84. D. L. Chen *et al.*, Consensus Recommendations on the Use of (18)F-FDG PET/CT in Lung Disease. *J Nucl Med* **61**, 1701-1707 (2020).

85. D. L. Chen *et al.*, Quantification of Lung PET Images: Challenges and Opportunities. *J Nucl Med* **58**, 201-207 (2017).

86. M. Soret, S. L. Bacharach, I. Buvat, Partial-volume effect in PET tumor imaging. *J Nucl Med* **48**, 932-945 (2007).

87. L. M. Carter *et al.*, The Impact of Positron Range on PET Resolution, Evaluated with Phantoms and PHITS Monte Carlo Simulations for Conventional and Non-conventional Radionuclides. *Mol Imaging Biol* **22**, 73-84 (2020).

88. H. S. Kulkarni *et al.*, Update on the Features and Measurements of Experimental Acute Lung Injury in Animals: An Official American Thoracic Society Workshop Report. *Am J Respir Cell Mol Biol* **66**, e1-e14 (2022).

89. L. D. Bos *et al.*, Identification and validation of distinct biological phenotypes in patients with acute respiratory distress syndrome by cluster analysis. *Thorax* **72**, 876-883 (2017).

90. K. R. Famous *et al.*, Acute Respiratory Distress Syndrome Subphenotypes Respond Differently to Randomized Fluid Management Strategy. *Am J Respir Crit Care Med* **195**, 331-338 (2017).

91. J. P. Reilly, C. S. Calfee, J. D. Christie, Acute Respiratory Distress Syndrome Phenotypes. *Semin Respir Crit Care Med* **40**, 19-30 (2019).

92. A. E. Williams, R. C. Chambers, The mercurial nature of neutrophils: still an enigma in ARDS? *Am J Physiol Lung Cell Mol Physiol* **306**, L217-230 (2014).

93. Y. Qu *et al.*, Thrombospondin-1 protects against pathogen-induced lung injury by limiting extracellular matrix proteolysis. *JCI Insight* **3** (2018).

94. J. C. Rodriguez-Prados *et al.*, Substrate fate in activated macrophages: a comparison between innate, classic, and alternative activation. *J Immunol* **185**, 605-614 (2010).

95. N. Borregaard, T. Herlin, Energy metabolism of human neutrophils during phagocytosis. *The Journal of clinical investigation* **70**, 550-557 (1982).

96. P. Sadiku *et al.*, Neutrophils Fuel Effective Immune Responses through Gluconeogenesis and Glycogenesis. *Cell Metab* **33**, 411-423 e414 (2021).

97. B. Kelly, L. A. O'Neill, Metabolic reprogramming in macrophages and dendritic cells in innate immunity. *Cell Res* **25**, 771-784 (2015).

98. G. M. Tannahill *et al.*, Succinate is an inflammatory signal that induces IL-1beta through HIF-1alpha. *Nature* **496**, 238-242 (2013).

99. J. P. Beca, J. W. Scopes, Serial determinations of blood lactate in respiratory distress syndrome. *Arch Dis Child* **47**, 550-557 (1972).

100. H. Zhang *et al.*, Risk stratification of patients with acute respiratory distress syndrome complicated with sepsis using lactate trajectories. *BMC Pulm Med* **22**, 339 (2022).

101. C. Wu *et al.*, Risk Factors Associated With Acute Respiratory Distress Syndrome and Death in Patients With Coronavirus Disease 2019 Pneumonia in Wuhan, China. *JAMA Intern Med* **180**, 934-943 (2020).

102. H. Sipahioglu, S. Onuk, Lactate dehydrogenase/albumin ratio as a prognostic factor in severe acute respiratory distress syndrome cases associated with COVID-19. *Medicine (Baltimore)* **101**, e30759 (2022).

103. N. Alipanah-Lechner *et al.*, Plasma metabolic profiling implicates dysregulated lipid metabolism and glycolytic shift in hyperinflammatory ARDS. *Am J Physiol Lung Cell Mol Physiol* 10.1152/ajplung.00278.2022 (2023).

104. A. F. Santos, P. Povoa, P. Paixao, A. Mendonca, L. Taborda-Barata, Changes in Glycolytic Pathway in SARS-COV 2 Infection and Their Importance in Understanding the Severity of COVID-19. *Front Chem* **9**, 685196 (2021).

105. M. Pourfathi *et al.*, Lung Metabolism and Inflammation during Mechanical Ventilation; An Imaging Approach. *Sci Rep* **8**, 3525 (2018).

106. M. J. Robinson, A. D. Krasnodembskaya, Therapeutic targeting of metabolic alterations in acute respiratory distress syndrome. *Eur Respir Rev* **29** (2020).

107. E. Ledoult *et al.*, (18)F-FDG positron emission tomography scanning in systemic sclerosis-associated interstitial lung disease: a pilot study. *Arthritis Res Ther* **23**, 76 (2021).

108. E. Puuvuori *et al.*, PET-CT imaging of pulmonary inflammation using [(68)Ga]Ga-DOTA-TATE. *EJNMMI Res* **12**, 19 (2022).

109. J. D. Steinberg, W. Vogel, E. Vegt, Factors influencing brown fat activation in FDG PET/CT: a retrospective analysis of 15,000+ cases. *Br J Radiol* **90**, 20170093 (2017).

110. N. M. Long, C. S. Smith, Causes and imaging features of false positives and false negatives on F-PET/CT in oncologic imaging. *Insights Imaging* **2**, 679-698 (2011).

111. J. W. Keyes, Jr., SUV: standard uptake or silly useless value? *J Nucl Med* **36**, 1836-1839 (1995).

112. G. J. Weiss, R. L. Korn, Interpretation of PET scans: do not take SUVs at face value. *J Thorac Oncol* **7**, 1744-1746 (2012).

113. M. Blau, Letter: Radiation dosimetry of 131-I-19-iodocholesterol: The pitfalls of using tissue concentration data. *J Nucl Med* **16**, 247-249 (1975).

114. M. C. Adams, T. G. Turkington, J. M. Wilson, T. Z. Wong, A systematic review of the factors affecting accuracy of SUV measurements. *AJR Am J Roentgenol* **195**, 310-320 (2010).

115. V. Zambelli *et al.*, Time course of metabolic activity and cellular infiltration in a murine model of acid-induced lung injury. *Intensive care medicine* **38**, 694-701 (2012).

116. R. Kubota *et al.*, Intratumoral distribution of fluorine-18-fluorodeoxyglucose in vivo: high accumulation in macrophages and granulation tissues studied by microautoradiography. *J Nucl Med* **33**, 1972-1980 (1992).

117. J. Haddad *et al.*, Molecular Imaging of Very Late Antigen-4 in Acute Lung Injury. *J Nucl Med* **62**, 280-286 (2021).

118. Q. Cao, Q. Huang, C. Mohan, C. Li, Small-Animal PET/CT Imaging of Local and Systemic Immune Response Using (64)Cu-alphaCD11b. *J Nucl Med* **60**, 1317-1324 (2019).

119. M. J. Hardwick, M. K. Chen, K. Baidoo, M. G. Pomper, T. R. Guilarte, In vivo imaging of peripheral benzodiazepine receptors in mouse lungs: a biomarker of inflammation. *Mol Imaging* **4**, 432-438 (2005).

120. G. Antoni *et al.*, In Vivo Visualization and Quantification of Neutrophil Elastase in Lungs of COVID-19 Patients: A First-in-Humans PET Study with (11)C-NES. *J Nucl Med* **64**, 145-148 (2023).

121. J. Villar, J. Blanco, R. M. Kacmarek, Current incidence and outcome of the acute respiratory distress syndrome. *Curr Opin Crit Care* **22**, 1-6 (2016).

122. C. A. Pfortmueller, T. Spinetti, R. D. Urman, M. M. Luedi, J. C. Schefold, COVID-19-associated acute respiratory distress syndrome (CARDS): Current knowledge on pathophysiology and ICU treatment - A narrative review. *Best Pract Res Clin Anaesthesiol* **35**, 351-368 (2021).

123. B. T. Thompson, R. C. Chambers, K. D. Liu, Acute Respiratory Distress Syndrome. *N Engl J Med* **377**, 562-572 (2017).

124. G. D. Rubenfeld *et al.*, Incidence and outcomes of acute lung injury. *N Engl J Med* **353**, 1685-1693 (2005).

125. J. R. Beitler *et al.*, Advancing precision medicine for acute respiratory distress syndrome. *Lancet Respir Med* **10**, 107-120 (2022).

126. C. S. Calfee *et al.*, Subphenotypes in acute respiratory distress syndrome: latent class analysis of data from two randomised controlled trials. *Lancet Respir Med* **2**, 611-620 (2014).

127. R. M. Schnabel *et al.*, Clinical course and complications following diagnostic bronchoalveolar lavage in critically ill mechanically ventilated patients. *BMC Pulm Med* **15**, 107 (2015).

128. M. I. Garcia-Laorden, J. A. Lorente, C. Flores, A. S. Slutsky, J. Villar, Biomarkers for the acute respiratory distress syndrome: how to make the diagnosis more precise. *Ann Transl Med* **5**, 283 (2017).

129. M. Pourfathi, S. J. Kadlecek, S. Chatterjee, R. R. Rizi, Metabolic Imaging and Biological Assessment: Platforms to Evaluate Acute Lung Injury and Inflammation. *Front Physiol* **11**, 937 (2020).

130. P. Z. Mannes, S. Tavakoli, Imaging Immunometabolism in Atherosclerosis. *J Nucl Med* **62**, 896-902 (2021).

131. L. D. J. Bos *et al.*, Precision medicine in acute respiratory distress syndrome: workshop report and recommendations for future research. *Eur Respir Rev* **30** (2021).

132. L. Fantuzzi *et al.*, Loss of CCR2 expression and functional response to monocyte chemotactic protein (MCP-1) during the differentiation of human monocytes: role of secreted MCP-1 in the regulation of the chemotactic response. *Blood* **94**, 875-883 (1999).

133. R. J. Phillips, M. Lutz, B. Premack, Differential signaling mechanisms regulate expression of CC chemokine receptor-2 during monocyte maturation. *J Inflamm (Lond)* **2**, 14 (2005).

134. E. P. C. van der Vorst *et al.*, Hematopoietic ChemR23 (Chemerin Receptor 23) Fuels Atherosclerosis by Sustaining an M1 Macrophage-Phenotype and Guidance of Plasmacytoid Dendritic Cells to Murine Lesions-Brief Report. *Arterioscler Thromb Vasc Biol* **39**, 685-693 (2019).

135. S. Zylla *et al.*, Association of Circulating Chemerin With Subclinical Parameters of Atherosclerosis: Results of a Population-Based Study. *Arterioscler Thromb Vasc Biol* **38**, 1656-1664 (2018).

136. K. Kaneko *et al.*, Chemerin activates fibroblast-like synoviocytes in patients with rheumatoid arthritis. *Arthritis Res Ther* **13**, R158 (2011).

137. D. Wendisch *et al.*, SARS-CoV-2 infection triggers profibrotic macrophage responses and lung fibrosis. *Cell* **184**, 6243-6261 e6227 (2021).

138. J. C. Melms *et al.*, A molecular single-cell lung atlas of lethal COVID-19. *Nature* **595**, 114-119 (2021).

139. S. Tavakoli *et al.*, Differential Regulation of Macrophage Glucose Metabolism by Macrophage Colony-stimulating Factor and Granulocyte-Macrophage Colony-stimulating Factor: Implications for (18)F FDG PET Imaging of Vessel Wall Inflammation. *Radiology* **283**, 87-97 (2017).

140. Y. Hao *et al.*, Integrated analysis of multimodal single-cell data. *Cell* **184**, 3573-3587 e3529 (2021).

141. M. Liao *et al.*, Single-cell landscape of bronchoalveolar immune cells in patients with COVID-19. *Nat Med* **26**, 842-844 (2020).

142. R. L. Chua *et al.*, COVID-19 severity correlates with airway epithelium-immune cell interactions identified by single-cell analysis. *Nat Biotechnol* **38**, 970-979 (2020).

143. X. Li *et al.*, ScRNA-seq expression of IFI27 and APOC2 identifies four alveolar macrophage superclusters in healthy BALF. *Life Sci Alliance* **5** (2022).

144. M. L. Speir *et al.*, UCSC Cell Browser: Visualize Your Single-Cell Data. *Bioinformatics* 10.1093/bioinformatics/btab503 (2021).

145. C. Tabula Sapiens *et al.*, The Tabula Sapiens: A multiple-organ, single-cell transcriptomic atlas of humans. *Science* **376**, eabl4896 (2022).

146. J. X. Zhou *et al.*, Chemerin C9 peptide induces receptor internalization through a clathrin-independent pathway. *Acta Pharmacol Sin* **35**, 653-663 (2014).

147. J. M. Opalek, N. A. Ali, J. M. Lobb, M. G. Hunter, C. B. Marsh, Alveolar macrophages lack CCR2 expression and do not migrate to CCL2. *J Inflamm (Lond)* **4**, 19 (2007).

148. Y. R. Yu *et al.*, A Protocol for the Comprehensive Flow Cytometric Analysis of Immune Cells in Normal and Inflamed Murine Non-Lymphoid Tissues. *PLoS One* **11**, e0150606 (2016).

149. M. E. Kuruvilla, F. E. Lee, G. B. Lee, Understanding Asthma Phenotypes, Endotypes, and Mechanisms of Disease. *Clin Rev Allergy Immunol* **56**, 219-233 (2019).

150. P. J. Barnes, Inflammatory endotypes in COPD. *Allergy* **74**, 1249-1256 (2019).

151. M. Ackermann *et al.*, Pulmonary Vascular Endothelialitis, Thrombosis, and Angiogenesis in Covid-19. *N Engl J Med* **383**, 120-128 (2020).

152. P. M. Scherer, D. L. Chen, Imaging Pulmonary Inflammation. *J Nucl Med* **57**, 1764-1770 (2016).

153. S. J. English *et al.*, CCR2 Positron Emission Tomography for the Assessment of Abdominal Aortic Aneurysm Inflammation and Rupture Prediction. *Circ Cardiovasc Imaging* **13**, e009889 (2020).

154. J. Schyns *et al.*, Non-classical tissue monocytes and two functionally distinct populations of interstitial macrophages populate the mouse lung. *Nat Commun* **10**, 3964 (2019).

155. C. C. Bain, A. S. MacDonald, The impact of the lung environment on macrophage development, activation and function: diversity in the face of adversity. *Mucosal Immunol* **15**, 223-234 (2022).

156. R. R. Lobb, M. E. Hemler, The pathophysiologic role of alpha 4 integrins in vivo. *The Journal of clinical investigation* **94**, 1722-1728 (1994).

157. M. Duan *et al.*, CD11b immunophenotyping identifies inflammatory profiles in the mouse and human lungs. *Mucosal Immunol* **9**, 550-563 (2016).

158. N. Wu *et al.*, Promising bifunctional chelators for copper 64-PET imaging: practical (64)Cu radiolabeling and high in vitro and in vivo complex stability. *J Biol Inorg Chem* **21**, 177-184 (2016).

159. T. J. Wadas, E. H. Wong, G. R. Weisman, C. J. Anderson, Copper chelation chemistry and its role in copper radiopharmaceuticals. *Curr Pharm Des* **13**, 3-16 (2007).

160. R. Farkas *et al.*, (64)Cu- and (68)Ga-Based PET Imaging of Folate Receptor-Positive Tumors: Development and Evaluation of an Albumin-Binding NODAGA-Folate. *Mol Pharm* **13**, 1979-1987 (2016).

161. D. Brasse, A. Nonat, Radiometals: towards a new success story in nuclear imaging? *Dalton Trans* **44**, 4845-4858 (2015).

162. A. V. Misharin *et al.*, Monocyte-derived alveolar macrophages drive lung fibrosis and persist in the lung over the life span. *J Exp Med* **214**, 2387-2404 (2017).

163. A. C. McQuattie-Pimentel, G. R. S. Budinger, M. N. Ballinger, Monocyte-derived Alveolar Macrophages: The Dark Side of Lung Repair? *Am J Respir Cell Mol Biol* **58**, 5-6 (2018).

164. G. Matute-Bello, C. W. Frevert, T. R. Martin, Animal models of acute lung injury. *Am J Physiol Lung Cell Mol Physiol* **295**, L379-399 (2008).

165. M. Tabary, J. S. Lee, Alveolar Macrophage Heterogeneity Goes up in Smoke? *Am J Respir Cell Mol Biol* **67**, 150-152 (2022).

166. K. J. Mould *et al.*, Airspace Macrophages and Monocytes Exist in Transcriptionally Distinct Subsets in Healthy Adults. *Am J Respir Crit Care Med* **203**, 946-956 (2021).

167. M. Liegeois *et al.*, Airway Macrophages Encompass Transcriptionally and Functionally Distinct Subsets Altered by Smoking. *Am J Respir Cell Mol Biol* **67**, 241-252 (2022).

168. S. Watanabe, M. Alexander, A. V. Misharin, G. R. S. Budinger, The role of macrophages in the resolution of inflammation. *The Journal of clinical investigation* **129**, 2619-2628 (2019).

169. L. Salvati, B. Palterer, P. Parronchi, Spectrum of Fibrotic Lung Diseases. *N Engl J Med* **383**, 2485 (2020).

170. L. Plantier *et al.*, Physiology of the lung in idiopathic pulmonary fibrosis. *Eur Respir Rev* **27** (2018).

171. V. Cottin, R. Teague, L. Nicholson, S. Langham, M. Baldwin, The Burden of Progressive-Fibrosing Interstitial Lung Diseases. *Front Med (Lausanne)* **9**, 799912 (2022).

172. R. Brownell *et al.*, Precision Medicine: The New Frontier in Idiopathic Pulmonary Fibrosis. *Am J Respir Crit Care Med* **193**, 1213-1218 (2016).

173. E. S. White, M. Thomas, S. Stowasser, K. Tetzlaff, Challenges for Clinical Drug Development in Pulmonary Fibrosis. *Front Pharmacol* **13**, 823085 (2022).

174. L. Richeldi *et al.*, Efficacy and safety of nintedanib in idiopathic pulmonary fibrosis. *N Engl J Med* **370**, 2071-2082 (2014).

175. G. Raghu *et al.*, Idiopathic Pulmonary Fibrosis (an Update) and Progressive Pulmonary Fibrosis in Adults: An Official ATS/ERS/JRS/ALAT Clinical Practice Guideline. *Am J Respir Crit Care Med* **205**, e18-e47 (2022).

176. O. Distler *et al.*, Nintedanib for Systemic Sclerosis-Associated Interstitial Lung Disease. *N Engl J Med* **380**, 2518-2528 (2019).

177. T. A. Wynn, Integrating mechanisms of pulmonary fibrosis. *J Exp Med* **208**, 1339-1350 (2011).

178. A. L. McCubbrey *et al.*, Deletion of c-FLIP from CD11b(hi) Macrophages Prevents Development of Bleomycin-induced Lung Fibrosis. *Am J Respir Cell Mol Biol* **58**, 66-78 (2018).

179. T. A. Wynn, T. R. Ramalingam, Mechanisms of fibrosis: therapeutic translation for fibrotic disease. *Nat Med* **18**, 1028-1040 (2012).

180. P. C. Carre *et al.*, Increased expression of the interleukin-8 gene by alveolar macrophages in idiopathic pulmonary fibrosis. A potential mechanism for the recruitment and activation of neutrophils in lung fibrosis. *The Journal of clinical investigation* **88**, 1802-1810 (1991).

181. Y. J. Ryu *et al.*, Bronchoalveolar lavage in fibrotic idiopathic interstitial pneumonias. *Respir Med* **101**, 655-660 (2007).

182. B. W. Kinder *et al.*, Baseline BAL neutrophilia predicts early mortality in idiopathic pulmonary fibrosis. *Chest* **133**, 226-232 (2008).

183. L. Welker, R. A. Jorres, U. Costabel, H. Magnussen, Predictive value of BAL cell differentials in the diagnosis of interstitial lung diseases. *Eur Respir J* **24**, 1000-1006 (2004).

184. J. C. Schupp *et al.*, Macrophage activation in acute exacerbation of idiopathic pulmonary fibrosis. *PLoS One* **10**, e0116775 (2015).

185. J. Lee *et al.*, Bronchoalveolar lavage (BAL) cells in idiopathic pulmonary fibrosis express a complex pro-inflammatory, pro-repair, angiogenic activation pattern, likely associated with macrophage iron accumulation. *PLoS One* **13**, e0194803 (2018).

186. M. P. Keane *et al.*, ENA-78 is an important angiogenic factor in idiopathic pulmonary fibrosis. *Am J Respir Crit Care Med* **164**, 2239-2242 (2001).

187. M. W. Ziegenhagen *et al.*, Increased expression of proinflammatory chemokines in bronchoalveolar lavage cells of patients with progressing idiopathic pulmonary fibrosis and sarcoidosis. *J Investig Med* **46**, 223-231 (1998).

188. L. Zhang *et al.*, Macrophages: friend or foe in idiopathic pulmonary fibrosis? *Respir Res* **19**, 170 (2018).

189. E. Y. Bissonnette, J. F. Lauzon-Joset, J. S. Debley, S. F. Ziegler, Cross-Talk Between Alveolar Macrophages and Lung Epithelial Cells is Essential to Maintain Lung Homeostasis. *Front Immunol* **11**, 583042 (2020).

190. D. Aran *et al.*, Reference-based analysis of lung single-cell sequencing reveals a transitional profibrotic macrophage. *Nat Immunol* **20**, 163-172 (2019).

191. N. Joshi *et al.*, A spatially restricted fibrotic niche in pulmonary fibrosis is sustained by M-CSF/M-CSFR signalling in monocyte-derived alveolar macrophages. *Eur Respir J* **55** (2020).

192. S. J. Allden *et al.*, The Transferrin Receptor CD71 Delineates Functionally Distinct Airway Macrophage Subsets during Idiopathic Pulmonary Fibrosis. *Am J Respir Crit Care Med* **200**, 209-219 (2019).

193. M. A. Gibbons *et al.*, Ly6Chi monocytes direct alternatively activated profibrotic macrophage regulation of lung fibrosis. *Am J Respir Crit Care Med* **184**, 569-581 (2011).

194. F. Li *et al.*, Monocyte-derived alveolar macrophages autonomously determine severe outcome of respiratory viral infection. *Sci Immunol* **7**, eabj5761 (2022).

195. Y. Liu *et al.*, Noninvasive Imaging of CCR2(+) Cells in Ischemia-Reperfusion Injury After Lung Transplantation. *Am J Transplant* **16**, 3016-3023 (2016).

196. A. Prasse *et al.*, BAL Cell Gene Expression Is Indicative of Outcome and Airway Basal Cell Involvement in Idiopathic Pulmonary Fibrosis. *Am J Respir Crit Care Med* **199**, 622-630 (2019).

197. B. Ley *et al.*, A multidimensional index and staging system for idiopathic pulmonary fibrosis. *Ann Intern Med* **156**, 684-691 (2012).

198. G. Raghu, Idiopathic pulmonary fibrosis: lessons from clinical trials over the past 25 years. *Eur Respir J* **50** (2017).

199. T. M. Maher, Precision medicine in idiopathic pulmonary fibrosis. *QJM* **109**, 585-587 (2016).

200. D. J. DePianto *et al.*, Heterogeneous gene expression signatures correspond to distinct lung pathologies and biomarkers of disease severity in idiopathic pulmonary fibrosis. *Thorax* **70**, 48-56 (2015).

201. J. D. Herazo-Maya *et al.*, Validation of a 52-gene risk profile for outcome prediction in patients with idiopathic pulmonary fibrosis: an international, multicentre, cohort study. *Lancet Respir Med* **5**, 857-868 (2017).

202. L. J. De Sadeleer *et al.*, BAL Transcriptomes Characterize Idiopathic Pulmonary Fibrosis Endotypes With Prognostic Impact. *Chest* **161**, 1576-1588 (2022).

203. L. M. Kraven *et al.*, Cluster analysis of transcriptomic datasets to identify endotypes of idiopathic pulmonary fibrosis. *Thorax* 10.1136/thoraxjnl-2021-218563 (2022).

204. D. S. Wilkes *et al.*, Oral immunotherapy with type V collagen in idiopathic pulmonary fibrosis. *Eur Respir J* **45**, 1393-1402 (2015).

205. A. T. Goodwin, G. Jenkins, Molecular Endotyping of Pulmonary Fibrosis. *Chest* **149**, 228-237 (2016).

206. T. Derlin *et al.*, Clinical Molecular Imaging of Pulmonary CXCR4 Expression to Predict Outcome of Pirfenidone Treatment in Idiopathic Pulmonary Fibrosis. *Chest* **159**, 1094-1106 (2021).

207. V. Ambrosini *et al.*, 68Ga-DOTANOC PET/CT allows somatostatin receptor imaging in idiopathic pulmonary fibrosis: preliminary results. *J Nucl Med* **51**, 1950-1955 (2010).

208. T. M. Maher *et al.*, A positron emission tomography imaging study to confirm target engagement in the lungs of patients with idiopathic pulmonary fibrosis following a single dose of a novel inhaled alphavbeta6 integrin inhibitor. *Respir Res* **21**, 75 (2020).

209. L. Landsman, S. Jung, Lung macrophages serve as obligatory intermediate between blood monocytes and alveolar macrophages. *J Immunol* **179**, 3488-3494 (2007).

210. A. L. Kesner *et al.*, Gating, enhanced gating, and beyond: information utilization strategies for motion management, applied to preclinical PET. *EJNMMI Res* **3**, 29 (2013).

211. Z. T. Rosenkrans *et al.*, [(68) Ga]Ga-FAPI-46 PET for non-invasive detection of pulmonary fibrosis disease activity. *Eur J Nucl Med Mol Imaging* **49**, 3705-3716 (2022).

212. H. R. Collard *et al.*, Acute Exacerbation of Idiopathic Pulmonary Fibrosis. An International Working Group Report. *Am J Respir Crit Care Med* **194**, 265-275 (2016).

213. P. M. George, C. M. Patterson, A. K. Reed, M. Thillai, Lung transplantation for idiopathic pulmonary fibrosis. *Lancet Respir Med* **7**, 271-282 (2019).

214. M. Neighbors *et al.*, Prognostic and predictive biomarkers for patients with idiopathic pulmonary fibrosis treated with pirfenidone: post-hoc assessment of the CAPACITY and ASCEND trials. *Lancet Respir Med* **6**, 615-626 (2018).

215. B. B. Moore, C. M. Hogaboam, Murine models of pulmonary fibrosis. *Am J Physiol Lung Cell Mol Physiol* **294**, L152-160 (2008).

216. A. Moeller, K. Ask, D. Warburton, J. Gauldie, M. Kolb, The bleomycin animal model: a useful tool to investigate treatment options for idiopathic pulmonary fibrosis? *Int J Biochem Cell Biol* **40**, 362-382 (2008).

217. T. Liu, F. G. De Los Santos, S. H. Phan, The Bleomycin Model of Pulmonary Fibrosis. *Methods Mol Biol* **1627**, 27-42 (2017).

218. P. Italiani, D. Boraschi, Development and Functional Differentiation of Tissue-Resident Versus Monocyte-Derived Macrophages in Inflammatory Reactions. *Results Probl Cell Differ* **62**, 23-43 (2017).

219. Anonymous (2022) Investigational New Drug (IND) Application.

220. S. Sanges *et al.*, Biomarkers of haemodynamic severity of systemic sclerosis-associated pulmonary arterial hypertension by serum proteome analysis. *Ann Rheum Dis* **82**, 365-373 (2023).

221. P. Kiczmer *et al.*, Assessment of CMKLR1 level in colorectal cancer and its correlation with angiogenic markers. *Exp Mol Pathol* **113**, 104377 (2020).

222. M. Westhrin *et al.*, Chemerin is elevated in multiple myeloma patients and is expressed by stromal cells and pre-adipocytes. *Biomark Res* **6**, 21 (2018).

223. K. L. Graham *et al.*, A novel CMKLR1 small molecule antagonist suppresses CNS autoimmune inflammatory disease. *PLoS One* **9**, e112925 (2014).

224. T. Imaizumi *et al.*, The discovery and optimization of a series of 2-aminobenzoxazole derivatives as ChemR23 inhibitors. *Bioorg Med Chem* **27**, 115091 (2019).

225. T. Imaizumi *et al.*, The design, synthesis and evaluation of 2-aminobenzoxazole analogues as potent and orally efficacious ChemR23 inhibitors. *Bioorg Med Chem* **28**, 115622 (2020).

226. T. Imaizumi *et al.*, Discovery and mechanistic study of thiazole-4-acylsulfonamide derivatives as potent and orally active ChemR23 inhibitors with a long-acting effect in cynomolgus monkeys. *Bioorg Med Chem* **56**, 116587 (2022).

227. G. Barnea *et al.*, The genetic design of signaling cascades to record receptor activation. *Proc Natl Acad Sci U S A* **105**, 64-69 (2008).

228. W. Beaino, C. J. Anderson, PET imaging of very late antigen-4 in melanoma: comparison of 68Ga- and 64Cu-labeled NODAGA and CB-TE1A1P-LLP2A conjugates. *J Nucl Med* **55**, 1856-1863 (2014).

229. J. Toms *et al.*, Targeting Fibroblast Activation Protein: Radiosynthesis and Preclinical Evaluation of an (18)F-Labeled FAP Inhibitor. *J Nucl Med* **61**, 1806-1813 (2020).